MATERIALS SCIENCE AND TECHNOLOGIES

NUMERICAL SIMULATION OF THE HEAT CONDUCTIVITY OF RANDOMLY INHOMOGENEOUS TWO-DIMENSIONAL COMPOSITE MATERIALS

MATERIALS SCIENCE AND TECHNOLOGIES

Additional books in this series can be found on Nova's website under the Series tab.

Additional e-books in this series can be found on Nova's website under the eBooks tab.

MATERIALS SCIENCE AND TECHNOLOGIES

NUMERICAL SIMULATION OF THE HEAT CONDUCTIVITY OF RANDOMLY INHOMOGENEOUS TWO-DIMENSIONAL COMPOSITE MATERIALS

ALEXANDER PYSARENKO, PHD

AND

IGOR ZAGINAYLO, PHD

nova
science publishers
New York

NOTICE TO THE READER

Library of Congress Cataloging-in-Publication Data

ISBN: 978-1-53614-687-5

Published by Nova Science Publishers, Inc. † New York

CONTENTS

PREFACE

The development of new composite materials is one of the important tasks of materials science. The growth in the number of applications of composite materials is the reason for an intensive study of their physical properties. Composites are used in numerous industrial processes that involve heating or cooling. This raises the need for the manufactoring of composite materials with high and low thermal conductivity, respectively.

Theoretical homogenization methods allow one to predict the thermal conductivity of composites. However, the effect of the placement parameters of inclusions on the thermal properties of the composite requires additional consideration. The random nature of the placement of inclusions in the matrix is the reason for using statistical methods of investigation. This book deals with the study of effective thermal conductivity and local heat fluxes in composites using numerical methods.

The plan of the book is as follows. Introduction and second sections present the wide variety of theoretical and empirical models for heat transport in two-component composites and their governing scientific principles. The third section is devoted to the numerical methods in heat conduction processes in composites. It covers finite difference method, finite element method, Monte Carlo and multi-scale methods. In this section we give justifications for the choice of the finite difference method

and the Monte Carlo method for numerical experiments on the study of heat transfer in two-component composites.

The fourth section describes the computational model for two-component composite material with differ values of matrix and filler thermal conductivity. The model geometry which includes rectangular matrix, inclusions and grid cells has been chosen to define the density and direction of the local heat fluxes through the local grid cell. The study assumes a random placement of inclusions in the composite matrix with the following parameters: the concentration and size of inclusions, the minimum distance between the inclusions.

The fifth section deals with the distribution statistics of the effective heat conductivity. General forms of the effective thermal conductivity distributions and their transformation have been obtained when the parameters of the placement of heat-insulating inclusions have been changed. Moreover, the influence of the placement heat-insulating inclusions on the parameters of the effective thermal conductivity distributions has also been discussed. The effective thermal conductivity dependence on the direction of temperature gradient leads to a fruitful concept of the effective anisotropy of thermal conductivity. The Monte Carlo simulation has been used to obtain the statistics of the effective anisotropy of the thermal conductivity distributions and its relationship to the effective thermal conductivity distributions statistics.

The local heat fluxes statistics and pattern maps of local heat fluxes through a randomly inhomogeneous two-phase medium with a heat-conducting matrix and heat-insulating inclusions have been analyzed in the sixth section. Numerical experiments reveal the influence of the number and extent of induced heat-conducting channels on the effective thermal conductivity of the material. The heat fluxes maps analyse allows considering the groups of heat-insulating inclusions in the form of thermal lenses that focus local heat fluxes into induced heat-conducting channels. Special attention has been paid to an area with a shortage of induced heat-conducting channels, so-called dark matrix. Multimodal distributions of the local heat fluxes density, as well as the binding of two distribution modes to heat-insulating inclusions and induced thermal conductive channels have

been described. The third mode of distribution was tied to a dark matrix on the heat-insulating inclusions map. Numerical results allow to describe the analytical dependences of the log-normal modes parameters of the local heat fluxes density distribution on the parameters of the heat-insulating inclusions placement. Section also presents the statistical distributions of angles between the direction of local heat fluxes and the temperature macro gradient as well as the transformation of the character of distribution when changing the parameters of placement of inclusions.

Finally, we would like to thank our wives, Tatyana and Oksana, for their unwavering support, patience, and understamding. Without their support, this book would never have been finished.

Alexander Pysarenko,
Igor Zaginaylo

August,2018

LIST OF ABBREVIATIONS

FDM	Finite difference method
FEM	Finite element method
GCT	Generalized conductivity theory
LHF	Local heat flux
RVE	Representative Volume Element

LIST OF SYMBOLS

Notation that is largely confined to sections is mostly excluded from the list below.

a	Inclusion radius
a_1, a_2	Coefficients, $W \cdot m^{-1} \cdot K^{-1}$
b	Inclusion size
c	Concentration of inclusions
d	Minimum distance
h	Grid step
i	Computational grid cell number along y-coordinate
J	Local heat flux
j	Computational grid cell number along x-coordinate
F_1, F_2	Functions
f_1, f_2	Probability density distribution functions
N	Number of inclusions
Pw	Mode power
p	Probability
s′	Spatial component
s_κ	Standard deviation of $<\kappa_e>$ distributions
s_δ	Standard deviation of $\delta\kappa_e$ distribution
T	Absolute temperature, K

w_Ω	Volumetric heat source

Subscripts

f	Filler
L	Left
R	Right
m	Matrix
i	Index
z	Index
W	Weibull parameter

Greek Symbols

α_3	Skewness
α_4	Kurtosis
β	Angle, specific direction
γ	Variable
κ	Relative thermal conductivity
λ	Thermal conductivity, $W \cdot m^{-1} \cdot K^{-1}$
ν	Number of tests
ξ	Half-width the range of values
ρ	Probability density
σ_b	Root-mean-square deviation
σ'	Standard deviation
ϑ	Coefficient of variation
Ω	Region of composite
φ_c	Angle component

Greek Subscripts

α	Angle
β	Angle, specific direction
Ω	Region of composite

Chapter 1

INTRODUCTION

The development of new high quality and cost-efficient materials is of great interest for the enhancing the modern industry. These materials have to comply with the requirements for the performance characteristics of finished products.

The variety of properties of composite materials achieved by varying the types of components, their volume fractions, shape, and the nature of the distribution of the filler particles in the matrix material makes them quite competitive in comparison with traditional materials. Therefore, the development of new composite materials is one of the important tasks of materials science. It should be noted that the technical and economic efficiency of the use of new materials largely depends on the ability to predict their performance properties.

The thermal conductivity of a composite material is of great importance in a wide range of applications. Thermal insulation plays an important role in contributing to the energy savings in the building by heat gains and losses through the building envelope. At the same time, noise pollution is increasingly getting more attention amongst the construction industry as it is a major health concern. Special composite materials are applied as noise and heat insulators in the enclosing structures of buildings and structures [1–8].

However, a lot of effort is put in order to improve composite material properties and especially thermal conductivity. Microelectronic devices with high thermal conductivity are desirable in order for heat to be efficiently dissipated. In this way, the operating temperature can be kept low, avoiding dielectric failures due to overheating. In many publications, improvement in the thermal conductivity of polymers when fillers are included has been reported [9–16]. The development of composites with low electrical conductivity and high thermal conductivity significantly affects the miniaturization, reliability and lifetime of electronic devices. Composite materials are used in the construction of heat shields and heat exchangers (evaporators, condensers, heat pump systems, gas coolers, tube banks and so on) [17–32]. The major properties in this case are mechanical/structural stability and resistant to aggressive influences, including chemical and radiation. Thus, the physical properties of the various composites must be carefully studied to predict their behavior and thereby optimize their use in real applications.

Composites, in the form of a matrix with polyhedral solid inclusions, are widely used as technical constructional, construction and functional materials in various devices. The study of the thermal behavior of such composites, which include two or more components with different thermal properties, has been conducted for more than 100 years. In order to predict their thermal behavior, a concept of effective thermal conductivity was developed. This concept significantly simplifies the work of the designer in many technical applications and technological developments.

Numerous theoretical and empirical models have been proposed to predict effective thermal conductivity. However, despite the importance of this property and the significant amount of studies that has been carried out, the determination of the effective thermal conductivity of the composite is only partially understood. The reason is that the effective thermal conductivity is a complex function of the thermal conductivity of the various components of the composite material, their geometry, the distribution of fillers within the matrix material, and the contact between the components.

Analytical methods for solving heat conduction problems can be applied to a finite number of problems in which the geometry of the object is represented only by the simplest forms (circle, rectangle, etc.). An additional factor that complicates the theoretical description of heat transfer in composites is the random spatial distribution of the filler particles.

The spatially-graded composites have a wide range of applications. Such composites consist of two or more components in which the relative volume fractions of the components or the dimensions of the filler particles vary in space according to a fixed law [33–38]. The space-graded composites due to their thermal anisotropy can form effective thermal barriers and heat flow routers.

The calculation of the thermal conductive properties of materials with randomly inhomogeneous spatial distribution of filler particles, with complex shape, as well as the thermal conductive properties of spatially-graded materials, is possible using numerical methods. The calculation of the temperature profiles in such materials requires the use of the concept of effective thermal conductivity and the study of the distribution of local heat fluxes in inhomogeneous systems with complex geometry.

Our work is devoted to numerical modeling of heat transfer processes in two-component materials with randomly inhomogeneous spatial distribution of filler particles. Such a choice of the research object allows us to use a statistical approach to the modeling and analysis of material properties. In addition, the results of the study will highlight those physical laws that play an important role in the formation of thermal properties of spatially-graded composites.

Chapter 2

MODELS FOR THERMAL CONDUCTIVITY OF COMPOSITES

2.1. HOMOGENIZATION METHODS

Numerous models have been proposed to predict macroscopic properties of the heterogenic medium, knowing the properties and volume fractions of the constituents. These are known effective medium theories. In these models, heterogenic materials are considered as being macroscopically homogenized. Due to their nature, effective medium approximations are unable to accurately predict the properties of heterogenic material.

Early Maxwell and Rayleigh works [39, 40] based on mathematically analogy of electrical and heat conductivity presented analytical expressions for effective conductivity of heterogenic medium. These authors considered the problem of spherical particles (filler) of conductivity λ_f embedded in a continuous matrix of conductivity λ_m. Rayleigh's model assumes the thermal interaction between the embedded spheres. The Maxwell and Rayleigh expressions for effective thermal conductivity λ_e of heterogenic medium have the same form

$$\frac{\lambda_e}{\lambda_m} = 1 + 3\alpha_i\varphi \quad i = M, R, \tag{1}$$

where φ is the volume fraction of the filler;

$$\alpha_M^{-1} = \left(\frac{\lambda_f + 2\lambda_m}{\lambda_f - \lambda_m}\right) - \varphi \tag{2}$$

and

$$\alpha_R^{-1} = \left(\frac{\lambda_f - 2\lambda_m}{\lambda_f - \lambda_m}\right) - \varphi + 1.569\left(\frac{\lambda_f - \lambda_m}{3\lambda_f - 4\lambda_m}\right)\varphi^{10/3} + \ldots, \tag{3}$$

Are the Maxwell and Rayleigh model coefficients. Both formulae are applicable only in the case of low φ ($\varphi \leq 25\%$).

Hamilton and Crosser [41] modified Maxwell's model. They studied the influence of included particle shape, composition, and pure component conductivity upon the thermal conductivity of heterogeneous two-component media consisting of a continuous and a discontinuous phase. The definition for the mixture thermal conductivity given by authors is:

$$\frac{\lambda_e}{\lambda_m} = \frac{\lambda_f + (\alpha_{HC} - 1)\lambda_m - (\alpha_{HC} - 1)\varphi(\lambda_m - \lambda_f)}{\lambda_f + (\alpha_{HC} - 1)\lambda_m + \varphi(\lambda_m - \lambda_f)}, \tag{4}$$

where ψ is sphericity; $\alpha_{HC} = 3/\psi$.

The authors proposed that the effect of particle shape should not be important when the ratio of conductivities of the two phases is below about 100. The results of study pointed on a strong shape effect in the case then discontinuous phase has the higher conductivity: $\lambda_f >> \lambda_m$. The authors pointed out that additional compound can be formed at the interfaces between the two phases as well as the shape of the particles may be indeterminate in the case of in the case of zero distance between the

particles. All these complications will have a large effect on the mixture conductivity in cases where the phases have widely different conductivity.

Experimental results and theoretical analyze indicated that the effective thermal conductivity of composites can be affected by a thermal barrier resistance at the interface between the individual components [42–50].

Hasselman and Johnson [51] examined the influence of particle size and interfacial gaps between filler and matrix on the composite materials effective thermal conductivity. They proposed modification of Maxwell and Rayleigh expressions for effective thermal conductivity of composites with nonzero interfacial thermal resistance. Hasselman-Johnson formulae based on the dependence of the effective thermal conductivity on the particle radius a_f and the boundary conductance h_c. The authors examined the thermal conduction in continuous matrix phase with inclusions of spherical, cylindrical and flat plate geometry. The formulae for effective thermal conductivity are

$$\frac{\lambda_e}{\lambda_m} = \frac{\alpha_{HJ1}\varphi + \alpha_{HJ2}}{\alpha_{HJ2} - 0.5\alpha_{HJ1}\varphi} \quad \text{(Spherical geometry)} \tag{5}$$

$$\frac{\lambda_e}{\lambda_m} = \frac{\alpha_{HJ1}\varphi + \alpha_{HJ2}}{-\alpha_{HJ1}(\varphi + 1)} \quad \text{(Cylindrical geometry)} \tag{6}$$

$$\frac{\lambda_e}{\lambda_f} = \frac{1}{\dfrac{\lambda_f}{\lambda_m} + \dfrac{\lambda_f \varphi}{a_f h_c} - \alpha_{HJ1}\varphi} \quad \text{(Flat plate geometry),} \tag{7}$$

where

$$\alpha_{HJ1} = \frac{\lambda_f}{\lambda_m} - \frac{\lambda_f}{a_f h_c} - 1, \tag{8}$$

and

$$\alpha_{HJ2} = 1 + \frac{\lambda_f}{2\lambda_m} + \frac{\lambda_f}{a_f h_c}. \quad (9)$$

Inclusions with flat plate geometry (last expression) are oriented perpendicular to the heat flux.

The derivation of the effective thermal conductivity of the composite relied on assessing the cumulative effect of small spheres of radius a_f within a large sphere with the effective thermal conductivity λ_e. Analogous arguments were used to calculate the effective thermal conductivity for the case of the cylindrical geometry of inclusions. Hasselman and Johnson examined thermal conductivity of composite with flat plate inclusions oriented perpendicular to heat flow. The effective thermal resistivity of composite was obtained by the addition of the thermal resistivity of each component plus the sum of all the interfacial thermal resistances.

The above results indicate that the effect of the interfacial thermal barrier resistance on the effective thermal conductivity is controlled by the non-dimensional parameter $\lambda_f /(a_f h_c)$, and its value relative to the ratio $\lambda_f /(\lambda_m)$. For $\lambda_f /(a_f h_c) \to \infty$ the effective thermal conductivity corresponds to the value for a matrix with a dispersed pore phase, irrespective of the absolute value of λ_f. The results of the study indicate that the effective thermal conductivity for any value of h_c, not equal to infinity, depends on the size (and size distribution) of the dispersed phase particles.

Tavangar et al. [52] considered the factors that limit Maxwell mean-field scheme usage, including the popular Hasselmann-Johnson model, for estimating the effective thermal conductivity of composite, especially in the case of a high effective phase contrast between composite constituents. Predictive schemes [53–56] for thermal conductivity of composites are assessed in the range of intermediate effective phase contrast against experimental values on diamond particle-reinforced Ag-Si alloy composites. The two composites were reinforced with synthetic diamond particles of different size in order to vary the effective thermal conductivity

of the inclusion phase due to the presence of a finite interface thermal conductance. Tavangar and his co-authors used the following formulas for particulate composites to confront experimental data with the Maxwell mean-field approach and differential effective medium, respectively

$$A = \frac{\varphi^e(1+2\varphi)+2(1-\varphi)}{\varphi^e(1-\varphi)+(2+\varphi)}, \text{ and} (1-\varphi) = \frac{\varphi^e - A}{\varphi^e - 1} A^{-1/3}, \tag{10}$$

where $A = \lambda_c/\lambda_m$ is conductivity amplification factor, λ_c is thermal conductivity of the composite,

$$\varphi^e = \lambda_f / \left[1 + \lambda_f / (a_f h_c)\right] . \tag{11}$$

An intrinsic thermal conductivity of the two diamond sizes was deduced in study. While the interface thermal conductance h_c remains roughly constant for the data sets deduced from differential effective medium scheme, the interface thermal conductance diverges from the data analyzed by the Maxwell mean-field scheme, requiring even negative values at very high effective phase contrast. For low effective phase contrast (small diamond particles and low matrix heat treatment temperature) the interface thermal conductance deduced based on the Maxwell mean-field scheme is similar to that found by the differential effective medium scheme for all conditions.

Their study shows that the results obtained with differential effective medium scheme were close to experimental in the whole examined range of effective phase contrast

$$\gamma_c = \lambda^e / \lambda_m (\gamma_c \subset [2;8]), \tag{12}$$

whereas the Hasselmann-Johnson model failed above $\gamma_c = 4$.

Bruggeman [57] and Landauer [58] proposed mathematical formalism which allows one to estimate effective properties of heterogeneous

materials, such as thermal conductivity, and thermal diffusivity. This theory is called the differential affective medium theory and assumes that a composite material may be constructed gradually by introducing infinitesimal changes to an already existing material. The scheme presented by Bruggeman and Landauer gives formulae for multi-component systems, in addition to the classical case of two components. One of the advantages is the high accuracy results for high filler volume fractions. Using Bruggeman's approach, Every and Tzou [59] obtained an expression for effective thermal conductivity of particulate composites

$$1-\varphi=\left(\frac{\lambda_m}{\lambda_e}\right)^{\lambda_f(1+2\alpha')/3\alpha_{ET}}\left(\frac{\lambda_e-\alpha_{ET}}{\lambda_m-\alpha_{ET}}\right)^{\lambda_f/\alpha_{ET}}, \tag{13}$$

where

$$\alpha'=\frac{R_{br}\lambda_m}{a_f} \tag{14}$$

is a dimensionless parameter depending on interfacial thermal resistance between filler and matrix, R_{br} is specific boundary resistance, and

$$\alpha_{ET}=\lambda_f(1-\alpha'). \tag{15}$$

Assuming in particular case that filler conductivity is much greater than that of the matrix, Every and Tzou approach may be simplified to formula [60]:

$$\frac{\lambda_m}{\lambda_f}=(1-\varphi)^{3\alpha_{ET}/[\lambda_f(1+2\alpha')]}. \tag{16}$$

The radius a_f boundary value for ZnS/diamond composite was estimated in study. The case of smaller particle sizes leads to mismatch

between the experimental results and theoretical predictions. This inconsistency may be caused by the non-spherical shape of diamond particles while the theoretical formula is for spheres. Authors observed that the thermal conductivity of ZnS/D composite is increased by adding large particles of highly conducting diamond, but lowered by the addition of sub-micron size particles of diamond. This effect is explained in terms of the interfacial thermal resistance which becomes increasingly dominant as the particles becomes smaller (because that increases their surface to volume ratio). A phenomenological model in which the interface resistance is expressed as an effective Kapitza radius is presented. Every, and Tzou applied Maxwell and Bruggeman models for low and high volume fraction composites, correspondingly. Both results, Maxwell and Bruggeman, predict that the effective thermal conductivity of the composite will be unchanged by the particles if the radius of the dispersed particles is the same as the Kapitza radius. The effective conductivity of the composite is lowered by the particles with radius smaller than the Kapitza radius, even if the particles themselves have a higher conductivity than that of the matrix. The conducting limit reached when the particles are about 10 times the Kapitza radius.

Thus the Kapitza radius becomes a physically important parameter in the design of composites where the objective is to change the thermal conductivity by mixing two different constituents.

Lewis and Nielsen semi-theoretical model provides reliable evaluation of thermal conductivity for a wide range of particle shapes and patterns. The Nielsen model formulation [61] for evaluating thermal conductivity is defined as

$$\frac{\lambda_e}{\lambda_m} = \frac{1-\alpha_{LN1}\alpha_{LN2}\varphi}{1-\alpha_{LN2}\psi\varphi}, \tag{17}$$

where

$$\alpha_{LN1} = k_E - 1 \tag{18}$$

$$\alpha_{LN2} = \frac{\lambda_f / \lambda_m - 1}{\lambda_f / \lambda_m + \alpha_{LN1}}; \tag{19}$$

$$\psi = 1 + \left(\frac{1 - \varphi_{\max}}{\varphi_{\max}^2} \right) \varphi . \tag{20}$$

The value $\varphi_{\max}$ is the maximum packing fraction in the aggregates. The constant k_E represents the Einstein coefficient, which takes into account the geometry and orientation of the particles dispersed within the polymer matrix. The factor $\varphi_{\max}$ represents the maximum packing fraction of filler, which is the fraction of the true volume of the filler to the volume of the filler when packed to its maximum capacity. The constant α_{LN1} depends primarily upon the shape of the dispersed particles and how they are oriented with respect to the direction of heat flux. The constant α_{LN1} is related to the generalized Einstein coefficient k_E. The factor α_{LN2} is a constant which takes into account the relative conductivity of the two components. The study results indicate that equation (17) for composite systems is a very good approximation in most cases. Equations (17) predicts values of thermal conductivity which are somewhat too high when $\varphi = \varphi_{\max}$ if the discontinuous dispersed phase is the more conducting of the two phases. However, at lower concentrations, theory and experiment generally agree very well. The effect of particle packing can be taken care of by the value $\varphi_{\max}$, which can be experimentally measured in many cases and calculated in other cases. The Nielsen model is inconsistent with the experimental results for high values volume fraction of the filler.

Using variation principles Donea [62] obtained upper, λ^+, and lower, λ, bound for the effective thermal conductivity of composite material which is statistically homogeneous and contains two phases each having isotropic and uniform thermal conductivity

$$\lambda^+ = \varphi \overline{\lambda} + (1 - \varphi) \lambda_m , \tag{21}$$

$$\lambda^{-} = \frac{\bar{\lambda}\,\lambda_m}{\varphi\lambda_m + (1-\varphi)\bar{\lambda}} \ . \tag{22}$$

For spherical inclusions

$$\bar{\lambda} = \frac{\lambda_m\left[(p'+2)+2s(p'-1)\right]}{(p'+2)-(p'-1)s}, \tag{23}$$

where $a_{\max}$ is the radius of the larges possible spherical shell surrounding the inclusion for random dispersion of spheres,

$$p' = \lambda_f / \lambda_m \text{ and } s = \left(a_f / a_{\max}\right)^3. \tag{24}$$

Equality $\lambda^{+} = \lambda^{-} = \bar{\lambda}$ corresponds to a matrix with a random dispersion of inclusions with varying sizes.

The effective thermal conductivity of materials reinforced by parallel circular fibers has also been investigated in [62]. The fibers were assumed to be of identical cross section and to be located at the vertices of a square or a hexagonal lattice. Exact bounds for the thermal conductivity in the transverse direction were obtained by using a concentric-cylinders model

$$\bar{\lambda} = \frac{\lambda_m\left[(p'+1)+s(p'-1)\right]}{(p'+1)-(p'-1)s}. \tag{25}$$

From the geometry of the hexagonal array $\varphi = \pi / 2\sqrt{3}$, and for a square array $\varphi = \pi/4$. Donea compared the upper and lower bounds for a hexagonal, a square, and a random array of circular fibers. The bounds for specified packing geometry are seen to be very close together except near the maximum theoretical volume fraction.

Benveniste [63] considered the effective thermal conductivity of a particulate composite exhibiting a thermal contact resistance at interphase boundaries. The study is concerned with the effective thermal conductivity

of composites containing spherical inclusions at non-dilute concentrations. The influence of the interfacial thermal resistance on the value of the effective thermal conductivity of composite was considered following methods considered in [64–67]. Two different micromechanical models are presented which take approximately into account the interaction between the particles: the generalized self-consistent scheme, and Mori-Tanaka theory [68]. Both methods, distinctly different in their approach, result in the same closed-form simple expression for the effective thermal conductivity.

Benveniste defined for homogeneous composite average quantities with imperfect interfaces: intensity H and flux j fields. The equality for flux field follows under the assumption of steady conditions and no heat sources.

At the interface S_{12}, the normal component of the heat flux is continuous, that is

$$j_i^{(1)}\left(S_{12}\right)n_i = j_i^{(2)}\left(S_{12}\right)n_i\,,\ i = 1, 2, \tag{26}$$

where n_i denotes the normal to S_{12} and is defined from the inclusion to the matrix. The study based on two fundamental equations necessary for the determination of the effective thermal conductivity λ_{ij}^{*} and thermal resistivity R_{ij}^{*} tensors:

$$\lambda_{ij}^{*} H_j^0 = \lambda_1 H_i^0 + \left(\lambda_2 - \lambda_1\right)\varphi_2\, \overline{H}_i^{(2)} - \lambda_1\, \varphi_2\, J_i^{(12)}, \tag{27}$$

$$R_{ij}^{*} j_j^0 = R_1 j_i^0 + \left(R_2 - R_1\right)\varphi_2\ \bar{j}_i^{(2)} - \varphi_2\ J_i^{(12)}, \tag{28}$$

where λ, φ_r, and R_r (r = 1, 2) denote, respectively, the thermal conductivity, volume fraction, and thermal resistivity of the isotropic and homogeneous constituents; the intensity components

$$H_i = -\frac{\partial T(x_i)}{\partial x_i}; \tag{29}$$

T (x_i) stands for the temperature field; $j_i = \lambda_{ij} H_j$ are heat flux components;

H_i^0 and j_i^0 are constant intensity and heat flux components at the surface S. The total flux is

$$J_i^{(12)} = \frac{1}{V_m} \int_{S_{12}} (\varphi_2 - \varphi_1) n_i dS_{12} . \tag{30}$$

The average intensity $\overline{H}$ contains an integral involving the jump in the temperature field across S_{12}. The thermal contact resistance between the constituents is presented by third-type boundary conditions. The volume fraction of the composite sphere is chosen in [63] such that $a_f^3 / a_o^3 = \alpha_B$, where a_f denotes the radius of the particle core and a_{or} is the outside radius. The normal component of the heat flux in the generalized self-consistent scheme is continuous at $r = a_f$, and $r = a_o$. The temperature field is continuous at $r = a_o$, but at $r = a_f$ third-type boundary condition prevails. Author mentioned, that the solution for the effective conductivity is valid for equal size inclusions of radius a_f and the maximum volume fraction of the particles need, in this case, be lower than $\alpha_B = \pi/6$.

The Mori-Tanaka theory applied in the present paper to the conductivity problem of a particulate composite exhibiting a thermal contact resistance between the constituents. Benveniste used the dilute approximation, so average heat intensity $\overline{H}$, and heat flux $\overline{J}$ would have been approximated by embedding a single inclusion in an all matrix medium. The heat intensity $\overline{H}$ depends on the average perturbed intensity in the matrix due to the presence of all the inclusions, and perturbed part of the same quantity in the inclusions with respect to the matrix. Author pointed out, that a coincidence between the Mori-Tanaka and generalized

self-consistent approaches does not exist for an imbedding with $a_o^3 / a_f^3 \neq \alpha_B$ and is not to be expected a priori for inclusion shapes other than spheres.

Most homogenization models take into account only the volume content of additives in the composite and do not consider possible changes in their mutual arrangement. The estimation of transverse thermal conductivity of continuous fiber reinforced composites containing a random fiber distribution with imperfect interfaces was performed in [69] using finite element analysis. Study results were compared with the classical solution of Hasselman and Johnson to determine limits of applicability. The results show that for the $\lambda_f / \lambda_m > 1$, the effective thermal conductivity solutions converge at a single Biot number $Bi = h_c a_f / \lambda_f$, irrespective of the volume fraction φ. This value of interfacial thermal conductance will be referred to as the homogenizing value. It can be postulated for all $\lambda_f / \lambda_m > 1$, there exist an imperfect interfacial condition which balances out the effects of the higher fiber conductivity and causes the material to behave homogeneously globally and locally.

For $\lambda_f / \lambda_m > 1$, the Hasselman-Johnson model under predicts thermal conductivity for conditions of nearly perfect interfacial bonding (Bi = 10000). For all λ_f / λ_m, the model over predicts the value of thermal conductivity for conditions of nearly insulated interfaces (Bi = 0.001). Significant differences of up to 10 percent exist between the model and finite element data for conditions of perfect interfacial bonding and $\lambda_f / \lambda_m > 1$. These differences vanish as the interfacial thermal conductance approaches the homogenizing value. Decreasing Bi results in increased differences between the model and results as the material begins to simulate a material containing voids. This can be seen since the differences between the model and numerical results converge to a value on the order of 15 percent (for a fixed volume fraction) once Bi is less than homogenized value. The study results show that the description of dilute fiber reinforcement should be based not on the fiber volume fraction φ and fiber distribution alone, but also include the boundary condition at the

reinforcement interface which controls the level of interaction between the constituents.

2.2. REPRESENTATIVE VOLUME ELEMENT

Homogenization methods are used to extract thermal effective properties of heterogeneous materials from the knowledge of the spatial distribution of their components. Numerical techniques and simulations on samples of the composite microstructure can be applied to solve homogenization problems. In this case, the concept of a representative volume element (RVE) is of paramount importance. RVE is usually considered as the volume V of a heterogeneous material that is large enough to be statistically representative of the composite, i.e., to efficiently include in the element all the microstructure heterogeneities that occur in the composite.

An algorithm of effective thermal conductivity evaluation is based on sequential solution of boundary problems of thermal conductivity with different boundary conditions (in the form of the temperature on the boundary) on RVE of composite with subsequent averaging of the resulting vector field of heat flux.

There are a few issues that need to be carefully considered when carrying out the RVE analyze. The correct RVE corresponding to the assumed fiber distribution must be isolated. Secondly, correct boundary conditions need to be applied to the chosen RVE to model different loading situations. Proper consideration must be given to the periodicity and symmetry of the model in arriving at the correct boundary conditions. Under longitudinal and transverse normal loading, a typical RVE can deform in such a way that it remains a right parallelepiped.

Kanit et al. [70] proposed quantitative definition of the RVE, which is based on statistical arguments. The methodology is applied to a specific random microstructure, namely a two-phase three-dimensional Voronoï mosaic. Three-dimensional Voronoï cells are simple representations of grains in a polycrystalline. A volume V of two-phase heterogeneous

material is considered. Hard phase (respectively highly conductive) has volume fraction φ_h and thermal conductivity λ_h. The soft one (respectively less conductive) has volume fraction φ_s and thermal conductivityλ_s. Three types of boundary conditions are used in the study of the effective thermal conductivity:

a) Uniform gradient of temperature at the boundary: $T = Gx$, $\forall x \in \partial V$, where average temperature gradient is

$$< \nabla T >= \frac{1}{V}\int_V \nabla T dV = G\,, \tag{31}$$

b) Uniform heat flux at the boundary: $jn = Jx$, $\forall x \in \partial V$, where average flux is

$$< j >= \frac{1}{V}\int_V j dV = J\,, \tag{32}$$

where n is the modulus of a vector perpendicular to ∂V,

c) periodic boundary conditions:

$$T = Gx + T_{fl}\,, \forall x \in \partial V\,, \tag{33}$$

where the fluctuation temperature T_{fl} is periodic.

Finite element simulations of volumes of different sizes are performed in the case of linear elasticity and thermal conductivity. The multi-phase element technique and technique of free meshing with tetrahedral elements were compared in the case of the Voronoï mosaic. Authors defined an integral range A_3 in the space R^3 which gives information on the domain size of the structure for which the parameters measured in this volume have a good statistical representatively. In the case of 3D Voronoï mosaic model the integral range is

$$A_3 = E\{V^2\} / E\{V\}\,, \tag{34}$$

where $E\{Z\}$ is the mathematical expectation of property Z. The value of the integral range is deduced from the variance of the volume of the random cell: $A_3 = 1.17$.

The thermal conductivity of the considered material, as a function of the size of the domain is estimated. The macroscopic linear properties of composites are available. They include the Wiener bounds that take only the volume fraction of the components into account.

It shows that the dispersion of results decreases when the size of the volume increases. The mean value of effective thermal conductivity given by the periodic boundary conditions does not vary very much, as compared to the other boundary conditions. For small volume elements, the average thermal conductivity obtained by simulations depends on the boundary conditions: uniform gradient of temperature gives results close to the upper Wiener bound $\lambda_{W+} = \varphi_h\lambda_h + \varphi_s\lambda_s$, and uniform heat flux produces results close to the lower Wiener bound

$$\lambda_{W-} = \frac{\lambda_h\lambda_s}{\varphi_h\lambda_s + \varphi_s\lambda_h}\,. \tag{35}$$

The self-consistent scheme, presented by Beran, gives the overall thermal conductivity λ_e as the solution of the equation

$$\frac{\lambda_h - \lambda_e}{\lambda_h + 2\lambda_e}\varphi_h + \frac{\lambda_s - \lambda_e}{\lambda_s + 2\lambda_e}\varphi_s = 0\,. \tag{36}$$

3D Voronoï mosaic model is relevant for poly-crystals but also for two-phase materials in which both phases percolate. The fluctuations of modules on small domains can be attributed to the percolation level of the hard phase for the fixed realization. The results of the study indicate that

the increase in the contrast of properties leads to an increase of the integral range and of the RVE size.

Kamiński [71] propose the homogenization-based finite element method algorithm for computational analysis [72, 73] of transient heat transfer processes in composite materials. For this purpose, the additional 1D, 2D and 3D composites homogenization models are collected and tested numerically in terms of deterministic as well as stochastic sensitivity. Two essentially different FEM formulations are obtained in study. Numerical results obtained by the use of both symbolic computations and the standard FEM program are related to general deterministic and probabilistic sensitivity of homogenized coefficients. The main purpose of numerical tests was to verify the efficiency of transient heat transfer homogenization procedure using the example of a three component layered composite.

The effective heat conductivity for periodic fiber-reinforced composite in 2D problem where the fiber has the round cross-section and the total composite volume is relatively large in comparison to the single inclusion can be approximated using cylinder assemblage model or, using the spherical inclusion model for spherical inclusions, distributed periodically in 3D composite, in the form of

$$\lambda_e^{(iD)} = \lambda_2 \left[1 + \varphi \left(\frac{1-\varphi}{i} + \frac{\lambda_2}{\lambda_1 - \lambda_2} \right)^{-1} \right], \; i = 2,3 \tag{37}$$

where λ_1, λ_2 are thermal conductivities of composite components. The following assumptions are made in [71]: a) there is no mechanical deformation accompanying thermal process, b) material parameters are independent from the temperature field, c) there are no phase changes and latent heat effects.

Computational experiments performed using symbolic mathematics show the variability of effective heat conductivity for 2D and 3D composites as a function of the reinforcement volume ratio, of composite components conductivity coefficients as well as of the probabilistic

moments of material properties versus volume ratio. The results of particular computational tests indicate that the heat transfer history is not sensitive to the interrelation between heat capacities of the constituents. The steady-state temperature function tends to that obtained for the homogenized composite, while $\lambda_2/\lambda_1 \to 1$. The difference of composite thermal behavior within the second component region starts to be significant for increasing values of the ratio λ_2/λ_1.

All the FEM-based results generally confirm the usefulness of the homogenization method presented above to the transient heat transfer analysis of layered composites [74–85]. The authors point out that the presented homogenization method can be efficiently extended on the stochastic finite element computational modeling, where some of material properties are treated as random variables or fields. The results obtained for deterministic and probabilistic computations of effective heat conductivity show almost the same sensitivity of 1D, 2D and 3D composites to geometrical and material parameters. However the values of this coefficient obtained for the same reinforcement ratio are the largest for the 3D composite with spherical inclusion, next for the 2D fiber-reinforced composite, and the smallest for the 1D case.

The size of a RVE can be defined for a given physical property, a given contrast and, above all, a given precision in the estimation of the effective properties and given number of realizations that one is ready to generate. For the same absolute error on the mean value, the periodic boundary conditions require the largest domain size compared to the other boundary conditions [86–96]. The uniform gradient of temperature at the boundary conditions gives a smaller domain size than the uniform heat flux for the same absolute error. For a given precision, the required number of realizations decreases when the volume increases. The periodic boundary conditions require the largest number of realizations, as compared to other boundary conditions. A scale-dependent comparative study of the different criteria which characterize the finite RVE size is performed in [97]. The effective properties, the Hill condition, the mean and the variance of the stress and strain components in the fiber and the typical inter-fiber distance distributions criteria are analyzed with the aim of defining a statistical

representative volume element. This element should reproduce the same statistics relating to stress and strain fields as all material, as well as statistical data related to the distribution of fibers. Trias et al. defined the dimensionless variable $\delta = L_S/R_f$ for fiber-reinforced composites. This variable relates the side length of the statistical representative volume element L_S and the fiber radius R_f. The work established the size of a statistical representative volume element for a typical carbon fiber reinforced polymer. It is concluded that the minimum size is $\delta = 50$.

Concerning the RVE determination in practical cases, two main approaches can be distinguished which are based on: 1) experimental observations [98–106] by combining basic morphological tools with stereological and image analysis techniques in order to describe the geometrical dispersion of the medium; 2) effective properties by means of analytical approaches or numerical analysis [107–116]. Shan et al. [98] developed methodology to arrive at a sufficiently small micro-structural window that can be regarded as a RVE of a non-uniform micro-structure of a ceramic matrix composite containing a range of fiber sizes, and fiber-rich and -poor regions at the length scale of about 100 μm. Authors presented methodology involves quantitative characterization of microstructure, micro-structure modeling, finite element-based simulations on computer simulated micro-structural widows of different sizes containing 60–2000 fibers, and finite element simulations on large-area high resolution digital image of the composite microstructure containing about 2000 fibers.

Forest et al. [107] used Cosserat modeling to study the size effects in the mechanical behavior of poly-crystals and multi-phase materials. Three-dimensional finite element calculations of periodic Cosserat multi-crystalline aggregates of different grain sizes are provided in this study. The mechanics of generalized continua has been shown to be an appropriate tool to account for size effects in poly-crystal and multi-phase materials. Analysis of study results leads to the necessity of formulating an initial boundary value problem of Cosserat plasticity with periodicity conditions for both the micro-structure and the mechanical fields.

Original statistical-numerical RVE determination method has been developed by Pellisou et al. [117]. The aim of this work was the

determination of RVE size of quasi-brittle random metal matrix composite. Authors developed statistical-numerical RVE determination technique that guarantees, for given RVE size and precision, a sufficient number of realizations while offering a good compromise between the RVE size and the total CPU time. This technique is based on the statistical framework previously used in [63] and on stopping criterion to build the initial samples. Criterion construction relies on: 1) the integration of estimation uncertainty (related to variance and mean) in the identification of the crucial integral range; 2) a sampling strategy that is adapted to the accuracy (i.e., relative error). Connection between linear and non-linear RVE sizes is provided by aspect ratio of energy and elastic integral ranges $\sqrt[3]{A_{ir,E} / A_{ir,C}}$, where integral range equals

$$A_{ir} = \frac{1}{C(X_m,0) - C(X_m,0)^2} \oint_{R^{N'}} \left(C(X_m,0) - C(X_m,0)^2 \right) dh_p \,, \tag{38}$$

where N' is the space dimension. The covariance function associated to an ergodic and stationary random medium X_m and denoted C (X_m, h_p) is the two-point probability function, i.e., the probability for two points with the separation h_p to be in the set

$$X_m : C(X_m, h_p) = P(x \in X_m, x + h_p \in X_m). \tag{39}$$

For h_p = 0, the covariance is the volume fraction of X_m: C (X_m, 0) = φ (X_m). It was shown that integral range depends on the studied property. The integral range is large for non-linear property than for elastic one.

Authors studied the effect of the volume fraction on the RVE size and on the fracture energy accuracy. Particular attention was focused on the volume fraction of the inclusions that gives the maximal standard deviation of the fracture energy. The mean value of the fracture energy converges when the domain size increases. For the intermediate and large domain sizes, the relative error range includes the stabilized value of the mean fracture energy.

The methodology has been successfully to the RVE determination of quasi-brittle random metal matrix composites for linear and no-linear properties. In the case of quasi-brittle fracture properties, the RVE size is found to be about 8–10 times the linear RVE size. The approach is flexible enough to be applied to linear and non-linear properties allowing one to exhibit a correlation factor between linear and non-linear RVE.

The numerical estimates of the effective linear properties of random composites are more accurate in the case of small volumes subjected to periodic boundary conditions, if a sufficient number of realizations are considered. Sab and Nedjar [118] proposed a qualitative convergence criterion for the numerical finite element simulation of a two-phase composite. This type of numerical estimates requires statistical methods to analyze the results, such as: χ^2 criterion [119], and the two-point probability [120].

Sab and Nedjar determined the homogenized elasticity tensor C^{hom}, associated with each periodic realization ω^L. Tensor C^{hom} has ensemble average $C^{\text{hom},\,L}$ and can be classically obtained with the standard periodic homogenization. The analysis is restricted to two-phase composites, for which V^L is the cube centered at the origin with sides of length $L > 0$ parallel to the canonical basis. The rate of convergence of $C^{\text{hom},\,L}$ to C^{hom} depends on the adopted periodization sequence and convergence up to a given relative error may occur for unit cell size larger than the minimum RVE size. Numerical estimates for ensemble average of matrix volume fraction φ are also provided.

An L –periodized sample of the above described inclusions-matrix composite is generated as follows: first, the number N of inclusions centers in V^L is generated according to the Poisson integer random variable. Then, N centers are uniformly distributed in V^L and they are extended to the whole space by L –periodicity. It can be proved that the L –periodized medium is statistically invariant.

The convergence of $C^{\text{hom},\,L}$ to C^{hom} is slower for phase contrast 100. In this case, the overall shear modulus is twice the Hashin-Shtrikman lower bound and one fifth the upper bound. Analysis of numerical calculations indicates that the normalized correlation function for $L/R_{RVE} = 10$ is very

small outside a circular domain of radius R_{RVE}. Similar result is obtained for phase contrast 10. This plaids for a minimum RVE size equal to $2R_{RVE}$ in agreement with the two-probability function estimation.

Marcos-Gómez et al. [121] compare the predicted values of the thermal conductivity of composite made using the differential effective approach, mean field approach, and the finite element method. The effects of inclusion anisotropy, inclusion orientation distribution, thermal interface conductance, and inclusions dimensions have been considered. The objective of study has been to use a range of modeling methods to evaluate the effect of fiber anisotropy and interfacial thermal contact resistance into the global thermal properties of a Cu matrix composite reinforced with carbon nanofibers.

The results have been contrasted with results, obtained through mentioned homogenization methods for RVE. Comparisons have been made for cylindrical and spherical inclusions.

The thermal interface conductance is implemented by replacing the inclusion with a non-ideal interface by an effective inclusion with thermal conductivity

$$\lambda_f^e = \frac{\lambda_f}{1+\lambda_f /\left(h_c a_f\right)}, \tag{40}$$

In order to separate the influence of the different parameters involved (size of reinforcement, volume fraction, phase contrast, interface thermal conductance, anisotropy of the reinforcements), the comparison has been made first with spherical inclusions and then with short fibers represented by cylinders.

The composite thermal conductivity λ_c given by mean field approach for a spherical inclusion is the same as that derived by [51]:

$$\frac{\lambda_c}{\lambda_m} = \frac{\varphi^e\left(1+2\varphi\right)+2\left(1-\varphi\right)}{\varphi^e\left(1-\varphi\right)+\left(2+\varphi\right)}, \tag{41}$$

where $\varphi^e = \lambda_f^e / \lambda_m$.

The differential effective approach counterpart is given by

$$1-\varphi = \frac{\left(\varphi^e - \frac{\lambda_c}{\lambda_m}\right)}{\left(\varphi^e - 1\right)}\left(\frac{\lambda_c}{\lambda_m}\right)^{1/3}. \tag{42}$$

Isotropic spherical inclusions with different thermal conductivities have been considered as a function of the thermal conductivity of the Cu matrix. Three different phase contrasts of 0.1, 1 and 10 have been studied, corresponding to λ_f values of 38.5, 385 and 3850 W/ (m·K), respectively. The length of RVE considered was 10 times the inclusion diameter which is enough to obtain representative results.

The finite element method tools were used to carry out a complete parametric study as a function of a thermal anisotropy of the inclusion and the interface conductance to identify the most important factors limiting the real thermal conductivity of Cu matrix composite reinforced with carbon nanofibers. The study compares the predicted thermal conductivities by finite element method and mean field approach for the three possible architectures (3D-random, planar-random and uniaxial) of a fiber reinforced composite for a fiber volume fraction of 0.28.

The predictions of the different approaches for spherical inclusions match perfectly at low volume fractions and begin to deviate at $\varphi \geq 0.3$. The differential effective approach consistently predicts higher values of thermal conductivity than the mean field approach, where the greatest relative difference (~18%) is observed at $\varphi \sim 0.7$. The values of φ, predicted by mean field approach tend to be lower than other prediction schemes.

The fiber length was fixed at 500 nm and the diameter at 100 nm. The RVE considered were cubes of side 900 nm. In the case of spherical inclusions their size is not relevant since the thermal contact at the interface is perfect. The predictions of the different calculation models

(differential effective approach, mean field approach, and the finite element method) match perfectly at low volume fractions and begin to deviate at an inclusion volume fraction of 0.3.

The effect of interface thermal conductance on the composite thermal conductivity observed for volume fractions φ = 0.2 and φ = 0.4, considering λ_f = 3850 W/(m·K). The conductivity shows an asymptotic behavior both for low and high conductance. Therefore, three regions can be identified; two plateaus for high and low values of h_c and a transition zone. For low h_c the composite behaves as a porous material whereas for high h_c the composite material with a perfect interface. The position of transition zone depends strongly on the inclusion size, with smaller inclusions showing more interface dominated behavior.

The predictions of mean field approach and finite element method match within 3%, except in the directions where there is a substantial fraction of fibers in the direction of the heat flow, in which case the finite element method predicts lower values (12% and 14% lower in the planar and uniaxial cases, correspondingly). In the case of short fiber reinforced composite the most important parameters controlling the thermal conductivity are the interface thermal conductance and preferred orientation of the fibers.

A procedure for predicting the thermal conductivities of composites through a combined approach of the RVE method and heat transfer analyses via finite element is presented in [122–138].

Insufficiently investigated aspects of the influence of the arrangement of inclusions on the thermo-physical characteristics of composites lead to a considerable spread in the estimates of the effective thermal conductivity of the composite in different directions, especially in the presence of elongated inclusions (fibers) and with a large difference in the thermal conductivity of the inclusions and the matrix [139–154].

The value of the effective thermal conductivity of a composite can vary over a wide range for different spatial distributions of the filler in the matrix, even at the same concentration [155–160].

Yang et al. [161] applied the inverse algorithm based on conjugate gradient method and discrepancy principle to estimate the unknown time-

depended heat flux and temperature distribution for the system composed of a multi-layer composite strip and semi-infinite foundation, from the knowledge of temperature measurements. The direct problem, concerned with the determination of the medium temperature when the heat flux, thermos-physical properties of the multi-layer composite strip with periodically repeated cells, and initial and boundary conditions are known [162–166], considered in study. Ching et al. provided the inverse analysis to predict the unknown time-depended function of intensity of the heat flux, merely from the knowledge of medium and boundary temperature.

Numerical results confirm that the proposed method can accurately estimate the time-depended heat flux and temperature distributions for the problem even involving the inevitable measurement errors. For the cases considered in this study, an increase in measurement error does not cause the obvious deterioration on the accuracy of the inverse solution. The results of calculations indicate that the temperature rises rapidly at the outer surface of the composite strip as a consequence of the rapid rise of its internal energy by heat flux, but it drops sharply as the distance from the outer surface increases.

Gori et al. [167] employed a theoretical model to evaluate the thermal conductivity of fiber reinforcement composite with ceramic-silica matrix under two thermal assumptions which allow to solve the heat conduction equation. This theoretical approach employs the cubic cell model with parallel isothermal and heat flux lines. The elementary cubic cell of the material is presented in three dimensions with fiber reinforcement in the middle and the ceramic-matrix around. Authors explored the heat conduction equation in the three dimensions for a non-isotropic material

$$j_i = -\lambda_{ik} \nabla T_k, \; i = x, y, z \, . \tag{43}$$

The heat conduction equation was solved under the two thermal assumptions of parallel isothermal lines, and parallel flux lines. The assumption of parallel isothermal lines means that the thermal conductivity in the transversal directions, i.e., on the isothermal plane, is infinitively high. The assumption of parallel flux lines means that the thermal

conductivity in the transversal direction, i.e., orthogonal to the heat flux is zero. A mathematical expressions for the total heat transfer in *x*, *y*, and *z* directions of composite sample, as well as the effective thermal conductivities were derived.

The theoretical model and numerical simulations include the values of the thermal conductivity of the fiber which differ by several orders of magnitude. This allows studying the effect of the ratio between the thermal conductivities of the fiber and the matrix. Experimental results indicate that the effective thermal conductivity in x-direction has higher values for parallel isothermal lines, while the numerical simulations are intermediate between the two thermal assumptions. Gori et al. defined the anisotropy degree as the ratio λ_x/λ_z, and anisotropy efficiency as the ratio between the fiber and matrix conductivities. The anisotropy degree increases with the consumption of the layer of silica, reaching the maximum at the complete consumption of the upper layer. The anisotropic efficiency of the composite linearly decreases with the increase of the potential anisotropy of the two materials. The anisotropic efficiency reaches a minimum for $\lambda_f/\lambda_m > 100$, which is dependent only on the geometrical parameters of the composite.

The foregoing is the reason for the transition in the study from averaged macro thermos-physical characteristics to local characteristics of composites. Local heat fluxes that are associated with individual inclusions and regions between them are an example of such micro characteristics.

It is obvious that the description of heat transfer by means of local heat flux (LHF) in a randomly inhomogeneous medium can only be statistical. At the initial stage of developing this approach, it is required to study the statistical characteristics of various parameters of LHF.

Heat conduction management for composites is still in its infancy. The influence of heat fluxes in the inner regions of the composite on the effects of heat transfer is obvious. The possibility to take into account the influence of the local heat fluxes spatial distribution on the average thermos-physical characteristics of the composite is important both for applied aspects and for the development of analytical models of heat transfer in composite media.

Chapter 3

NUMERICAL METHODS IN HEAT CONDUCTION

3.1. MESH METHODS

Numerical methods for finding the effective thermal conductivity of a composite material can be conditionally divided into two large groups. The first group of methods involves a numerical solution of the heat equation for fixed boundary conditions, as a result of which the temperature field is located. The finite difference method (FDM) [168–181] and the finite element method (FEM) [182–198] are the most popular in the whole variety of numerical methods for solving partial differential equations of the heat conduction type [199–211]. The major advantage of the first method is the simplicity of implementation, but the solution of the equation is performed on a uniform rectangular grid, which leads to a large amount of computation, and unrecoverable errors in the case of the non-rectangular shape of the filler particles of the composite or the counting area itself. The above is the reason for using the finite element method in technical applications.

There are no restrictions on the geometry of objects for the finite element method [212]. However, in the case of the rectangular shape of all objects in the countable domain, both methods lead to equivalent results.

The simplicity of obtaining exact solutions in the case of anisotropic media and media with variable thermal conductivity is additional important advantage of the method of finite differences.

James et al. [213] modified the finite difference method to calculate the thermal conductivity of a composite in which the fibers can be at any angle to the faces of the sample. Authors calculated heat fluxes in regions, remote from boundaries, where the temperature gradient is uniform over an appreciable volume of material for the case of known thermal conductivities and temperature gradient. FDM can be also applying to study the media with variable thermal conductivity [214–228].

Elbarbary et al. [229] studied the effects of variable thermal conductivity on heat transfer from moving surfaces in a micro polar fluid through a porous medium with radiation. The governing fundamental equations of the thermal conductivity are solved numerically by using Chebyshev finite difference method [230–242]. The numerical results show that variable thermal conductivity has significant influences on the temperature profiles in cases of plane surface moving in parallel with the free stream and in the opposite direction to the free stream. The numerical results indicate that in the first case the temperature increases also as a variable conductivity parameter increases bat it decreases with permeability, variable viscosity and radiation increasing.

A hybrid numerical technique which combines the differential transformation ad finite difference method is utilized in [243] to investigate the annular fin with temperature-depended thermal conductivity. The results of calculations indicate that the increase in thermal conductivity leads to more uniform temperature distribution in the medium. The results reveal that convective heat transfer is the main effective heat dissipation mechanism under the convection-radiation condition. Thus, in spite of the above advantages of the finite element method, the finite-difference method has its own specific field of application.

Thus, the finite element method is more often used to numerically solve the heat conduction equation in composite materials with an arbitrary shape of the filler particles [244–256].

Islam et al. [257] systematically studied the applicability of FEM in predicting the effective transverse thermal conductivity of fiber reinforced composites. The numerical research was applied for the cases of square and circle cross-section fiber. Authors pointed out the next ideal model assumptions: the composites are macroscopically homogeneous; locally both the matrix and the filament are homogeneous and isotropic; the thermal contact resistance between the filament and matrix is negligible; the filaments are arranged in a square periodic array, i.e., they are uniformly distributed in the matrix. The last assumption implies that the filaments are equal and uniform in shape and size and are symmetrical about the x- and y-axes. Four boundary conditions to calculate by FEM the effective transverse thermal conductivities of the RVE were employed in study: 1) prescribed constant boundary temperature on both vertical boundaries; 2) prescribed constant temperature and prescribed constant heat flux at the vertical boundaries; 3) prescribed constant heat fluxes at both vertical boundaries; 4) prescribed constant vertical boundary temperatures and a linearly varying temperature on the horizontal boundaries. All the boundary conditions yield about the same results up to the fiber volume fraction 0.5 and thereafter first condition gives the highest thermal conductivity and thirst condition the lowest one.

The comparison with experimental results showed clearly higher thermal conductivity in the case of fiber volume fraction below 0.67. Authors pointed out the uneven distribution if fibers in the cross-section involving, e.g., contact of fibers leading to higher conductivity of the composite.

In composites with interfacial thermal barrier resistance the effective conductivity varies in a wide range depending on the interfacial conductance between fiber and matrix. The maximum reduction of the effective thermal conductivity may be as large as 50% then the interfacial conductance is reduced by two decades. Best fit with available experimental results was obtained for both circular and fibers when the dimensionless interfacial conductance is about 30.

Comparison of FEM results with available analytical and experimental results revealed that the effective conductivity of composites varies in a

wide range depending on the interfacial conductance between fiber and matrix. It was found that matrix crack parallel to the direction of heat flux would have no effect on thermal conductivity.

Song et al. [258] calculated the effective thermal conductivity of polymer composites filled with randomly disposed non-interacting carbon nanotubes. The RVE was constructed by assuming that the carbon nanotubes are dispersed homogeneously in the polymer matrix. It was assumed that the RVE contains a single nanotube. The calculation of the heat transfer through the RVE assumes the applying of finite element method. In this case, the asymptotic expansion homogenization method was used, with the help of which the transition from a heterogeneous medium to an effective homogeneous medium at the macro and micro scale of RVE is carried out. The reason for using this procedure is that the ratio of the length of a carbon nanotube to its outer and internal diameters was of the order of 10^3 and 3×10^3, correspondingly.

3.2. STATISTICAL METHODS

The second group of numerical methods for solving the heat transfer problem is represented by Monte Carlo methods [259–271]. The idea of using Monte Carlo methods for solving differential equations is to find a random process for which the numerical procedure of the solution coincides with the numerical procedure for solving a given equation [272–275]. An example of such a random process for the heat equation is the random walk of a Brownian particle.

We consider the Dirichlet problem for the temperature field $T(x, y)$ in some two-dimensional region without sources of internal heat release. In this case, the application of finite-difference approximation on a uniform orthogonal grid with step h reduces the problem to the calculation of temperatures at internal nodes $T_{i,j}$, where i, j are the indices of the internal nodes of the countable domain. The finite differences method provides the following value for the temperature $T_{i,j}$ of a homogeneous material

$$T_{i,j} = \frac{1}{4}\left(T_{i-1,j} + T_{i+1,j} + T_{i,j-1} + T_{i,j+1}\right). \quad (44)$$

The modification of the random walk method allows one to solve the Dirichlet problem. Haji-Sheikh and Sparrow [276, 277] considered the methods of a fixed and floating random walks.

A uniform orthogonal grid is superposed on the arbitrarily shaped two-dimensional region in the method of fixed random walks. This procedure is also applied to the finite differences method. All transition probabilities between nodes in a homogeneous material are considered to be 1/4. The boundary of the region is considered as an absorbing screen. The process stops when random-walking particle reaches a boundary of the region. The values of the function $\varphi_b(x, y)$ at the boundary are equal to $\varphi_{b;p,q}$ where p, q are the indexes of boundary nodes. The function $\varphi_b(x, y)$ can be considered as a random variable. Then the relation between the mathematical expectation $v_{i,j}$ of the function $\varphi_b(x, y)$ for all trajectories of particles starting the walk from the inner node of the region with the numbers i, j and the mathematical expectations obtained for all trajectories of particles starting the walk from the neighboring inner nodes of the countable domain, can be represented as

$$v_{i,j} = \frac{1}{4}\left(v_{i-1,j} + v_{i+1,j} + v_{i,j-1} + v_{i,j+1}\right). \quad (45)$$

It is obvious that formulas (44) and (45) have a similar form. Consequently, the quantities $T_{i,j}$ can be considered as the mathematical expectations $v_{i,j}$ of the function $\varphi_b(x, y)$.

For the case of a sufficiently large number N_p of particles whose trajectories begin at a fixed internal node (x_i, y_j) and terminate at the boundary, the value of $T_{i,j}$ can be estimated as

$$T_{i,j} = v_{i,j} \approx \frac{1}{N_p}\sum_{k=1}^{N} \varphi_b\left(x_p^{(k)}, y_q^{(k)}\right), \quad (46)$$

where $\left(x_p^{(k)}, y_q^{(k)}\right)$ is the exit point to the boundary of the particle with index k emitted from the node (x_i, y_j). Using formula (46), one can find a solution of the Dirichlet problem at a single point (x_i, y_j) without knowing solutions for the remaining points of the grid.

It should also be noted that each particle emitted from point (x_i, y_j) and passing through some node (x_m, y_n) can be viewed as a particle emitted from point (x_m, y_n). Thus, one can obtain solutions to the Dirichlet problem for all internal nodes of the grid through which a large number of random walking particles passed. In addition, the resulting set of trajectories of a walk can be used in accordance with (21) to obtain a solution with any set of boundary conditions $\varphi_{b;p,q}$.

Both FDM and the method of fixed random walks are difficult to apply for an arbitrary shape of the boundary.

The method of floating random walks is free from this shortcoming. The initial point of the walk for this method is chosen arbitrarily. The next point of the trajectory is chosen on a circle whose radius is equal to the smallest distance from the initial point to the boundary of the region. The process is repeated until the particle is at a distance equals to the capture section from the boundary of the region. It is important to note that for $N \to \infty$ the solution obtained by the floating random walk method tends to an exact solution, while the solution obtained by the fixed random walk method tends to a finite-difference solution, which in itself is approximate.

Zinsmeister and Pan [278] developed the inscribed figure method. The basic concept of the inscribed figure method involves dividing the conduction region into standard shapes, for which analytical solutions are known. Along the dividing lines of standard shapes and inside areas that do not have a standard shape, the Monte Carlo method is applied. Standard shapes would include squares, rectangles, triangles, and circles for which Green's function is known or could be calculated numerically. Thus the initial boundary value problem is reduced to a number of smaller problems in regions of standard shape.

In the case of an anisotropic material or an inhomogeneous material with inclusions scattered in the matrix, a method of floating random walk

creates difficulties in determining the probability of a particle jumping to the next point of the trajectory. In order to overcome these difficulties, in the method of fixed random walks it is assumed that the probabilities of jumps from a given node to adjacent ones are inversely proportional to the thermal resistance between them, and their sum should be equal to 1.

Cruz and Patera [279] presented a new first-principle framework for the prediction of effective properties and statistical correlation lengths for multi-component random media. The methodology is based upon a variation hierarchical decomposition procedure which recasts the original multi-scale problem as a sequence of three scale-decoupled sub-problems. The study is devoted to the computationally intensive mesoscale sub-problem, which comprises: Monte Carlo acceptance-rejection sampling; domain generation and parallel partition based on Voronoi tessellation; parallel Delaunay mesh generation; homogenization-theory formulation of the governing equations; and finite-element discretization.

Kowsary and Arabi [280] presented a Monte Carlo algorithm for the anisotropic heat conduction calculating, based on the fixed-step random walk.

Heat transfer in composites was studied by Fiedler et al. [281–283] using Einstein relation for thermal diffusion

$$D_e = \frac{< R^2 >}{2d_S \cdot t}, \tag{47}$$

where D_e is effective thermal diffusivity, d_S is dimensional structure, $<R^2>$ is the average mean square displacement of random-walking particles that occurred over the time t. The effective thermal conductivity λ_e is then obtained using the formula

$$\lambda_e = \frac{D_e}{\overline{\rho} C_e}, \tag{48}$$

where $\overline{\rho}$ is the average density, C_e is the effective specific heat of the multiphase material. The values $\overline{\rho}$ and C_e can be chosen arbitrarily in the case of a stationary transfer problem.

The probabilities of a walking particle jumps between nodes of a uniform orthogonal grid are determined on the basis of the diffusion coefficients given in the source nodes and receiver nodes. The authors compared the solutions obtained in this modification of the Monte Carlo method and analytical methods for materials with a regular structure and found that these solutions are in good agreement.

Reza Bahadori et al. [284, 285] developed this diffusion approach and modified the floating random walk method to analyze heat transfer in a composite material. The modified floating random method allows parallelization of calculations and gives a significant gain in comparison with the standard FEM. The modified floating random method and the standard finite element method are in quite good agreement.

Grove [286] modeled transverse thermal conductivity in continuous unidirectional fiber composite materials by combining finite element analysis and spatial statistical techniques. Author proposed the statistical model of composite which based on the concept of Voronoï cells. Composite was modeled as a collection of these cells. For a given fiber volume fraction, the composite was regarded as comprising many unit cells, each with different dimensions. Grove proposed mathematical expression for the squared coefficient of variation of the cell dimensions

$$\overline{C}_V^2(\pi/\varphi) = 3\varphi^2/\pi\left[1 + 2\int_0^1 u^{-3}\exp\left(-K\upsilon/\sqrt{u}\right)du\right] - 1. \qquad (49)$$

The constant K is defined by the probability density function of the distance from a fiber center to the boundary of the Voronoï cell. The function υ is associated with the 'excluded region' around each fiber center which can contain no other centers. The mathematical validity of the model was confirmed to volume fractions less than about 0.5. As the volume fraction increases, there is progressively less possibility for random

distribution of fibers, value of $\overline{C}_V^2$ decreases, and necessarily reach zero for hexagonal close packing.

The finite element model was used to solve the temperature distribution within the cell. Heat flux and the effective thermal conductivity of the primary cell is calculated by applying the finite element model. Calculations were made for fiber volume fractions $\varphi \subset [0.05 – 0.5]$. The numerical calculation then yielded a value for the effective thermal conductivity of the primary cell, and was repeated over a wide range of values for λ_f/λ_m. The numerical study results pointed out that the random distribution of fibers gives thermal conductivities significantly lower than those calculated from the primary unit cell. The fractional difference increases from about 1% at a volume fraction of 0.05 up to 8% at a volume fraction of 0.5, and appears to be nearly independent of the thermal conductivity ratio λ_f/λ_m. The author notes that the combination of finite element analysis and spatial statistical techniques has resulted in a model of transverse thermal conductivity in continuous unidirectional fibre composites containing randomly distributed reinforcement.

Boltzman lattice method has been widely used to investigate the effective thermal conductivity of porous media and composites [287–299]. Wang et al. [300] presented a full set of numerical methods for predicting the effective thermal conductivity of fibrous materials, which includes a random generation-growth method for generating micro morphology of fibrous materials based on existing statistical macroscopic geometrical characteristics and a highly efficient lattice Boltzmann algorithm. Authors considered a two-dimensional and two-phase fibrous material. They assumed each fiber is represented by a straight line located by its core position and orientation angle. The core distribution probability is defined as the probability of a point to become a core of fiber. The value of core distribution probability is strongly relative to the fiber number density. For the isothermal boundary treatment, authors followed the bounce-back rule of the non-equilibrium distribution

$$g_\alpha - g_\alpha^{eq} = -\left(g_\beta - g_\beta^{eq}\right), \tag{50}$$

where α and β represent opposite directions, g^{eq} is equilibrium distribution of the evolution variable g. The suggested approaches include a stochastic generation growth algorithm for producing the practical structures of fibrous materials, and a lattice Boltzmann model for solving the energy equations through the materials.

The effective thermal conductivity of 2D fibrous networks is analyzed for different given parameters. The study results show that the fiber orientation angle limit will cause the material effective thermal conductivity to be anisotropic and a smaller angle limit leads to a greater anisotropy. The effective thermal conductivity of fibrous material increases with the fiber length and approach a stable value when the fiber length is sufficiently long. The effective thermal conductivity differs for different fiber location distribution functions as well.

The effective thermal conductivity of composite materials with thermal contact resistance at interfaces is studied by lattice Boltzmann modelling in [301]. The partial bounce back scheme was revisited to obtain correct dimensional formula for thermal contact resistance. Xie et al. considered the concept of temperature "diffusing" through the multiphase lattice system to apply the thermal lattice Boltzmann method. The position-dependent temperature diffusivity $\tilde{\lambda}$ has the same value as the real thermal conductivity, but with a different dimension (m^2/s).

The local macroscopic temperature and heat flux at each node were statistically calculated using distribution of the evolution variable. The study results showed that the existence of thermal contact resistance lowered the effective thermal conductivity. Thermal contact resistance increased with the particle-particle interfaces. With a low thermal contact resistance, the effective thermal conductivity of composites decreased with the increasing particle size. However if the thermal contact resistance was not negligible, a smaller average size of particles led to a lower effective thermal conductivity of composites for a given volume fraction φ.

Thomas et al. [302] carried out a quantitative analysis of a globally transverse anisotropic unidirectional carbon fibre-reinforced polymer with a high volume fraction. The associated RVE for thermal conductivity predictions was estimated. Several spatial descriptors (fibre volume

fraction, pair correlation function, local area fraction distribution through Voronoï tessellation, covariance function) are used to characterize distribution of fibres location and reveal a weak level of anisotropy. A comparison of the results was made with those obtained for a random microstructure, so the deviation from the uniformity was graded with statistical parameters.

The studied material is a unidirectional laminate that has been laid up with 27 layers of carbon fibres/epoxy matrix. In a layer, all the fibres have the same orientation, and all the layers have a 0^o orientation. The fibres radii vary in the 2.8-3.9 μm range. Comparison between the microstructure of an ideal isotropic-fibre arrangement and the microstructure of the studied composite material was realized. The microstructure of the isotropic-fibre distribution (in the plane orthogonal to the fibre direction) was modelled as a random point pattern. In a composite a hard-core model is employed since two fibres cannot be closer than a distance equal to the sum of their radii. The fibre radii dispersion and the fibre volume fraction were the ones measured in the experimental micrographs. The pair correlation function is defined for peculiar orientation (angle α) as follows

$$g_\alpha(r) = \frac{\sum_{k=1}^{N} n_{k,\alpha}(r)}{(r_1 \Delta r)\rho(N-1)}, \tag{51}$$

where $n_{k,\alpha}(r)$ is the number of fiber centers within distance $(r - \Delta r/2)/(r + \Delta r/2)$ from a reference fiber, N is a total number of fibers, ρ is the fiber density, and r_1 is the diameter of the channel in which the count is made.

Authors associated Voronoï diagram to a non-parametric statistical test to get RVE objectivity. The computation of fiber locations in composite matrix was realized using a classical iterative algorithm and took into account the edge effects. Results of study showed that the covariance function was a relevant descriptor to point out the anisotropy. The covariance plot for two orthogonal directions ($\alpha = 0^o$ and $\alpha = 90^o$)

highlighted significant differences mainly for small distances between fibers (< 100 μm). Authors have determined the RVE size considering the evolution of fiber area fraction, directional pair correlation function and effective thermal conductivities with the composite image size. The effective thermal conductivity calculations gave the estimation of RVE size (~ 280 μm).

3.3. MULTI-SCALE METHODS

Most composite materials are multi-scale in nature, i.e., the scale of the constituents is of lower order than the scale of the resulting material and structure. For most of the analyses of composite structures, effective or homogenized material properties are used; instead of taking into account the individual component properties and geometrical arrangements. These effective properties are usually difficult or expensive to measure and in the design stage the composition may vary substantially, making frequent measurements prohibitive. Hence a lot of effort went into the development of mathematical and numerical models to derive homogenized material properties directly from those of the constituents and from their microstructure. However, sometimes such analyses are not accurate enough. In principle it would be possible to refer directly to the microscopic scale, but such microscopic models are often far too complex to handle for the analysis of a large structure. A way out is what is now commonly known as multi-scale modeling [303–307], where macroscopic and microscopic models are coupled to take advantage of the efficiency of macroscopic models and the accuracy of the microscopic models. The scope of such multi-scale modeling is to design combined macroscopic-microscopic computational methods that are more efficient than solving the full microscopic model and at the same time give the information that we need to the desired accuracy.

An analytical and micromechanical modelling study was conducted by Srinivasan et al. [308] to predict through the thickness thermal conductivity of composite filled with diamond powder are developed and

validated. This research also includes an algorithm based on modified random sequential adsorption algorithm was developed to generate statistically isotropic unit cell of carbon fibre containing up to 60% of volume fraction in the RVE along with random distribution of spherical and ellipsoidal diamond powder particles embedded in the matrix based on the position and orientation. The effects of aspect ratio, shape and particle size on thermal conductivity of the composite were studied. The goal of unit cell generation algorithm was to generate random distribution of fibers in the unit cell which would be statistically equivalent to the actual carbon fiber reinforced plastic microstructure. Statistical functions were used to distribute the fibers in the RVE. 2D FEM models of RVE with unidirectional carbon fibers in the unit cell along with spherical and ellipsoidal particle filler embedded in the matrix were randomly generated. The diamond powder filler was generated randomly based on position and orientation within the matrix without overlapping. The fiber and the fillers were meshed using three node linear heat transfer triangular elements and the epoxy was meshed using four node linear heat transfer quadratic elements. Steady state heat transfer thermal analysis of composite was carried out using finite element software. The insulated surfaces prevented convection and the direction of heat transfer was perpendicular to lines of heat sink. The temperature distribution between both faces of composite across the distance 2*h* is

$$\Delta T = (1/2h)\int_{-h}^{h}[T(h,y)-T(-h,y)]dy\,. \tag{52}$$

The micromechanical analytical model was considered. The thermal conductivity of hybrid matrix of diamond powder/epoxy values according to these models is

$$\lambda_m{}' = \left[\varphi_m/\lambda_m + \varphi_f/\lambda_f\right]^{-1}. \tag{53}$$

In order to evaluate transverse thermal conductivity coefficient of the model, heat flux was calculated on the upper and lower faces of RVE and the thermal conductivity coefficient was determined by equation

$$\lambda_e = 2hj / T . \tag{54}$$

The numerical results showed that the fiber inclusions demonstrate a significant influence for the heat flux distribution in the RVE and the heat fluxes are concentrated through the fiber-filler interaction. A comparison of FEM and analytical model for the transverse thermal conductivity of the composite was carried out in the study. The analytical micromechanical models were mainly dependent on the thermal conductivity ratios and the volume fraction of the constituents.

The formulation and implementation of an extended finite-element method for random short fibre-reinforced composite materials have been proposed by Pike and Oskay [309]. A new enrichment function is proposed to incorporate the effect of random fibre inclusions within the extended finite-element method framework to eliminate the need of using finite-element meshes compliant with fibre inclusions. An extended finite-element method is based on the expression of the response field using the following approximation

$$u(x) = \sum_{a=1}^{n} N_a(x)\hat{u}_a + \sum_{b \subset L'} N_b(x)\psi(x)\hat{c}_b , \tag{55}$$

where u is displacements; N_a is the finite-element shape function associated with node *a*; *a* and *b* are the dummy indices of summation over all nodes and enriched nodes, respectively; ψ is the enrichment function; $\hat{u}_a$ and $\hat{c}_b$ are the nodal coefficients of the standard and enrichment shape functions, respectively; n is the total number of mesh nodes in a finite-element discretization; and L is the index set of enriched nodes. The first right-hand side term of this equation corresponds to the standard finite-element approximation of the response field, whereas the second part is the

enrichment to the approximation space based on a predefined enrichment function, ψ.

The enrichment functions of extended finite-element method have been employed in modeling the deformation response of short fibers embedded in a matrix. The fibers were idealized in study as rigid bodies going through only translation and rotation, but no bending and stretching. This condition may be imposed by considering the following constraint

$$g(x) := u(x) - u_c - (R - \delta)(x - x_c) = 0 , \tag{56}$$

where u_c is the constant vector of translation; R is the orthogonal tensor of rigid body rotation about the center of the fiber; and δ is Kronecker Delta. The orthogonal transformation imposed by the rigid body rotation constraint is valid for large rotations, but is a nonlinear constraint. The discretization of the trial and test functions follows the Galerkin method. The process was started by the decomposition of the problem domain into finite elements. In contrast to the standard finite-element approach, the mesh does not necessarily conform to the fiber domains, i.e., fibers are allowed to lie within the element domains. The constraint equation for the fiber indicates that the motion of the fiber is fully defined by a translation vector and a rotation angle.

The following possible cases of fibre positions were considered in numerical calculation: far field elements with no enrichment, partially enriched elements, and fully enriched elements entirely crossed by the fiber, fully enriched elements that contain fiber. In full enrichment cases, triangular sub-elements aligned with the fiber faces are used in the integration of a 2D quadrilateral. The number of integration points along the fiber (n_g^i) is determined using a heuristic formula as a function of the fiber length (l_i) and the mesh density (h_m) given as the approximation to the nearest even integer $n_g^i = \{(1.3 l_i / h_m)\}$. Only an even number of integration points are used to ensure that the no gauss point lies on the fiber center.

The numerical studies indicated that the sensitivity to the numerical integration of the constraint equation is the main factor leading to non-monotonic convergence. The demonstrated errors are point wise in contrast to the more traditional error characterization in which the errors over the entire problem domain are averaged. The highest errors within the model typically occur at the fiber tips. The errors at the fiber tips tended to decrease slightly as it moved across the domain, but clearly demonstrate the position sensitivity of the accuracy. The largest errors occur when the tips of the fibers are positioned at the center of an element. The numerical examples of this work verified the performance characteristics of the proposed extended finite-element method against the direct finite-element method.

Algorithms for automated meshing and unit cell analysis of periodic composites were introduced by Kim and Swan [310]. The hierarchical pixel/voxel meshing framework for periodic composites was extended in this study to achieve unit cell models of quadratic triangles (2D) or tetrahedra (3D) using combinations of element splitting and nodal shifting. Two of the most significant and challenging aspects of constructing meshes for general unit cell analysis of periodic composites are those associated with achieving full compatibility between the matrix and reinforcement phases (the two-way meshing problem), and that of applying periodic boundary conditions to the unit cell. To highlight the general two-way meshing problem, it is helpful to consider the plane weave composite with orthogonal inserts. Meshing of the individual yarns in this unit cell model is actually quite simple, starting with a circular cylinder for each yarn and then applying a sequence of distortion, translation, and rotation transformations. Within the context of a standard FEM framework, attention is devoted here to solving the two-way meshing problem for unit cell or RVE models containing internal surfaces of discontinuity. In FEM and extended finite-element method the approximation functions are enriched using partition of unity concepts to incorporate local analytical solution characteristics in the vicinity of inclusions or discontinuities.

In a three-dimensional spatial domain, the material region occupied by the *R*-th reinforcing fiber or particle can be described mathematically either

with a single function $F^R(X): \Omega_s \mapsto \Re$ or a set of different functions as follows

$$\Omega^R = \left\{ X \subset \Omega^S \,\middle|\, F^R(X) < 0 \right\}. \tag{57}$$

These mathematical representations permit one to test whether any given material point lies inside of a specific reinforcing object *R* or outside of that object. The material points *X* lies inside of the *R*-th reinforcing object when $F^R(X) < 0$.

The textile composite unit cell model is composed of four woven yarns and nine orthogonal inserts. It is here assumed that each yarn was initially a straight cylinder with an elliptical cross-section, but then deformed so that the center-line curve is sinusoidal and so that cross-sections remain orthogonal to the original axis of the cylinder. In addition, the center-line curve of the yarn lies on a user-defined, $\xi\eta$ -plane. The mathematical description of each woven yarn in local co-ordinates can be written as

$$\Omega^R = \left\{ X \,\middle|\, F^R(X) < 0 \right\} = \left| \xi \right| \hat{F}^R(\xi) < 0, \tag{58}$$

where

$$\hat{F}^R(\xi) = \left(\frac{\eta - C_L(\xi)}{r_\eta} \right)^2 + \left(\frac{\zeta}{r_\zeta} \right)^2 \tag{59}$$

and center-line

$$C_L(\xi) = l_\eta \left(\frac{2\pi\xi}{l_\xi} \right). \tag{60}$$

In the preceding, r_η, r_ζ, are radii of the yarn's elliptical cross-section in local directions η, and ζ, respectively, and l_ξ, l_η are the amplitude and wavelength of the sinusoidal curve C_L (ξ) that defines the centerline of woven yarn object in local co-ordinates $\xi-\eta$.

The fiber director is assumed parallel to the yarn's center-line curve and is constant over each elliptic cross-section perpendicular to ξ-axis. Accordingly, the material director of point ($\xi\eta\zeta$) in $\xi\eta\zeta$-co-ordinates can be expressed as

$$\hat{d}(\xi)=\left\{1+\left[\left(2\pi l_\eta / l_\xi\right)\cos\left(2\pi\xi / l_\xi\right)\right]^2\right\}^{-0.5}\times \\ \times\left[1,\left(2\pi l_\eta / l_\xi\right)\cos\left(2\pi\xi / l_\xi\right),0\right] \quad (61)$$

It was assumed that a given unit cell model can initially be meshed with hierarchical pixel (in 2D) or voxel (in 3D) meshing techniques.

All pixels were splitted into triangles and all voxels into tetrahedra without regard to the location of material interfaces. In two dimensions, individual four-nodded pixels without hanging nodes can simply be diagonally bisected with no additional concerns about displacement field continuity between adjoining triangles, and if the original pixels are square, then the triangles resulting from splitting will have aspect ratios of $\sqrt{2}$, where here aspect ratio is defined as the ratio of maximum to minimum edge length. The essential techniques used in subdivision of pixels into triangles generalize directly to three-dimensions where voxels and their quadrilateral faces are split into tetrahedra.

In the current framework, the mesh of the unit cell was constructed in three stages: a) creation of the background pixel/voxel mesh; b) splitting of pixels/voxels into triangles/tetrahedra to form the base-triangular or tetrahedral mesh; and c) additional node-shifting and element splitting to achieve the final triangular/tetrahedral mesh. To demonstrate the robustness and efficacy of proposed meshing techniques, three different types of composite unit-cells are modeled in [310]: an aligned fiber composite at very high fiber volume fraction φ_f, achieved using multiple

fiber diameters; a particulate composite at moderately high volume fraction of reinforcement; and a three-dimensional continuous textile-reinforced composite material.

The above methods were applied in three-dimensions to create the unit cell of Si–C and In–Sn composites. The inclusions are assumed to be spherical, of uniform size, and arranged in a face-centered cubic pattern, which gives up to about 70% volume fraction when uniform particles are closely packed. The convergence behavior of the computed elastic constants shows that the effective stiffness modules increase with increasing mesh refinement. This behavior is due to the fact that intermediates nodes of the quadratic tetrahedral elements were positioned midway along element edges, leading to truncation of the SiC volume fraction at low mesh resolutions.

Study results show that coarse meshes tend to underestimate the volume fractions of convex reinforcing objects, since their boundaries are approximated here as piecewise linear or piecewise planar. If the intermediate nodes of edges could be positioned to fall on material interfaces, as opposed to merely the midpoint of the segment connecting end nodes, then the quadratic elements used in this study would achieve piecewise quadratic approximation of material interfaces.

Hou and Wu [311] have considered a multi-scale finite element method for solving a class of elliptic problems arising from composite materials and flows in porous media, which contain many spatial scales. The method is designed to efficiently capture the large scale behavior of the solution without resolving all the small scale features. The second-order elliptic equation was considered

$$-\nabla a(x)\nabla u = f\,, \tag{62}$$

where $a(x) = a_{ij}(x)$ is the conductivity tensor and is assumed to be symmetric and positive definite with upper and lower bounds. This equation can be regarded as the equation of steady state heat conduction through a composite material, with *a*, and *u* interpreted as the thermal

conductivity and temperature. In practice, a may be random or highly oscillatory; thus the equation solution displays a multiple scale structure.

A set of nodal basis $\left\{\psi_K^i, i=1...d\right\}$ with d being the number of nodes of the element was defined in each element $K \in K^h$. In multi-scale method ψ^i satisfies

$$\nabla a(x)\nabla \psi^i = 0 \text{ in } K \in K^h. \tag{63}$$

By the homogenization theory the solution of examined equation has an asymptotic expansion:

$$u = u_0(x) + \varepsilon u_1(x,y) - \varepsilon \theta_\varepsilon + O(\varepsilon^2), \tag{64}$$

where $y = x/\varepsilon$ is the fast variable. Here, u_0 is the solution homogenized equation

$$\nabla a^* \nabla u_0 = f \text{ in } \Omega,\ u_0 = 0 \text{ on } \partial\Omega, \tag{65}$$

a^* is the constant symmetric and positive effective coefficient, given by

$$a_{ij}^* = \left\langle a_{ik}(y)\left(\delta_{ik} - \frac{\partial}{\partial y_k}\chi^j\right)\right\rangle, \tag{66}$$

and χ^j is the periodic solution of

$$\nabla_y \cdot a(y)\nabla_y \chi^j = \frac{\partial}{\partial y_i} a_{ij}(y) \tag{67}$$

with zero mean, i.e.б $\langle \chi^j \rangle = 0$.

Under certain smoothness conditions, one can also obtain point-wise convergence of u to u_0 as $\varepsilon \to 0$. The conditions can be weakened if the

convergence is considered in the $L^2(\Omega)$ space. Since in general $u_1 \neq 0$ on $\partial\Omega$, the boundary condition $u|_{\partial\Omega} = 0$ is enforced through the first-order correction term θ_ε, which is given by

$$\nabla a(x/\varepsilon)\nabla\theta_\varepsilon = 0 \text{ in } \Omega,\ \theta_\varepsilon = u_1(x, x/\varepsilon) \text{ on } \partial\Omega. \tag{68}$$

The base functions defined by equation

$$\nabla a(x)\nabla\psi^i = 0 \tag{69}$$

have the same asymptotic structure as that of u, i.e.,

$$\psi^i = \psi_0^i + \varepsilon\psi_1^i - \varepsilon\theta^i + \ldots,\ i = 1, d, \tag{70}$$

where ψ_0^i, ψ_1^i and first-order corrector θ^i are defined similarly as u_0, u_1, and θ_ε respectively. Multi-scale method converges to the correct homogenized solution in the limit as $\varepsilon \to 0$ and attains large error in the case of $\varepsilon \sim h$. The first-order corrector θ^k has a boundary layer structure when its boundary condition on ∂K has a high frequency oscillation with $O(1)$ amplitude. A proper boundary condition for the base function ψ^k was chosen in order to eliminate the due to the boundary integral boundary layer structure. In the special case when conductivity tensor is diagonal and separable in 2D, the base functions can be constructed from the tensor products of the corresponding 1D base. In this case the corrector θ^k does not have a boundary layer. This is a special example of obtaining the appropriate boundary condition without solving the cell problem.

It was pointed out that the multi-scale method gives the same rate of convergence as the linear finite element method when the small scales are well resolved, $h << \varepsilon$. When h does not resolve the small scales, the multi-scale method and the traditional finite element method behave very differently. The boundary condition of the base functions can have a big influence on the accuracy of the multiscale method. The oscillatory

boundary condition for the base functions in general leads to better accuracy than the linear boundary condition.

Steady heat conduction through a composite material with tubular fiber reinforcement in a matrix was considered in study. The base functions were chosen in order to resolve the smallest scales of the composite. The oscillation was localized in the circular region with fibers. Away from that region, the multiscale base functions are very close to the standard bilinear base functions since the conductivity is practically a constant. Numerical experiment results pointed out that the multi-scale finite element method is useful for general fiber composite problems. The efficiency of the above computation can be greatly improved by constructing the multi-scale functions only in the region of rapid oscillations.

A new finite element formulation has been developed by Ghost [312] for analysis of heterogeneous media, in which the second phase is randomly dispersed within the matrix. A tessellation based mesh generation technique to account for the arbitrariness in location, shape and size of the second phase was introduced.

A tessellation based mesh generator was developed to adequately account for the presence of the randomly dispersed second phase. Two-dimensional mesh generator is developed on the basis of Dirichlet tessellation of a domain to yield a network of Dirichlet cells or Voronoï polygons. This is a method of subdividing a Euclidean space into n-dimensional bounded convex polytopes. It may be perceived as the production of a network of interfaces formed by the impingement of expanding hyperspheres about random nuclei that are growing at a uniform rate from zero. If second phase inclusions are realized to be points in space, the convex polytopes (polygons in two dimensions) resulting from this discretization would encompass one inclusion.

Dirichlet tessellation is defined as the subdivision of a plane, determined by a set of points such that each point has associated with it a region of the plane that is closest to it than to any other. Then the interior of the Voronoi polygon associated with the labeled point P_i is the region D_i defined as

$$D_i = \{x : |x - x_i| < |x - x_j|, \forall j \neq i\}, \tag{71}$$

where $P_1(x_1)$, $P_2(x_2)\ldots P_n(x_n)$ is a set of n distinct random points in plane. The aggregate of all such regions D_i constitute the Dirichlet tessellation in the plane. Each region may be perceived as the intersection of open half planes bounded by the perpendicular bisectors of lines joining the point P_i with each of its neighbors P_j. The boundary segment B_{ij} is common to the polygons for P_i and P_j and nearer to them than to any other labeled points in the plane, i.e.,

$$B_{ij} = \{x : |x - x_i| = |x - x_j| < |x - x_l|, \forall l \neq i, j\}. \tag{72}$$

The vertex V_{ijk} of the polygons is equidistant from three generating points P_i, P_j, P_k as

$$V_{ijk} = \{x : |x - x_i| = |x - x_j| = |x - x_k| < |x - x_l|, \forall l \neq i, j, k\}. \tag{73}$$

The Voronoi polygons that share boundary segments were called contiguous elements or polygons and the corresponding generating points were called contiguous points.

The tessellation for a finite number of points P_1, $P_2\ldots P_n$ inside a restricted window W to be made up of regions or tiles was characterized as

$$D_i = \{x \in W : |x - x_i| < |x - x_j|, \forall j \neq i, P_j \in W\}. \tag{74}$$

The labeled points considered in their algorithm were all assumed to lie within the window. The edges of the window may be represented by effective linear inequality constraints, which were used in unambiguous tile creation near the domain periphery.

A two-dimensional mesh generator was devised for plane sections of multi-phase materials which are assumed to consist of unidirectional fibers or particulates. Based on information regarding the boundary of the

domain, locations, shapes and sizes of the inclusions, discretization takes place automatically. Following the representation of the domain boundary, the tessellation algorithms create convex elements within the entire region. The tessellation algorithm was described in detail in the study. Both the complete global and incomplete local Voronoï cell finite element methods have produced satisfactory results for a wide variety of test problems. Furthermore, convergence is achieved through an increase in the degrees of freedom and incorporating more regularly shaped elements.

A numerical scheme, based on an isoparametric second-order finite element discretization of the unit cell heat conduction problem, to calculate the effective thermal conductivity of composite materials with general 3-D microstructures and interfacial thermal resistance was presented by Matt and Cruz [313]. The scheme is based on an isoparametric second-order finite-element discretization of the unit cell heat conduction problem. In study the finite-element methodology of Rocha and Cruz, originally developed to calculate the effective conductivity of unidirectional fibrous composites with interfacial thermal resistance, was extended in two important directions: the three dimensions are considered, and second-order isoparametric finite elements are employed to accurately treat curved geometries.

A statistically homogeneous composite was considered. The continuous and dispersed composite phases were, respectively, a solid homogeneous matrix of thermal conductivity λ_m occupying domain Ω_c, and solid homogeneous particles/fibers of thermal conductivity λ_{ij}^d, $i, j = 1, 2, 3$, occupying domain Ω_d. The particles/fibers have arbitrary shapes, and are orderly or randomly distributed within the matrix. An interfacial thermal resistance function R_I was present at the interface $\partial\Omega_s$ (a disconnected set) between the matrix and the dispersed phase. The composite extends throughout a macro-scale region $\Omega = \Omega_c \cup \Omega_d$ of characteristic dimension L, over which an external temperature gradient $\Delta T/L$ is imposed. The RVE of the composite microstructure is the locally periodic cell Ω_{pc}, which contains several particles and/or fibers of characteristic dimension l, which was commonly referred to as the micro-scale. The characteristic dimension

of the RVE was referred to as the mesoscale, denoted by L_R. The composite length scales were well-separated and, given statistical homogeneity, one can define the small parameter $\varepsilon \equiv L_R/L$ for the medium.

For steady state heat conduction in the medium described above, the non-dimensional strong form of the boundary value problem is

$$\begin{aligned} -\partial\left(\partial\theta^c/\partial y_i\right)/\partial y_i &= G_c \text{ in } \Omega_c \\ -\partial\left(\lambda_{ij}\partial\theta^d/\partial y_i\right)/\partial y_i &= G_d \text{ in } \Omega_d \\ -n_i^c\partial\theta^c/\partial y_i &= Bi\left(\theta^c-\theta^d\right)=Bi\left[\theta_\varepsilon\right]\partial\Omega_s \text{ in } \Omega_s \end{aligned} \quad , \tag{75}$$

were $\theta_\varepsilon = T_\varepsilon/\Delta T$; $\theta^c = \theta_\varepsilon\big|_{\Omega_c}$; $\theta^d = \theta_\varepsilon\big|_{\Omega_d}$; $G = \dot{g}L_R^2/\left(\lambda_m\Delta T\right)$; T_ε and g are, respectively, the temperature field and the volumetric rate of heat generation at the micro-scale; n^c is the unit vector locally normal to $\partial\Omega_c$ and pointing to the outside of Ω_c; Bi is the Biot number; $\lambda_{ij} = \lambda_{ij}^d/\lambda_m$ is the conductivity ratio. Numerical solution of the cell problem (a boundary-value problem with periodic boundary conditions) by the finite element method was divided into three steps: 1) domain and mesh generation, 2) finite-element discretization, and 3) solution of the resultant linear system of algebraic equations. The following cell microstructures were considered in study: ordered array of spheres, ordered array of perfectly-aligned prolate ellipsoids, ordered array of circular cylinders, and a disordered array of disoriented circular cylinders. Mesh generation comprises the subdivision of the cell domain Ω_{pc} into N_E non-overlapping conforming finite elements, each to domain Ω_e, $e = 1\ldots N_E$, such that

$$\Omega_{pc,h} = \bigcup_{e=1}^{N_E}\Omega_e \tag{76}$$

is the discrete approximation to the domain Ω_{pc}, where h is the interfacial thermal conductance function. Over each finite element, the solution of the cell problem is approximated by the interpolation of its values at the nodes. An isoparametric discretization implies that both the geometry Ω_{pc} and the

periodic temperature field were approximated by the interpolation functions. Quadratic polynomials are employed as the interpolants; hence, the finite element meshes are composed of 10-node quadratic tetrahedral. The use of quadratic interpolation functions is expedient: an improved representation of 3D curved surfaces (spherical, ellipsoidal, and cylindrical) is mandatory for an accurate numerical solution, especially for composites with a high thermal contrast between the constituent phases. Numerical results of study revealed that is more computationally efficient to sum directly the surface integral contributions to the appropriate entries of the global composite matrix, rather than to incorporate elemental contributions into the elemental stiffness matrices, and then perform direct stiffness summation with these elemental data structures. In the finite element code developed, three auxiliary data arrays for the construction of the global stiffness matrix and forcing vector are used: a) the array, which associates to each local mesh node of a tetrahedron Ω_e; b) the vector, which associates to each global node the corresponding degrees of freedom; c) the array, which associates to each local mesh node of a tetrahedron Ω_e the corresponding equation number.

The numerical predictions for the effective thermal conductivity of ordered array of spheres, ordered array of prolate ellipsoids, ordered array of circular cylinders, and disordered array were presented in study.

The numerical predictions have been validated against analytical results for the simple cubic array of spheres, and for the limiting cases when the ordered arrays of perfectly-aligned prolate ellipsoids of revolution and circular cylinders are thermally equivalent, respectively, to the simple cubic array of spheres and the square array of unidirectional fibers. The data indicate that the effect of the Biot number is more pronounced on the in-plane conductivities, than on the out-of-plane conductivity. The numerical results show that the magnitude of the interfacial thermal resistance significantly affects the effective conductivity of composite materials.

The complexity and heterogeneity (inclusions) of composite materials often cause costly computational efforts. FEM and FDM are widely used to evaluate the heat transfer problems. FEM is recommended in case of

thermal analysis of composite structures. FEM has advantages when dealing with complex geometry and loading but its formulae and programming are more complicated. Nevertheless it should be mentioned that FDM has been successfully applied by many users. They have gathered broad experience in skilful heat conductivity modelling. The formulae for FDM are relatively simple, and the execution of FDM programmes is rapid. As the configurations of composite matrix with inclusions are not so complicated in our model, the FDM is applied in our research.

The results of our study indicate that the Monte Carlo method, combined with the FDM, is a powerful numerical technique for heat transfer modelling in irregular composites.

Chapter 4

RESEARCH METHOD

4.1. NON-RANDOM-WALK MONTE CARLO METHOD

Two-component composite material, with matrix thermal conductivity λ_m was investigated as a computational model. Square shaped thermal inclusions with a thermal conductivity $\lambda_f << \lambda_m$ were placed randomly in the binder matrix. Inclusions location in the material was done using a random number generator built into the Delphi® compiler and was equiprobable. Two algorithms of the random inclusion placement were used in the calculations. The first algorithm allowed receiving isolated inclusions. Each newly placed inclusion was prohibited to contact with existing inclusions. Thus, there was a matrix layer around each inclusion, which minimum thickness was set as a parameter. The second algorithm allowed inclusions to contact with each other. In this case, inclusions could contact their faces and can gather in clusters.

For each realization of the random placement of the inclusions (for each test) we solved numerically the internal Dirichlet problem in a two-dimensional rectangular area. The Dirichlet problem includes the stationary heat equation in the interior of a given region and the prescribed temperature setting on the boundary of the region. The Fourier's law of heat conduction in composite's area Ω with heat conductivity λ_Ω and temperature T_Ω can be expressed as

$$\nabla \cdot \left(\lambda_{\Omega} \nabla T_{\Omega} \right) = -w_{\Omega}, \tag{77}$$

where w_{Ω} is volumetric heat source.

We have considered the problem of thermal conductivity in a composite in the absence of heat sources: $w_{\Omega} = 0$.

To minimize errors accumulated in iterative cycles, we used non-dimensional variables: relative thermal conductivity

$$\kappa = \lambda_{\Omega} / \lambda_{m} \tag{78}$$

and relative temperature

$$\theta = T_{\Omega} / T_{C}, \tag{79}$$

where T_C is a characteristic temperature for the problem to be solved. In these dimensionless variables, the two-dimensional heat equation can be written as

$$\frac{\partial}{\partial x}\left(\kappa(x,y) \frac{\partial \theta(x,y)}{\partial x} \right) + \frac{\partial}{\partial y}\left(\kappa(x,y) \frac{\partial \theta(x,y)}{\partial y} \right) = 0, \tag{80}$$

where $\kappa(x, y)$ can take the values 1 or λ_f/λ_m.

Equation (80) was solved by the method of top progressive relaxation on a uniform rectangular grid. As a result of each test, we calculated the temperature field within the region and determined the effective relative thermal conductivity of the material.

For a large number of tests we built statistical distribution of the probability p that the effective relative thermal conductivity was in a certain range of values. The probability was estimated as $p_m = \nu_m/\nu$, where ν_m is the number of tests for which the relative thermal conductivity was into a range of values $[\kappa_{m_R} - \xi; \kappa_{m_R} + \xi)$, m_R is integer index, which enumerated the range of relative thermal conductivity values, ν is the total

number of tests, ξ is the half-width the range of values. The probability density (or the distribution density) was estimated as the ratio of the probability to the width of the interval

$$\rho\left(\kappa_{m_R}\right)=\frac{p_m}{\xi}. \tag{81}$$

Next, we determined the following characteristics of the above mentioned distribution: average value $\overline{\kappa}$, standard deviation σ', the coefficient of variation

$$\vartheta=\frac{\sigma'}{\overline{\kappa}}, \tag{82}$$

skewness α_3

$$\alpha_3=\frac{\nu}{(\nu-1)(\nu-2)}\sum_{i=1}^{\nu}\left(\frac{\kappa-\overline{\kappa}}{\sigma'}\right)^3, \tag{83}$$

and kurtosis α_4

$$\alpha_4=\frac{\nu(\nu+1)}{(\nu-1)(\nu-2)(\nu-3)}\sum_{i=1}^{\nu}\left(\frac{\kappa-\overline{\kappa}}{\sigma'}\right)^4-\frac{3(\nu-1)^2}{(\nu-2)(\nu-3)}. \tag{84}$$

The temperature gradient ∇T_α in the direction of the angle α with respect to the axis X in an elementary volume of anisotropic medium with a thermal conductivity κ_α causes only one local heat flux $d\mathbf{J}$, which is described by the Fourier equation

$$d\mathbf{J}=-\kappa_\alpha\nabla T_\alpha,\ \alpha=\angle\left(X,\nabla T_\alpha\right). \tag{85}$$

Consider the region Ω of the composite, whose matrix, according to the Monte Carlo principle, is randomly filled with inclusions.

The stationary Fourier heat conduction equation for the region Ω, which does not contain heat sources or heat sinks, can be expressed in terms of the LHF density vector:

$$\nabla d\mathbf{J}\big|_{\Omega} = 0\,. \tag{86}$$

Suppose that a temperature difference ∇T_β is applied to this region in the β angle direction. In this case, the resulting heat flux in the β direction for the indicated region can be expressed by the modified probability density distribution functions $F_1(s')$ and $F_2(\varphi_c/s')$ for the spatial and angular components, respectively:

$$\mathbf{J}_{\Omega,\beta} = \int_{\Omega} d\mathbf{J} = \int F_1(s')F_2(\varphi_c / s')\nabla T_\beta d\Omega\, d\varphi_c \tag{87}$$

Functions $F_1(s')$ and $F_2(\varphi_c/s')$ can be represented as linear combinations of probability density distribution functions $f_1(s')$, $f_2(\varphi_c/s')$ for the spatial and angular components, as well as factors $a_1(s')$ and $a_2(\varphi_c/s')$, having the dimension of the thermal conductivity coefficient

$$F_1(s_c) = a_1(s')f_1(s'),\ \text{and}\ F_2(\varphi_c / s') = a_2(\varphi_c / s')f_2(\varphi_c / s'), \tag{88}$$

where $f_2(\varphi_c/s')$ is the probability density of passing a local heat flux in the direction of the angle φ_c, provided that it is observed in the spatial region s'.

Functions $f_1(s')$ and $f_2(\varphi_c/s')$ are determined by independent test parameters.

The size of inclusions having the shape of a square with side b; minimum distance d between inclusions; the concentration c of inclusions;

the ratio λ_m/λ_f of the coefficients of thermal conductivity of the matrix and inclusions, can be indicated as such parameters:

$$f_i(\gamma) = \prod_z f_{i,z}(\gamma) \begin{cases} z = b, d, c, \lambda_m / \lambda_f \\ \gamma = s', \varphi_c / s' \\ i = 1, 2 \end{cases} . \quad (89)$$

The thermal inhomogeneity of the various regions of the composite, as well as the non-isotropy of heat transfer, are the reasons for the multimodal character of the probability density distributions $f_1(s')$ and $f_2(\varphi_c/s')$:

$$f_1(s') = \sum_k f_k(s'_k), \; f_2(\varphi_c / s') = \sum_p f_p(\varphi_{c,p}). \quad (90)$$

Preliminary it is possible to distinguish the following characteristic regions of heat transfer in a composite: unperturbed matrix, inclusions, regions before and behind the inclusion (in the direction of heat flux $\mathbf{J}_{\Omega\beta}$), and regions between inclusions with increased flux density.

Directions that are parallel and perpendicular to the temperature gradient ∇T_β, two symmetrical directions for each of the angles of square inclusion from the regions before and behind the inclusion (relative to the heat flux $\mathbf{J}_{\Omega\beta}$) can be indicated as the characteristic directions of the local heat fluxes.

The numerical solution of equation (80) at fixed boundary conditions allows to calculate the temperature field $T(x, y)$, and then, using (85), to calculate the components of the LHF density vector of $j_{\Omega,x}$ and $j_{\Omega,y}$, along the coordinate axes x and y, respectively. The modulus of local heat flux density vector can be easily determined from its components:

$$|\mathbf{j}_\Omega| = \sqrt{j_{\Omega,x}^2 + j_{\Omega,y}^2} . \quad (91)$$

The density vector direction of LHF in the region Ω can be characterized by the angle φ_Ω of vector deviation from axis *x*. It's obvious that

$$\varphi_\Omega = \arctan \frac{j_{\Omega,y}}{j_{\Omega,x}}. \tag{92}$$

An investigation of the statistical distribution of the density of local heat fluxes in a composite material requires the solution of the heat equation (80) in a sufficiently large number of points uniformly located in the countable region.

In this situation, the numerical method for solving heat conduction problems, which is considered to be the most effective, namely, the Monte Carlo method with floating random walk does not solve the problem, since the coordinates of the walk points are dynamically generated, and the uniformity of their location in the countable domain is not guaranteed.

The Monte Carlo method with a fixed random walk on a uniform orthogonal grid more closely matches the requirements of the problem, but we must be sure that the walking particles emitted from the source node will pass through all the nodes of the counting domain in sufficient quantity.

Thus, it seems more convenient to use the finite-difference methods, with which we are guaranteed to obtain the result for each node.

We separately note that to find the field of directions of density vectors of local heat fluxes; it is convenient to solve equation (80) on an orthogonal grid with step *h*. This orthogonal grid is oriented along coordinate axes.

We consider heat flux through the neighborhood ($x \pm h$, $y \pm h$) of computational grid node (x, y) as local heat flux in the composite matrix. Thus, in this situation, it is possible to use the finite difference method. It is convenient to choose rectangular shape of the two-dimensional region filled with the matrix material and square-shaped inclusions.

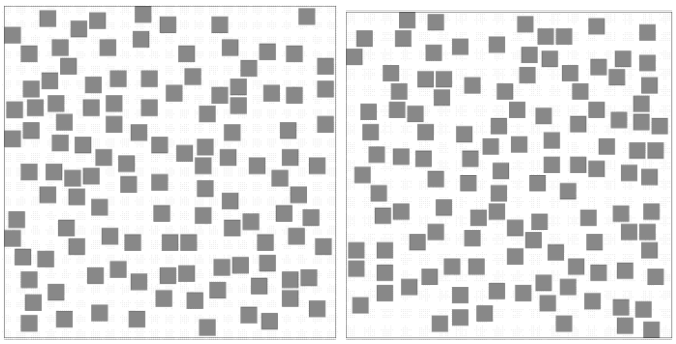

Figure 1. Example of two templates with random placement of inclusions: N = 117, a = 160h, b = 8h, and d = h.

We generated a square-shaped template with a side of the square equals to *a*. The side of the square was equal to the integer number of steps of the rectangular grid. The value of side varied in our numerical experiments from 128*h* to 1024*h*.

The square-shaped inclusions with equal side *b* have been placed in the template, using the random number generator with an equally probable distribution law. The minimum value of *b* is 4*h*; the maximum value is 32*h*. The inclusions placement algorithm sets sizes of the inclusions and their number *N* in the template, as well as minimum distance *d* between the inclusions. The values of *d* change from *d* = 0 (non-isolated inclusions) to *b* – *h*. Figure 1 shows two examples of composite matrixes with inclusions sizes are *a* = 160*h* and *b* = 8*h*, respectively. The minimum distance between inclusions is *d* = *h.* The number of inclusions in these templates is *N* = 117.

Figure 2 shows a fragment of the template with a superimposed grid. The mesh and the boundaries of the filler particles are oriented along the *x*- and *y*-axes. The index *j* numbers the grid nodes along the *x* axis, the index *i* numbers the grid nodes along the *y*-axis. The boundaries of the filler particles are located in the middle between the nodes of the counting mesh. When calculating the temperature field and local heat fluxes, the following rule is used: if two adjacent nodes, between which the heat energy is transferred, are inside one component of the composite material, namely in

the matrix or in the filler particle, then the thermal conductivity in the heat flux path is taken to be equal to the thermal conductivity of the matrix λ_m or the thermal conductivity of the filler λ_f, respectively.

If the matrix-inclusion boundary passes between two adjacent nodes, as for example between nodes ($j = m + 1$; $i = n$) and ($j = m + 1$; $i = n + 1$), then the thermal conductivity in the path of heat flux between these nodes were assumed to be equal to the average arithmetic thermal conductivity of the material components $\left(\lambda_m + \lambda_f\right)/2$.

Thus, we did not introduce additional interface thermal resistance, assuming the thermal contact between matrix and filler particles to be ideal.

The inclusions concentration in the template was considered as the ratio of all inclusions area to the total area of the template

$$c = \frac{Nb^2}{a^2}. \tag{93}$$

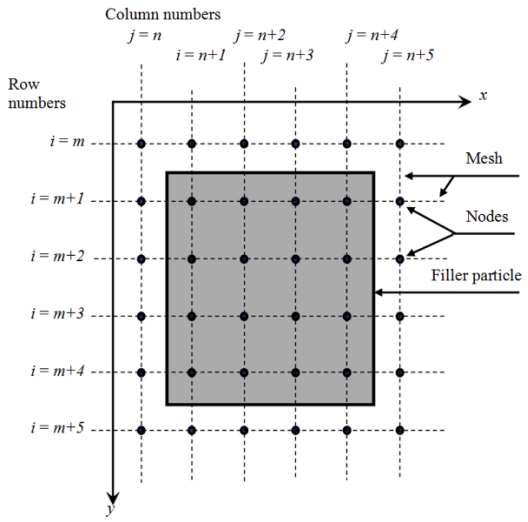

Figure 2. Fragment of the template with superimposed grid.

The Figure 1 shows the calculation results for $c = 0.5$. The ratio of the thermal conductivities of the matrix and the inclusions was $\lambda_m/\lambda_f = 21$ for all numerical experiments.

In order to minimize the errors associated with heat transfer at the boundaries, the calculated region of the modeled composite included three identical templates: central (representative) and two adjacent ones. The centers of these templates were located along the *y*-axis. On the perimeter of the calculation area, one layer of cells with size *h* was added. The computational model assumed that this layer has the thermal conductivity of matrix. Thus, the size of the computational domain along *x*-axis was $(a + 2)\ h$, and along *y*-axis was $(3a + 2)\ h$. Inclusions were not located on the outer boundaries of the calculated region. The computational grid node indices along *x*-axis assumed the values $j \subset [1; a + 2]$, and along *y*-axis $i \subset [1; 3a + 2]$. The scheme of calculated region is shown in Figure 3.

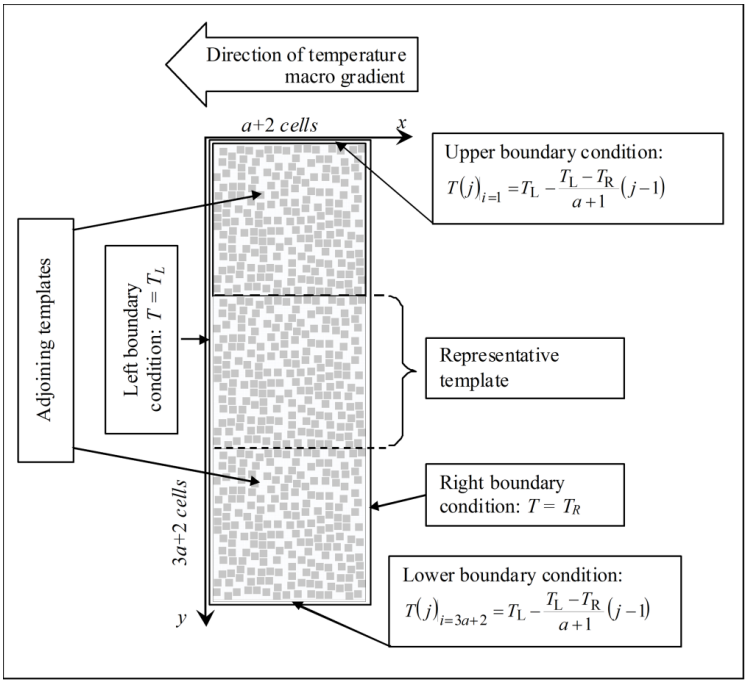

Figure 3. Scheme of calculation area.

We carried out the calculations under the assumption that the Dirichlet boundary conditions are satisfied at the boundaries. The left (j = 1) and right (j = a + 2) boundary layers of the composite matrix had constant temperatures:

$$\begin{aligned} T(i)\big|_{j=1} &= T_{\mathrm{L}} \\ T(i)\big|_{j=a+2} &= T_{\mathrm{R}} \end{aligned}. \tag{94}$$

At the same time, inequality $T_L > T_R$ holds. The vector directed along the normal from the less heated isothermal template surface to the warmer isothermal template surface and equals to the ratio of the temperature difference to the distance between these surfaces we called the temperature macro-gradient. Thus, the temperature macro-gradient was applied along x-axis. For the upper (i = 1) and lower (i = 3a + 2) boundary layers, a linear temperature change along x-axis was specified:

$$T(j)\big|_{i=1} = T(j)\big|_{i=3a+2} = T_{\mathrm{L}} - \frac{T_{\mathrm{L}} - T_{\mathrm{R}}}{a+1}(j-1). \tag{95}$$

The effect of the boundary layers i = 1 and i = 3a + 2 on the temperature fields in the countable region is shown in Figure 3. It shows the temperature distributions in the same column (j = 512) of the counting grid for representative and two adjoining templates of size a = 1024h, filled with inclusions of size b = 32h with a concentration c = 0.37 at the minimum distance between the particles of filler d = 8h.

The figure shows that the temperature profile of the column of the upper adjacent template differs somewhat from the temperature profile of the representative template in lines 1 to 300, and then they coincide with high accuracy. Similarly, the temperature profiles of the representative and lower adjacent template coincide in lines 1–700, and in lines 700–1024 there are discrepancies. The influence of the upper and lower boundary conditions on the temperature profiles and, consequently, on the local heat fluxes, extends about 1/3 of the template. Thus, the temperature profile of

the representative template in the counting domain can be considered undistorted.

We also note that due to the translational symmetry for counting region which includes above mentioned templates, the thermal fluxes between the layers for $i = a$ and $i = a + 1$ are exactly equal to the thermal fluxes between the layers for $i = 2a + 1$ and $i = 2a + 2$. Therefore, the calculation technique assumed a solution of equation (85) for the whole counting area and then the analysis of LHF only for the representative template $i \subset [a + 1; 2a + 2]$. All LHF values in this work are in conventional units, because to represent them in system units it is necessary to specify a certain value of h. The effective thermal conductivity of the representative pattern was calculated from the total heat flux passing through its left or right boundary. The value of temperature macro-gradient in calculation of λ_e can be replaced by $(T_L - T_R)/[(a+1)h]$. The total heat flux $\mathbf{J}_\Sigma$ at the boundary passes distance ah through an isothermal line. In this case, the effective thermal conductivity can be expressed by:

$$\lambda_e = \frac{(a+1)}{a(T_\mathrm{L} - T_\mathrm{R})} J_\Sigma . \tag{96}$$

The procedure for generating the described pattern with random placement of inclusions values of the placement parameters a, b, c and d we call test. For each test, we generated the inclusions pattern. Equation (80) was solved by the finite-differences method. The solution was considered to be obtained when the ratio (86) was fulfilled for each node of the computational grid with accuracy not worse than 10^{-5}. Formulas (91) and (92), as well as the values of the components of LHF density vector for each node of the computational grid, were used to determine the modulus of the local flux density vector and its deviation angle from x-axis. The effective thermal conductivity of the material was found from (96). All data were saved.

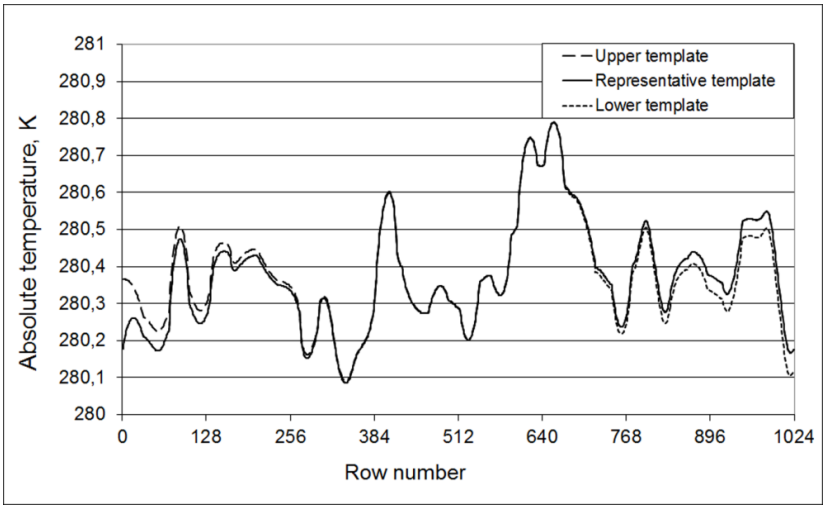

Figure 4. The temperature distribution along the column $j = 512$ in the representative and adjacent templates with a size $a = 1024h$.

The tests with the same parameters of inclusions placement we call series of tests. The number of tests in the series varied depending on the study objectives from 400 to 8000.

Because of the random placement of inclusions in each test, our research method can also be attributed to Monte Carlo methods in the sense that is commonly used in economic simulation tasks [314]. For the same reason, the local heat fluxes calculated by us can be considered as random variables. All the values of local heat fluxes in one series of tests were considered a sample from one general population. The value of the effective thermal conductivity obtained in each test was also interpreted by us as a random variable, and the set of values obtained in one series of tests was taken as a sample from the general population. The statistical characteristics of samples of the effective thermal conductivity, the modulus of the local heat flux vector, and the angle of deviation of the local heat flux from the x axis were investigated using standard statistical procedures.

4.2. VISUALIZATION IN HEAT CONDUCTION ANALYSIS

The study of the calculated maps of the modules of local heat fluxes density vectors and fields of their directions is another productive way of analyzing the results of modeling thermal conductivity processes in inhomogeneous materials. Flux maps provide important qualitative information that, even without being expressed in numerical measures, allows one to analyze specific heat transfer processes occurring in a matrix with randomly scattered inclusions.

In the case of a homogeneous matrix that does not contain an inclusion, the local heat fluxes in each node of the countable grid are equal in modulus of density and have the same direction. Such a state of the matrix will be called an unperturbed matrix. We will also use the term "ntensity" instead of the term "modulus of density vector" as applied to local heat fluxes.

In the case of inclusions with a thermal conductivity different from the thermal conductivity of the matrix, the local heat fluxes become inhomogeneous. In our numerical experiments, where thermal insulating inclusions with relative thermal conductivity $\kappa_f = \lambda_f/\lambda_m \approx 0.048$ were modeled, the spread of the intensity of local heat fluxes reached 1.5–2 orders of magnitude.

Figure 5 shows the LHF intensity map in test with parameters $a = 128h$ at $b = 16h$, $c = 0.094$ and $d = 14h$. This map was performed in 8-bit grayscale. Black, and white areas on this map correspond to the fluxes with lowest and highest intensity correspondently. Heat-insulating inclusions (black squares) and unperturbed matrix (light gray regions) are clearly visible on this LHF intensity map.

In addition, dark gray areas with reduced intensity of local heat fluxes to the left and right of inclusions are visible in Figure 5. It should be noted that in these regions the thermal conductivity of the medium is the same as in the region of the unperturbed matrix, but the intensity of the heat fluxes is much lower. We will call such domains a dark matrix. Since the total heat flux moves from left to right, the left, and right areas of the dark

matrix will be called the front region and the rear region, respectively. The regions with increased intensity of local heat fluxes are formed in the inclusion angles area.

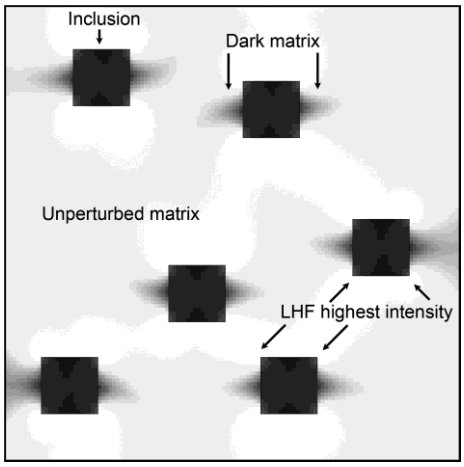

Figure 5. LHF intensity map in test: $a = 128h$, $b = 16h$, $c = 0.094$, and $d = 14h$.

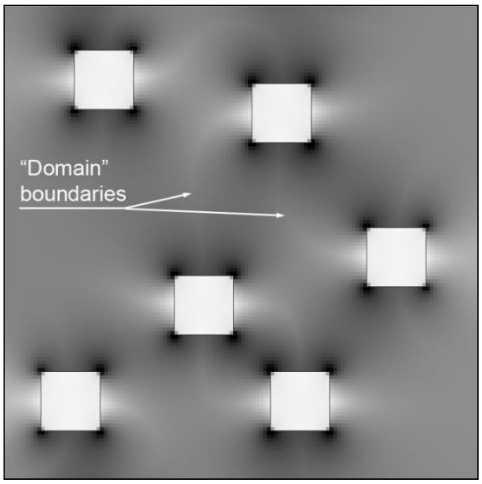

Figure 6. LHF intensity map (in gray scale) in test: $a = 128h$, $b = 16h$, $c = 0.094$, and $d = 14h$.

Figure 6 presents the flux map negative image with a non-linear blackening curve in test $a = 128h$ at $b = 16h$, $c = 0.094$ and $d = 14h$.

Such a map makes it possible to better detect the increase in the intensity of local fluxes in the region of inclusions angles. The fluxes map contains the outlines of the domain structure. The intensity of local fluxes is reduced at the boundaries of the domains located in the heat-conducting matrix. The computational model assumes the presence of square-shaped inclusions in composite matrix. The boundaries of domains begin and end at the centers of the sides of these squares.

Analysis of Figure 7 allows one to determine the nature of the dark matrix. Figure 7 shows the field of directions of local fluxes in the vicinity of a solitary inclusion. The directions field, calculated using formula (92), is indicated by arrows. The thickness of the arrows is proportional to the intensity of the local heat flux. Only eight gradations of intensity are displayed on this map, while the maps shown in Figures 5, 6 contain 256 gradations of intensity.

Local heat fluxes are shielded by inclusion in the rear region. This phenomenon is the cause of the formation of a dark matrix. For local fluxes flowing to the inclusion from the left, it is more advantageous to round the obstacle. Therefore, most part of the flux leaves the frontal area of the inclusion. Thus, a frontal dark matrix is formed. Local fluxes, flowing over the upper and lower side of the inclusion, form a region with increased intensity. Local fluxes flowing inside the inclusion still tends to come out of it, crossing the horizontal boundaries, and further enhances the intensity of fluxes, that envelops the inclusion. This increase in flux ceases to operate in the region of the middle of the horizontal boundary of the inclusion. Local fluxes again begin to penetrate into the inclusion through horizontal boundaries in the region of the right vertical boundary. Then, local fluxes exit through the right boundary of the inclusion into the region of the rear dark matrix. The foregoing is a mechanism for the formation of high intensity angular regions. These regions are clearly visible in Figure 6.

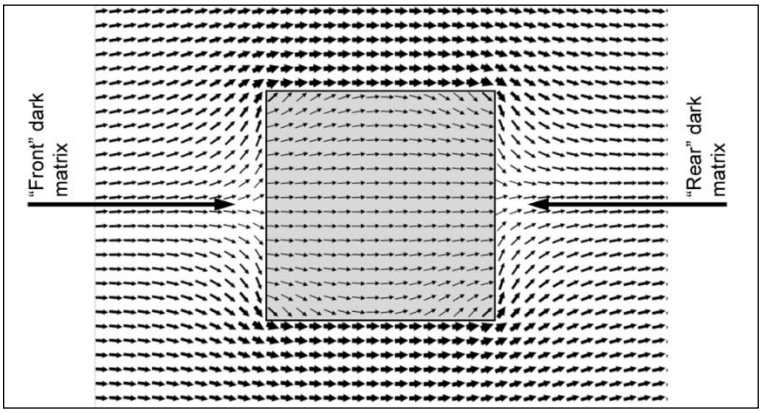

Figure 7. LHF directions field around the square filler particle.

In the case of low inclusions concentrations and large minimum distances between them the directions field and the density of local fluxes around each inclusion is not distorted due to the presence of surrounding inclusions. This situation reflects the concept of "non-interacting inclusions" used in Maxwell's generalized thermal conductivity theory and its numerous modifications. Figure 5 shows that the length of the region of the dark matrix on which the influence of the isolated inclusion extends is of the inclusion size order.

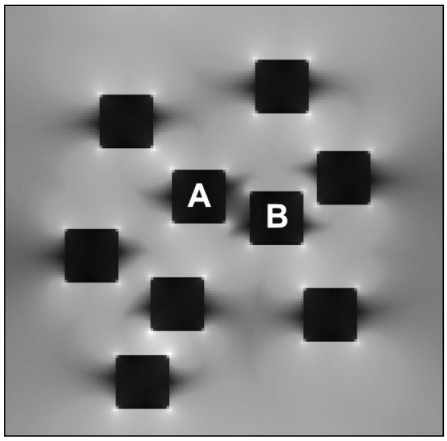

Figure 8. LHF intensity map in test: $a = 128h$, $b = 20h$, $c = 0.22$, and $d = 5h$.

Figure 8 shows the LHF intensity 8-bit grayscale map in test with parameters $a = 128h$ at $b = 20h$, $c = 0.22$ and $d = 5h$.

In contrast to the case shown in Figure 5, here we see two inclusions, marked “A” and “B”, about which it cannot be said that they “do not interact.”

The combined grayscale intensity map and the field of directions of local fluxes in the region of inclusions interaction are shown in Figure 9. Local heat fluxes flow mainly upwards in the region into the gap between the inclusions. Due to this maneuver, the general path of the heat flux in the matrix is somewhat longer.

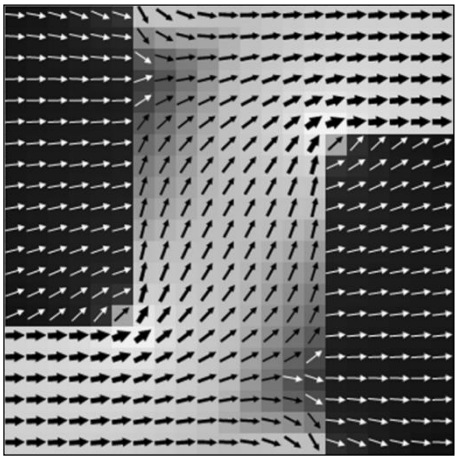

Figure 9. LHF intensity and directions map between interacting filler particles A and B from Figure 8.

The number of interacting filler particles is expected to increase with increasing concentration and decreasing the minimum distance between them. Figures 10 – 11 show changes in the conditions for the flow of local heat fluxes with a further increase in the concentration of inclusions. The figures show the fluxes maps of two tests of the same series. At $c = 0.33$, almost all inclusions interact with each other. And this interaction is not exhausted by the mutual distortion of dark matrices. Angular regions of increased intensity of local fluxes merge with each other, form sufficiently extensive channels with high flux densities. The length and number of

local channels depends not only on the random location of the filler particles, but also on the direction of application of the temperature drop at the boundaries of the region. Therefore, we call these heat conductive channels induced.

In Figure 10, there are three rather long channel designated Ch1, Ch2 and Ch3. The channels Ch1 and Ch2 are practically straight, without any significant lengthening of the path of the local flux.

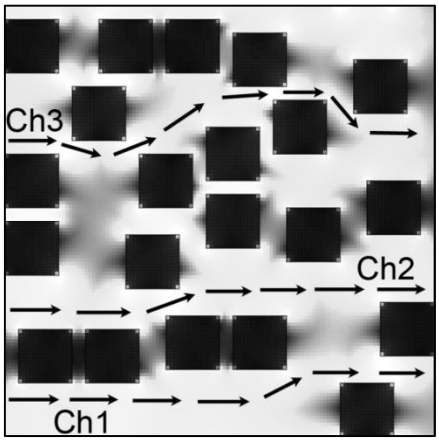

Figure 10 a. LHF intensity map in test 1: $a = 128h$, $b = 16h$, $c = 0.33$, and $d = 4h$.

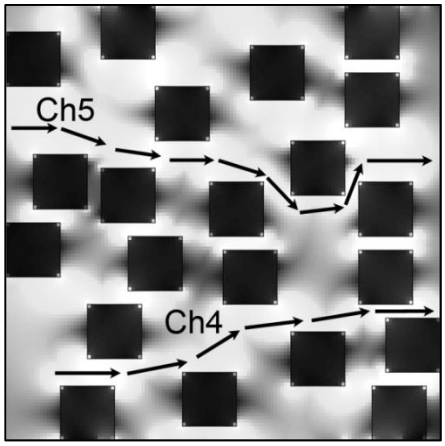

Figure 10 b. LHF intensity map in test 2: $a = 128h$, $b = 16h$, $c = 0.33$, and $d = 4h$.

In Figure 11, the situation is somewhat different: we see only 2 channels, Ch4 and Ch5, and they are less long and more curved than Ch1 and Ch2. The heat transfer conditions in the sample shown in Figure 10 are obviously more favorable than in the sample shown in Figure 11.

Thus, visualization of the solutions of the heat conduction problem in a random-inhomogeneous material makes it possible to understand how the placement parameters of the inclusions affect the conditions for the flow of local heat fluxes.

The formation of induced heat-conducting channels can be interpreted within the framework of the following heat-optical analogy. Consider, for example, the heat fluxes map shown in Figure 11. Here the heat fluxes move from left to right due to the temperature difference on the sides. Let us consider the case of heat-insulating inclusions. Two close-lying inclusions, labelled 1L1t and 1L1b, direct some of the total heat flux to the region A free of inclusions. Thereafter, the pair of inclusions 1L2t and 1L2b directs the main part of the heat flux from the region A to the region B free of inclusions. Inclusions 1L3t and 1L3b direct the heat flux from area B to the right boundary. The pairs of inclusions 1L1t – 1L1b, 1L2t – 1L2b, and 1L3t – 1L3b can be considered as elements that focus heat flow and direct it to the induced thermal channel 1. Consequently, these pairs of inclusions can be termed as thermal lenses of this channel. For clarity, we drew stylized lenses directly on the fluxes map of the induced channel 1.

A similar role is played by the pairs of inclusions 2L1t – 2L1b, 2L2t – 2L2b, and 2L3t – 2L3b. These pairs can also be considered as thermal lenses that focus heat fluxes and form the induced heat-conducting channel 2.

It should be noted that at least two heat insulating inclusions are required to form a thermal lens. Local heat flux will move between these inclusions. Due to the fact that the general direction of the heat fluxes in this case is horizontal, the thermal lens should conventionally include at least one "top" inclusion and at least one "bottom" one. Our labelling of inclusions contains this information. For example, marking 2L1b means

"second induced channel, thermal lens 1, and “bottom element", and 1L3t means "first induced channel, thermal lens 3, and "top element".

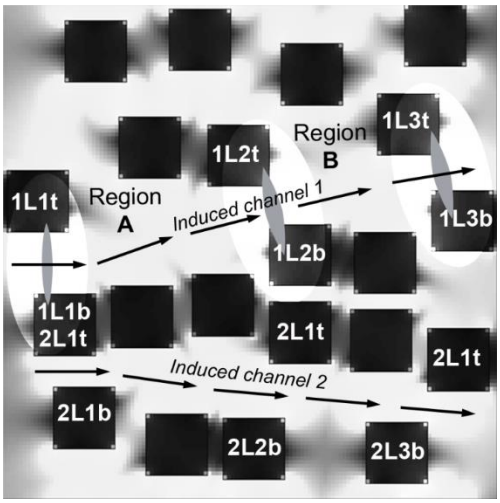

Figure 11. Visualization of the heat-optical analogy.

We also note that one and the same inclusion can be part of two thermal lenses, as happened with the inclusion of 1L1b/2L1t. This inclusion is simultaneously the lower element of the first thermal lens of the first induced channel and the upper element of the first thermal lens of the second induced channel.

Chapter 5

THERMAL CONDUCTIVITY OF TWO-COMPONENT 2D COMPOSITES

5.1. STATISTICS OF THERMAL CONDUCTIVITY DISTRIBUTION

Changing the random arrangement of inclusions in the matrix with the same placement parameters leads to spread in the value of the transmitted heat flux and, consequently, to scatter of the effective thermal conductivity of the material. Based on the results of a large number of tests for each series with certain placement parameters, we constructed the effective thermal conductivity statistical distribution of composite material. Such a distribution shows the probability for certain value of the effective thermal conductivity can be obtained in a separate test.

For convenience of comparing the results of various series of tests, we use the relative effective thermal conductivity, defined as the ratio of the effective thermal conductivity of the material to the thermal conductivity of the matrix

$$\kappa_e = \frac{\lambda_e}{\lambda_m}, \tag{97}$$

as well as the probability density, equal to the ratio of the frequency of the value κ_e falling in a certain interval to the width of this interval.

Statistical distributions of the relative effective thermal conductivity for various placement parameters are shown in Figures 12 – 17.

Figures 12 – 13 are performed on the same scale and show the transformation of the distribution of effective thermal conductivity with a change in the concentration of inclusions. Analysis of the figures shows that a change in the concentration of inclusions causes not only a shift in the position of the mode of the distribution, but also a change in the width of the peak, and the nature of its asymmetry, namely, the elongation of the front or tail of the distribution. Peak of the distribution is narrower at small and large concentrations of filler than at average concentrations. The case of a small concentration of inclusions corresponds to an elongated front of the distribution, and the case of large concentrations corresponds to an elongated tail of the distribution.

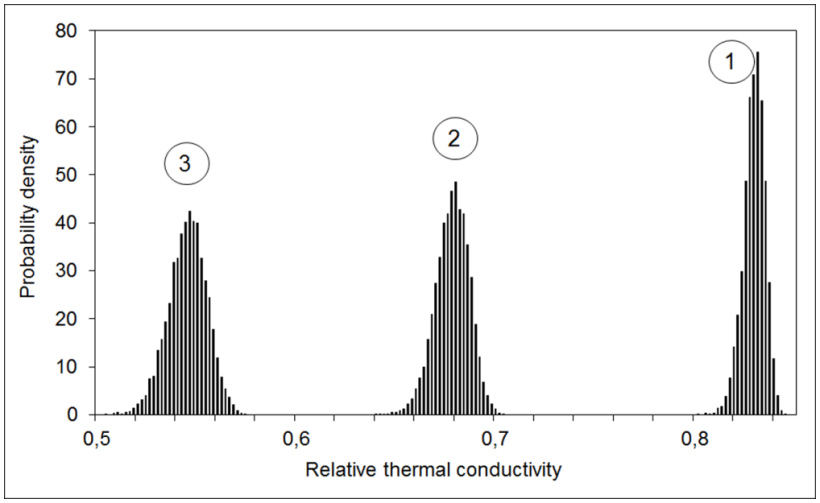

Figure 12. Statistical distributions of the relative effective thermal conductivity in series of 8000 tests: $a = 128h$, $b = 8h$, $d = 0$, and 1) $c = 0.098$; 2) $c = 0.195$; 3) $c = 0.293$.

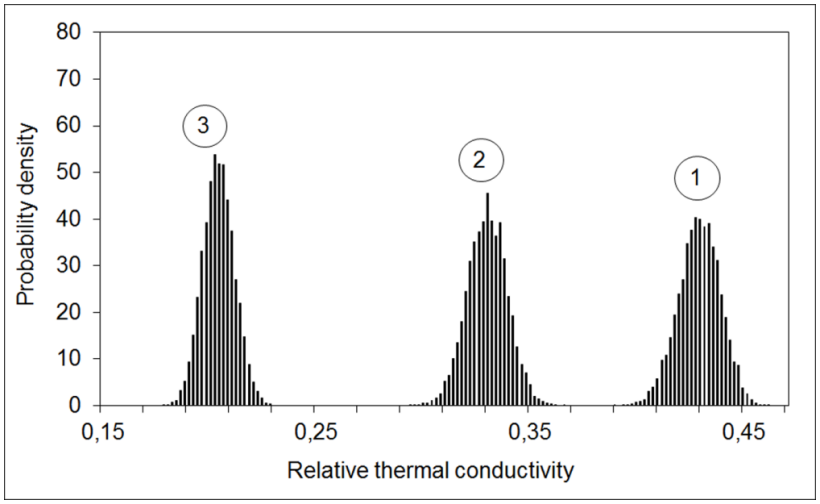

Figure 13. Statistical distributions of the relative effective thermal conductivity in series of 8000 tests: $a = 128h$, $b = 8h$, $d = 0$, and 1) $c = 0.391$; 2) $c = 0.488$; 3) $c = 0.637$.

An increase in the size of the filler particles with an equal concentration of inclusions and a constant minimum distance between them leads to a shift in the average value of κ_e toward lower values (Figures 14, 15). The width of the distribution peak under these conditions increases. These changes become more significant at higher filler concentrations.

Figure 16 presents a change in the character of the distribution of κ_e with a change in the minimum distance between the filler particles for the case of constant concentration and size of the inclusions. An increase in the minimum distance causes a small increase in the effective thermal conductivity, while the peak width of the distribution decreases.

The statistical distributions κ_e for a different scatter of the particle sizes of the filler are shown in Figure 17. In these tests, the Gaussian distribution of the particle size of the filler was simulated with a given average value $< b >$ and different values of the root-mean-square deviation σ_b.

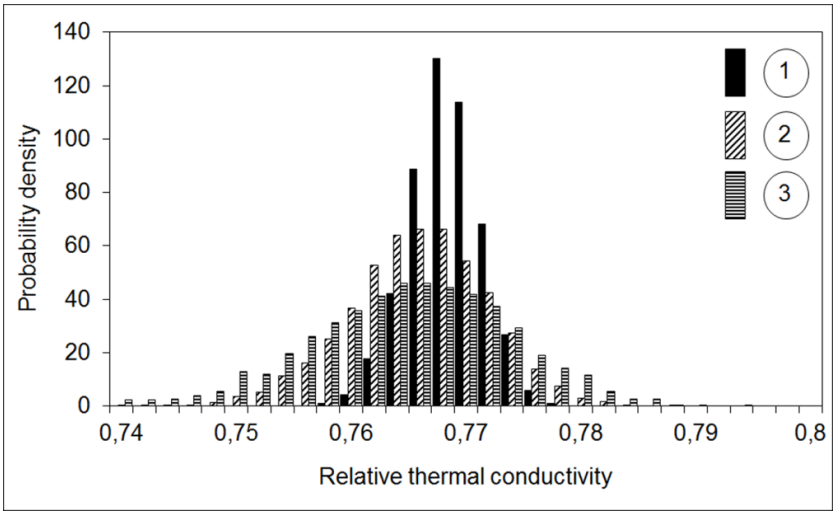

Figure 14. Statistical distributions of the relative effective thermal conductivity in series of 4000 tests: $a = 128h$, $c = 0.14$, $d = 4h$, and 1) $b = 8h$; 2) $b = 12h$; 3) $b = 16h$.

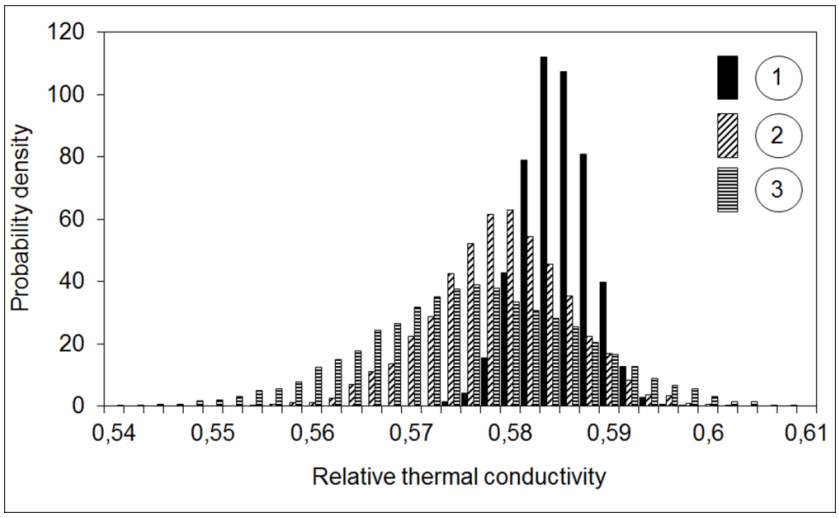

Figure 15. Statistical distributions of the relative effective thermal conductivity in series of 4000 tests: $a = 128h$, $c = 0.28$, $d = 4h$, and 1) $b = 8h$; 2) $b = 12h$; 3) $b = 16h$.

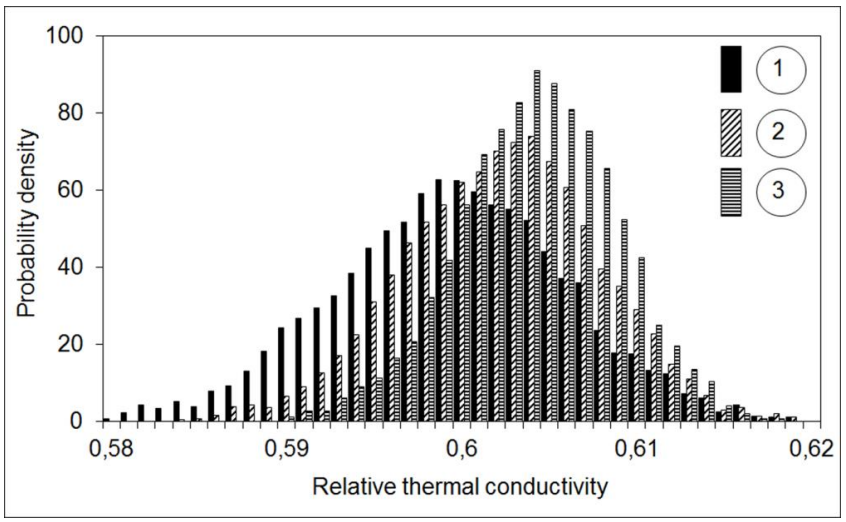

Figure 16. Statistical distributions of the relative effective thermal conductivity in series of 4000 tests: $a = 128h$, $c = 0.26$, $b = 12h$, and 1) $d = 4h$; 2) $d = 6h$; 3) $d = 8h$.

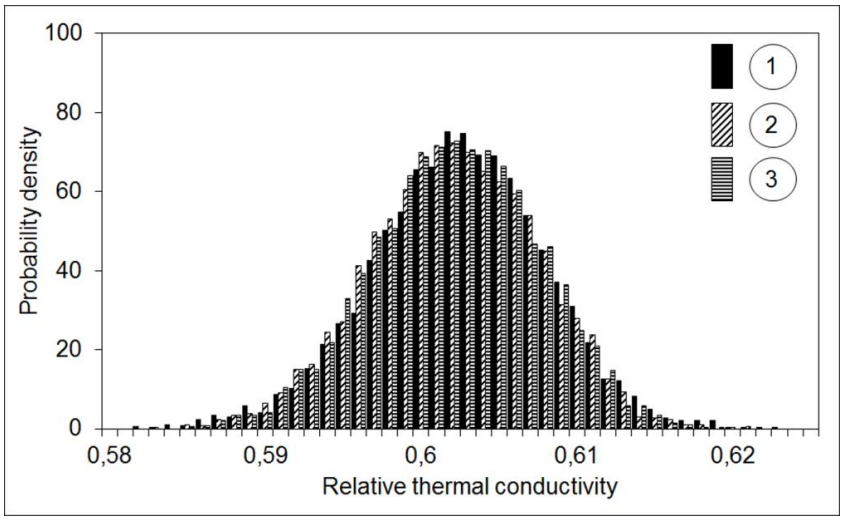

Figure 17. Statistical distributions of the relative effective thermal conductivity in series of 4000 tests: $a = 128h$, $c = 0.26$, $d = 6h$, $< b > = 12h$ and 1) $\sigma_b = 0$; 2) $\sigma_b = 0.6h$; 3) $\sigma_b = 2.1h$.

The form of the distribution of κ_e practically does not change for different scatterings of the dimensions of the filler particles. It should be noted that for larger filler particles the mean value of κ_e decreases, while for smaller particles it increases (Figure 15). The case of particle size distribution according to the Gaussian law corresponds to the appearance in the matrix in equal quantities of both smaller and larger inclusions compared with the average size. Thus, we obtain two competing effects of particles of large and small sizes on an average value of κ_e. Figure 17 shows, that in this case both effects compensate each other.

The possible values of κ_e are limited from above and below, so it is natural to assume that the statistics κ_e can be described by the beta-distribution with a probability density

$$p(x) = \frac{x^{\alpha-1}(1-x)^{\beta-1}}{\int_0^1 x^{\alpha-1}(1-x)^{\beta-1}dx}. \tag{98}$$

However, using the beta-distribution is inconvenient for analyzing the results of numerical experiments, since the variations of parameters α and β affects both the position of the distribution mode and its asymmetry.

It seems more convenient for us to use the Weibull distribution

$$p_w(x) = \frac{\gamma_W}{\delta_W}\left(\frac{x-\alpha_W}{\beta_W}\right)^{\gamma_W-1}\exp\left[\left(-\frac{x-\alpha_W}{\beta_W}\right)^{\gamma_W}\right]. \tag{99}$$

Parameter β_W shows the distribution mode position, parameter α_W characterizes distribution width, and shape parameter γ_W characterizes the asymmetry of the distribution. To approximate the experimental data, it makes sense to introduce scale factors in the Weibull distribution (41), which depend on the width of the interval partition. A fairly convenient modification of the Weibull distribution is [Seasolve PeakFit Users Manual 4.12]:

$$p(x)=a_0^{(W)}\left(\frac{a_3^{(W)}-1}{a_3^{(W)}}\right)^{-\frac{a_3^{(W)}-1}{a_3^{(W)}}}\left(\frac{x-a_1^{(W)}}{a_2^{W}}+\left(\frac{a_3^{(W)}-1}{a_3^{(W)}}\right)^{\frac{1}{a_3^{(W)}}}\right)^{a_3^{(W)}-1}\times$$
$$\times\exp\left[-\left(\frac{x-a_1^{(W)}}{a_2^{(W)}}+\left(\frac{a_3^{(W)}-1}{a_3^{(W)}}\right)^{\frac{1}{a_3^{(W)}}}\right)^{a_3^{(W)}}+\frac{a_3^{(W)}-1}{a_3^{(W)}}\right], \quad (100)$$

where $a_0^{(W)}$ is the magnitude of the peak amplitude, $a_1^{(W)}$ is the position of the distribution mode, $a_2^{(W)}$ is the full-width at half-maximum (FWHM), and $a_3^{(W)}$ is the shape parameter of the distribution, characterizing its asymmetry at half-maximum width.

Table 1. Parameters of the effective thermal conductivity distribution at various placements of inclusions in composite

Location settings	$a_0^{(W)}$	$a_1^{(W)}$	$a_2^{(W)}$	$a_3^{(W)}$
b = 8h, d = 4h and c = 0.141 (Figure 14)	128	0.769	0.0112	3.81
b = 12h, d = 4h and c = 0.141 (Figure 14)	67.3	0.797	0.0241	4.34
b = 16h, d = 4h and c = 0.141 (Figure 14)	46.3	0.766	0.0361	4.48
b = 8h, d = 4h and c = 0.281 (Figure 15)	114	0.585	0.0120	3.57
b = 12h, d = 4h and c = 0.281 (Figure 15)	60.2	0.580	0.0252	4.09
b = 16h, d = 4h and c = 0.281 (Figure 15)	37.1	0.576	0.0351	4.32
b = *12*h, d = 4h and c = 0.264 (Figure 16)	60.1	0.600	0.0259	4.16
b = 12h, d = 6h and c = 0.264 (Figure 16)	71.2	0.603	0.0212	4.02
b = 12h, d = 8h and c = 0.264 (Figure 16)	88.1	0.605	0.0162	3.79
b = 12h, σ_b = 0,6h d = 4h, c = 0.264 (Figure 17)	72.2	0.602	0.0190	3.58
b = 12h, σ_b = 1,6h, d = 4h, c = 0.264	75.4	0.601	0.0185	3.66
b = 12h, σ_b = 2,1h, d = 4h, c = 0.264 (Figure 17)	73.3	0.602	0.0189	3.62

Table 1 shows the parameters of the distributions from Figures 14 – 17, obtained by approximating them with a modified Weibull distribution (100). For the distributions shown in Figure 12 and 13 it is more convenient to use the graphical representation in the form of concentration dependences (Figure 18). Note that parameter $a_1^{(W)}$ is close to the average value, i.e., to the effective thermal conductivity κ_e, which is discussed in detail below.

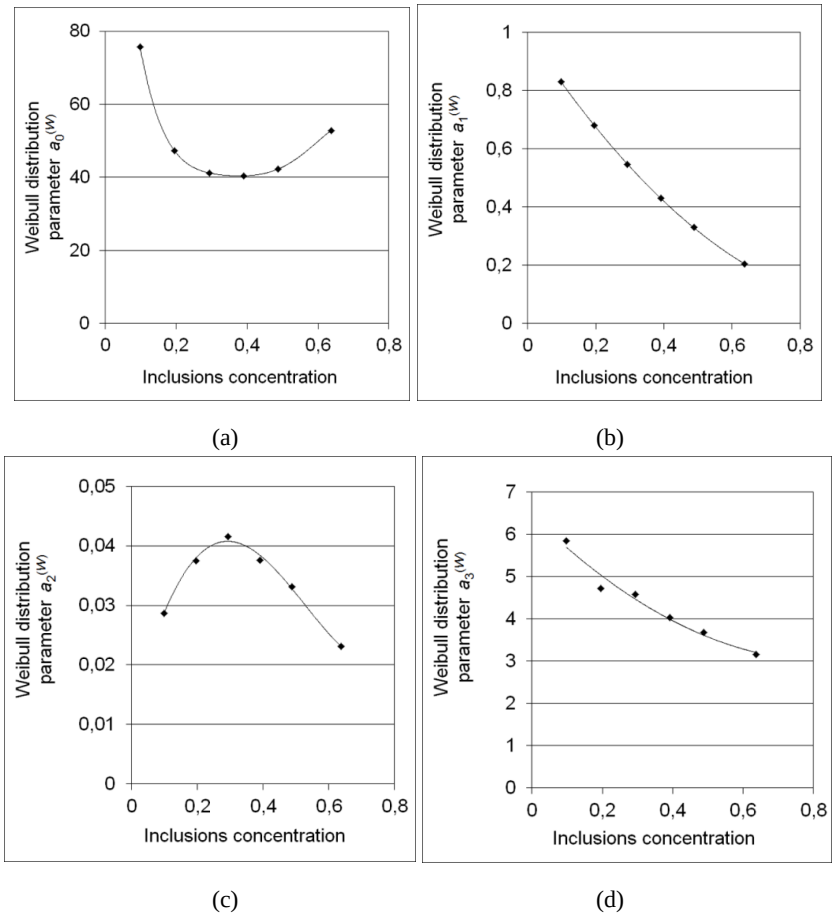

Figure 18. Concentration dependences of the Weibull distribution parameters shown in Figures 12 and 13 ($a = 128h$, $b = 8h$, $d = 0$): a) $a_0^{(W)}$; b) $a_1^{(W)}$; c) $a_2^{(W)}$ d) $a_3^{(W)}$.

The distribution parameters given in Table 1 and shown in Figure 18, allow us to objectively estimate the changes in the distribution parameters of the effective thermal conductivity when the parameters of the placement of the filler particles are changed. The effect of the placement parameters of the inclusions on the peak width of the effective thermal conductivity distribution will be discussed in more detail below.

Let's summarize the results of this study:

- increase in the size of the inclusions causes a decrease in the effective thermal conductivity, provided that all other placement parameters remain unchanged;
- increase in the minimum distance between inclusions causes a decrease in the effective thermal conductivity, provided that all other placement parameters remain unchanged;
- increase in the concentration of inclusions leads to a change in the asymmetry of the peak of the distribution from the case when peak is elongated in the front direction to the case when the peak is elongated in the tail direction;
- increase in the size of the inclusions leads to a change in the asymmetry of the peak of the distribution, namely, the peak is elongated in the front direction;
- the distribution peak is elongated in the tail direction in the case of increasing of minimum distance between the inclusions;
- dispersion of the filler particle sizes does not significantly affect the characteristics of the peak of the distribution.

This indicates that the resistance to heat transfer in the composite is determined not only by the ratio of the volumes of phases with different thermal conductivity, but also by the qualitative change in the processes of heat transfer when the parameters for placing heat-insulating inclusions change.

5.2. CONCENTRATION DEPENDENCES OF THERMAL CONDUCTIVITY

The relative effective thermal conductivity of the material was calculated as the average value $< \kappa_e >$ for a series of tests. Graphs of $< \kappa_e >$ dependence on the concentration c for various b and d, for a series of 800 tests, are shown in Figures 19 and 20.

It should be noted that the generalized conductivity theory (GCT) [39, 40] predicts $< \kappa_e >$ dependence only on the concentration of inclusions and their shape providing that the inclusions are not interacting.

Analysis of local fluxes maps indicates that in the case of square-shaped inclusions the ratio $d/b \geq 1$ can be considered as a criterion for the absence of interaction between the filler particles and, consequently, as a criterion of the GCT applicability.

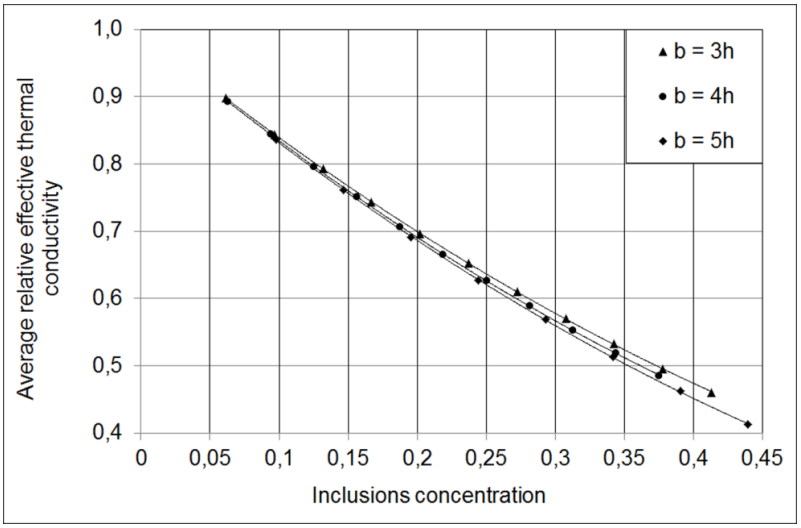

Figure 19. Dependence $<\kappa_e>(c)$ for materials with different b and $d = h$.

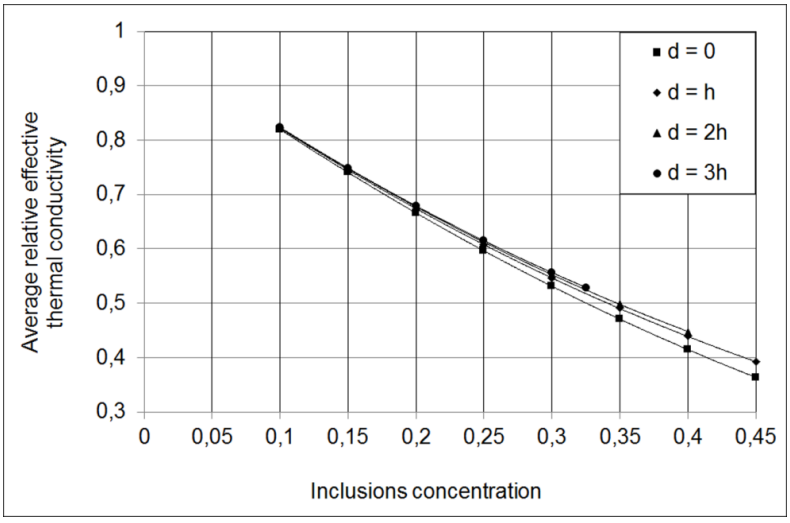

Figure 20. Dependence $<\kappa_e>(c)$ for materials with $b = 8h$ and various d.

Indeed, as d approaches b, the $<\kappa_e>(c)$ dependences differ slightly: the difference in values $<\kappa_e>$ is less than 0.5% (Figure 20). In this case, the effects of inclusions on local heat fluxes near their neighbors are weakening. Parameters d and b, in accordance with the predictions of GCT, no longer affect the effective thermal conductivity.

When the inclusion concentration in composite materials increases the application of GCT becomes problematic, but in case of small concentrations (with $c \leq 0.1$), $<\kappa_e>$ behavior is well described by this theory. With a small number of inclusions, it is most probable that they will be located at distances significantly greater than d. Thus, in this case GCT can be applied, and $<\kappa_e>$ should not depend on b and d. Figures 19 and 20 show weak dependences $<\kappa_e>(d)$ and $<\kappa_e>(b)$ in the region of small concentrations.

The dependencies shown in Figures 19 and 20 are nonlinear. We considered in sections 2 various models of thermal conductivity of composites, which also predict various nonlinear dependencies $<\kappa_e>(c)$. Since our approach is model-free, we did not use any of the models described above and selected a function that best describes the results of

our numerical experiments. In doing so, we have limited the range of possible dependencies rather simple fractional-rational and irrational functions. As a result, we found that the concentration dependences of the effective thermal conductivity are best described by the function [315]

$$< \kappa_e >= 1 - \frac{\alpha_\kappa c}{\sqrt{(1+\beta_\kappa c)^3}}, \tag{101}$$

where c is inclusions concentration; α_κ and β_κ are fitting coefficients.

Discussion of Figures 15 and 16 showed that the mode of distribution of effective thermal conductivity depends on the placement parameters of inclusions, so it is natural to expect the functional dependence of α_κ and β_κ on b and d.

Our numerical experiments showed that if we impose computational grids with different steps h on the modeled pattern with inclusions, then, as expected, the effective thermal conductivity obtained as a result of solving the heat conduction problem does not change. That is, if we have calculated the thermal conductivity of the template with the placement parameters a = 128, b = 16 and d = 4, then exactly the same result will be obtained for the mesh, with the superimposition of a = 160, b = 20 and d = 5 or a = 224, b = 28 and d = 7. Thus, α_κ and β_κ should depend on dimensionless quantities: the relative size of the inclusion b/a, and the relative minimum distance d/a. The relative minimum distance can also be defined as d/b, and this definition seems more convenient to us.

The analysis of fitting coefficients showed that α_κ weakly depends on the relative minimum distance between the inclusions d/b, but demonstrates a significant dependence on the relative size of the inclusions b/a. The graph of this functional dependence is shown in Figure 21. The graph shows points with different values of d/b.

It should be noted that dependence $\alpha_\kappa = \alpha_\kappa (b/a)$ is saturated at $b/a > 1$, i.e., in the case where the size of inclusions cannot be assumed to be small compared to the size of the counting area. Apparently, under such

conditions, the concept of a composite material and its effective thermal conductivity lose meaning, and the countable region can be interpreted as a model of a construction of two homogeneous materials.

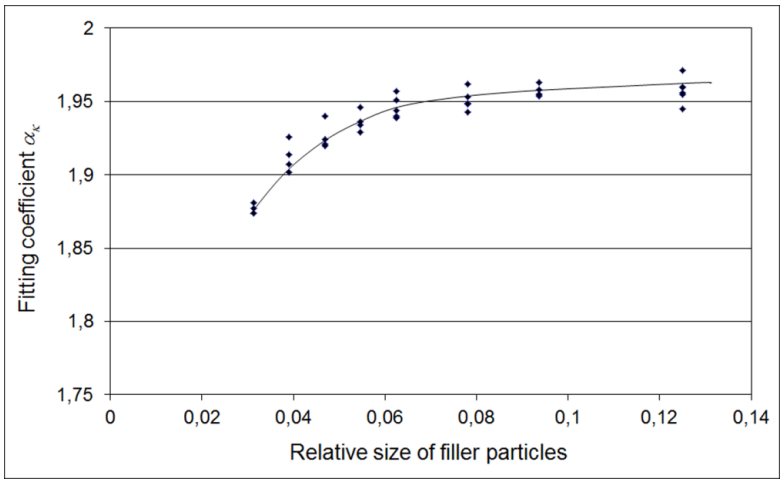

Figure 21. Dependence of the fitting coefficient α_κ on the relative size b/a of filler particle.

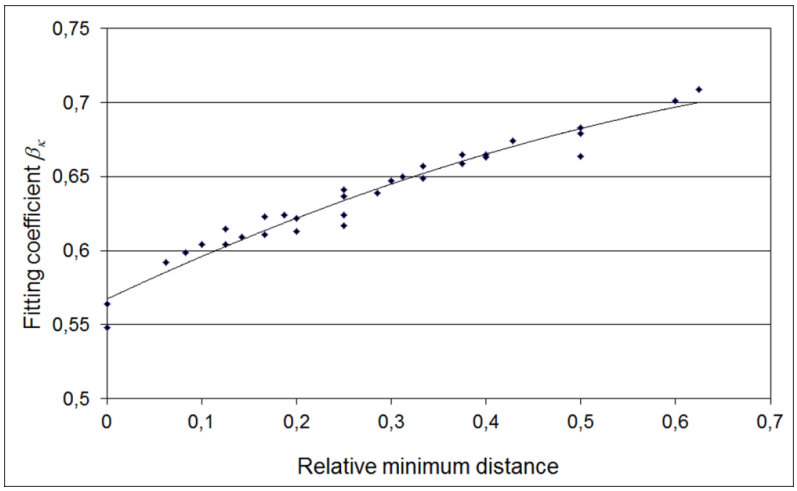

Figure 22. Dependence of the fitting coefficient β_κ on the relative minimum distance d/b between the filler particles.

The fitting coefficient β_κ, on the contrary, turned out to be practically independent of b/a, but depending on the relative minimum distance d/b. Figure 22 shows the dependence of the fitting coefficient β_κ on the relative minimum distance between the filler particles. In this case, points with different values of b/a, are marked on the graph.

The separation of the fitting factors by a coefficient α_κ that depends only on the relative particle size, and by the coefficient β_κ, that depends only on the relative minimum distance is a good argument for choosing the relative minimum distance precisely in the form of d/b.

Another argument is that in this case it is possible to analyze not the dependencies $< \kappa_e > (b/a)$ and $< \kappa_e > (d/a)$ separately, but immediately consider the dependencies $< \kappa_e > (d/b)$. Figure 23 shows the dependencies of $< \kappa_e > (d/b)$ for several material models with different filler particle sizes and their similar concentrations.

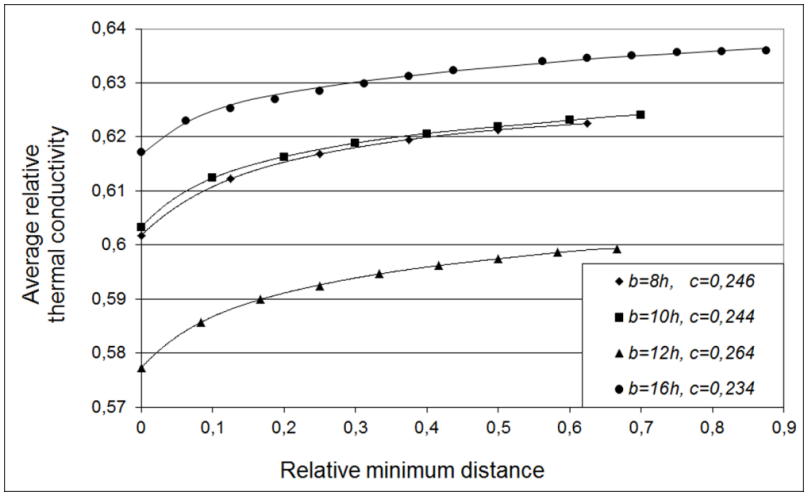

Figure 23. Dependence $< \kappa_e > (d/b)$ for materials: $b = 8h$ and $c = 0.246$; $b = 10h$ and $c = 0.244$; $b = 12h$ and $c = 0.264$; $b = 16h$ and $c = 0.234$.

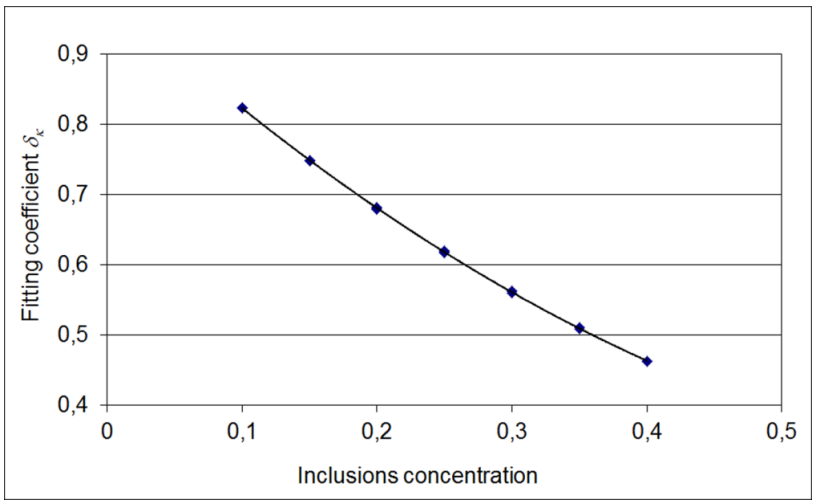

Figure 24. Dependence of the fitting coefficient δ_κ on the relative concentration of the filler particles.

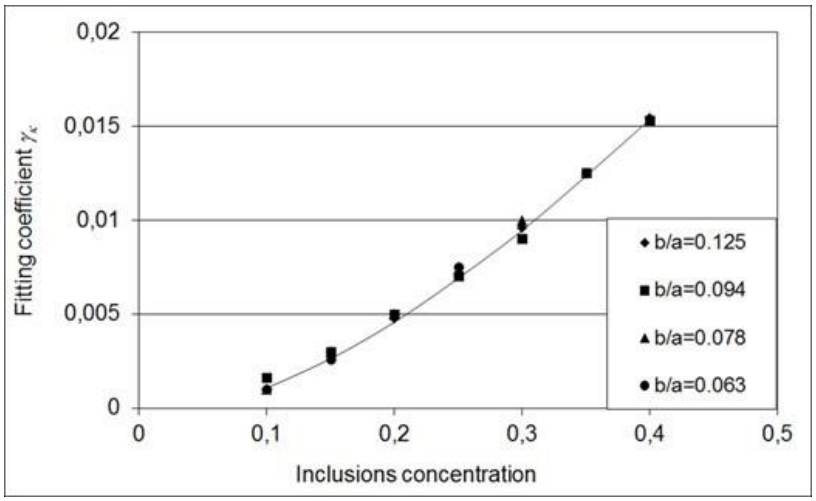

Figure 25. Dependence of the fitting coefficient γκ on the relative concentration of the filler particles.

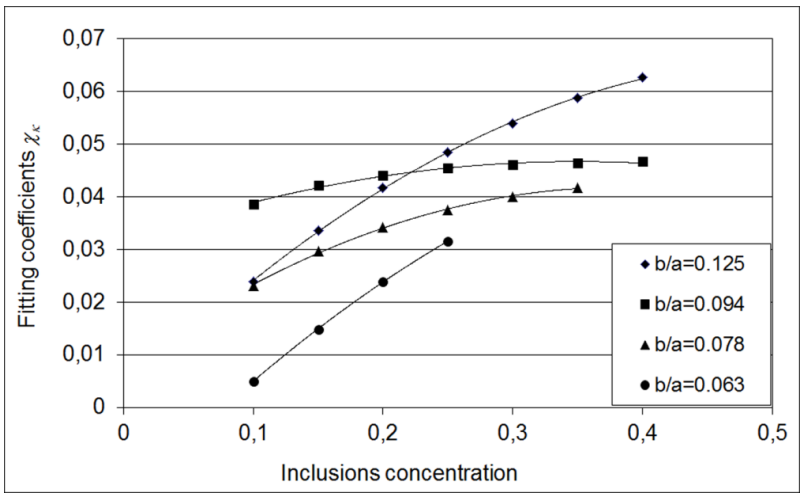

Figure 26. Dependence of the fitting coefficient χ_κ on the relative concentration of the filler particles.

As noted above, the increase in the ratio d/b corresponds to a decrease in the interaction between the inclusions. The dependence of $< \kappa_e > (d/b)$ under these conditions disappears. Indeed, the curves in Figure 23 are saturated when the value of d/b tends to unity.

Under the condition $d/b < 1$, the dependencies $< \kappa_e > (d/b)$ are approximated fairly well by the expression

$$\kappa_e = \delta_\kappa + \gamma_\kappa \ln\left(\frac{d}{b} + \chi_\kappa\right), \tag{102}$$

where δ_κ, γ_κ, and χ_κ are the fitting coefficients which depend on the concentration of filler particles in the material.

Figure 24 shows the dependence of the fitting coefficient $\delta_\kappa(c)$ on the relative concentration of the filler particles. The graph presents the points for 8 different sizes of inclusions. The values of the coefficient δ_κ for the used variants b/a (from 0.031 to 0.125) coincide with high accuracy. Consequently, this dependence is common for all sizes of inclusions.

Figure 25 shows similar concentration dependence for the fitting coefficient γ_κ. This coefficient is also weakly dependent on the size of inclusions. And only the concentration dependencies of the fitting coefficient χ_κ turned out to be different for inclusions of different sizes (Figure 26).

5.3. Effective Anisotropy and Scatter of Thermal Conductivity

The dispersion can be used as a characteristic of the distribution curve broadening, but for analysis of heat transfer in a two-phase composite, it is more convenient to consider the standard deviation or the coefficient of variation. The dependence of the standard deviation s_κ of $<\kappa_e>$ distributions on the inclusions concentration is shown in Figures 27 and 28. Here the values of the placement parameters coincide with those shown in Figures 19 and 20.

Standard deviation increases with inclusions concentration raises and reaches maximum at a certain value of c (Figures 27 and 28). The position of the maximum $s_\kappa(c)$ is determined mainly by minimum distance d and slightly depends on inclusions size b. The presence of the maximum $s_\kappa(c)$ is quite expectable. At high concentrations, we can consider the material model not in the form of a heat-conducting matrix with heat-insulating inclusions (model A), but in the form of a heat-insulating matrix with heat-conducting inclusions (model B). The heat-insulating inclusions concentration increasing (model A) is equivalent to the heat-conducting inclusions concentration decreasing (model B).

The standard deviation s_κ tends to zero for $c = 1$ (model A) or $c = 0$ (model B). Thus, $s_\kappa(c)$ dependence should have a maximum. However, this dependency cannot be symmetrical with respect to the position of the maximum. Model A assumes square-shaped inclusions and model B assumes fiber-shaped inclusions. Maximum $s_\kappa(c)$ is shifted toward smaller concentrations of insulating inclusions.

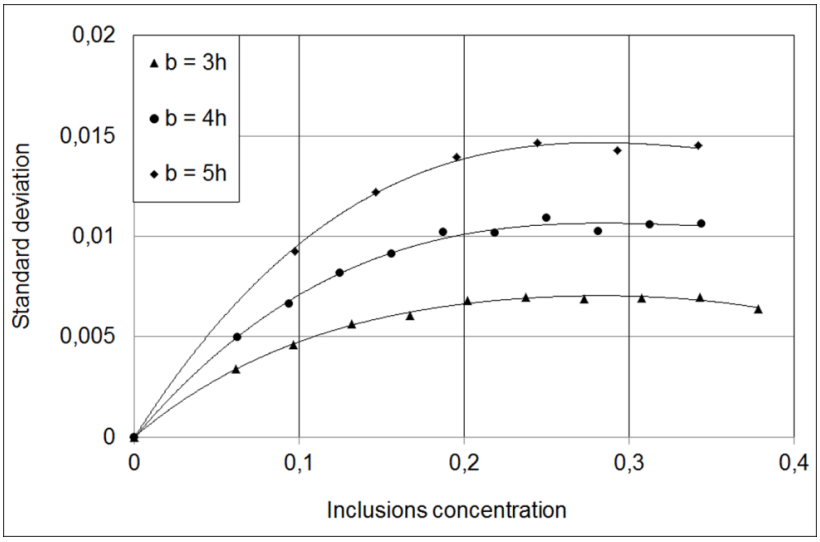

Figure 27. Dependence of the distribution standard deviation $<\kappa_e>$ on the concentration for materials with different b and $d = h$.

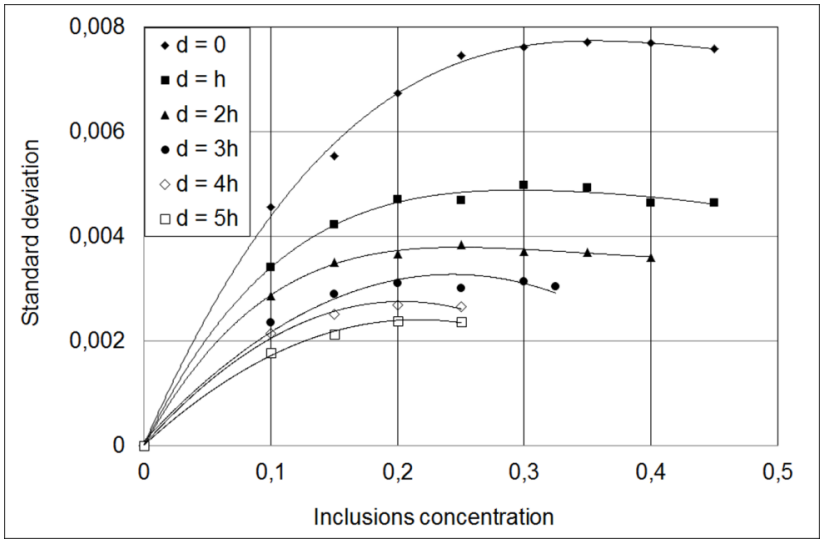

Figure 28. Dependence of the distribution standard deviation $< \kappa_e >$ on the concentration for materials with $b = 8h$ and different d.

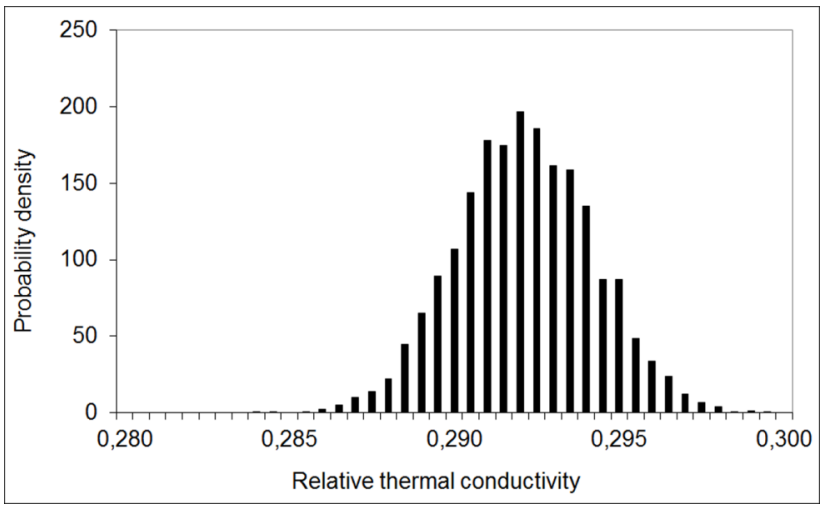

Figure 29. Distribution of the $<\kappa_e>$ values when a temperature macro-gradient is applied along x-axis.

The inclusions random placement in the template not only leads to difference in the effective thermal conductivity from test to test, but also to difference in the effective thermal conductivity when temperature macro-gradient is applied along different directions in the same test. It is known that anisotropy is a characteristic for ordered materials. We examine a difference in the effective thermal conductivity along different directions in composite. This difference was called an effective anisotropy.

The probability distribution of $<\kappa_e>$ values in a series of 3600 tests for placement $N = 272$ heat-insulating inclusions is shown in Figure 29. The sizes of the inclusions and the template are $b = 5h$ and $a = 128h$, respectively, and the minimum distance between inclusions is $d = h$. The distribution of thermal conductivity values in the same test series, but after turning each template by 90° is presented in Figure 30. This rotation corresponds to the fact that the temperature macro-gradient is first applied along x-axis and then applied along y-axis.

Both distributions are visually very similar and have similar parameters; the average value of $<\kappa_e>$ in both cases is 0.292. The standard deviations of both distributions are 0.0205 and 0.0207, respectively. The

distribution of the difference between the relative effective thermal conductivities $\delta\kappa_e$ along two coordinate axes x and y is shown in Figure 31. This difference we call the effective anisotropy of thermal conductivity.

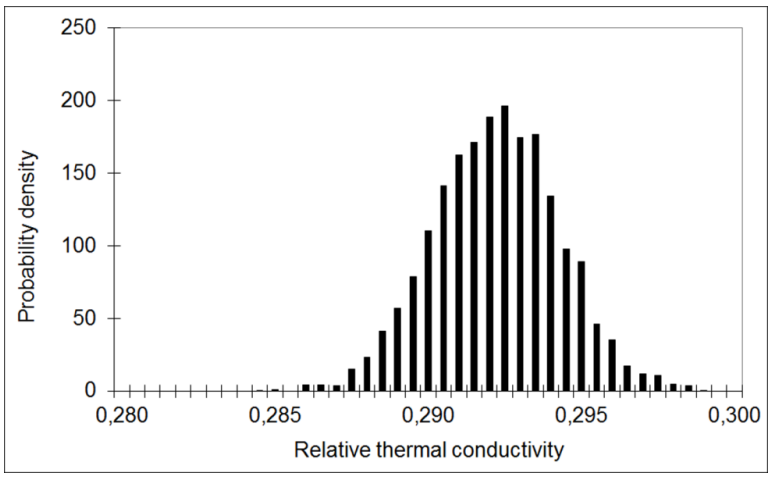

Figure 30. Distribution of the $<\kappa_e>$ values when a temperature macro-gradient is applied along y-axis.

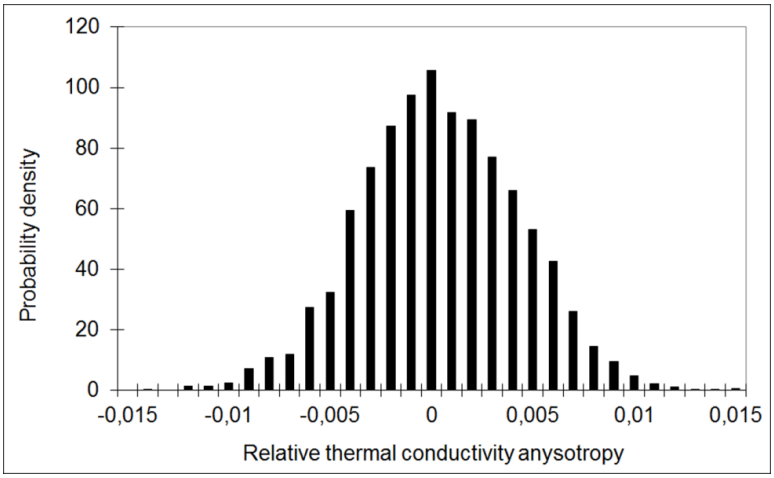

Figure 31. Distribution of the $\delta\kappa_e$ values.

The average value $<\delta\kappa_e>$ for the distribution, which is shown in Figure 31, is 8.88×10^{-5}. This value is 3.5 orders of magnitude smaller than the average values of the initial distributions of effective thermal conductivity. We can assume that, in comparison with the average value of the effective thermal conductivity, the value $<\delta\kappa_e>$ is equal to 0.

The standard deviation of the distribution $\delta\kappa_e$ is 0.0392, which is almost 2 times higher than the standard deviation of the initial distributions κ_e. Hence, we can assume that for a given series of placements the initial distributions κ_e for different temperature macro-gradient directions are statistically independent from each other. In other words, the change in the temperature macro-gradient direction is equivalent to another random realization of inclusions placement.

Therefore, there is no sense to consider the average value $< \delta\kappa_e >$ as a quantitative measure of the effective anisotropy of thermal conductivity, since the mathematical expectation of this quantity should be equal to 0.

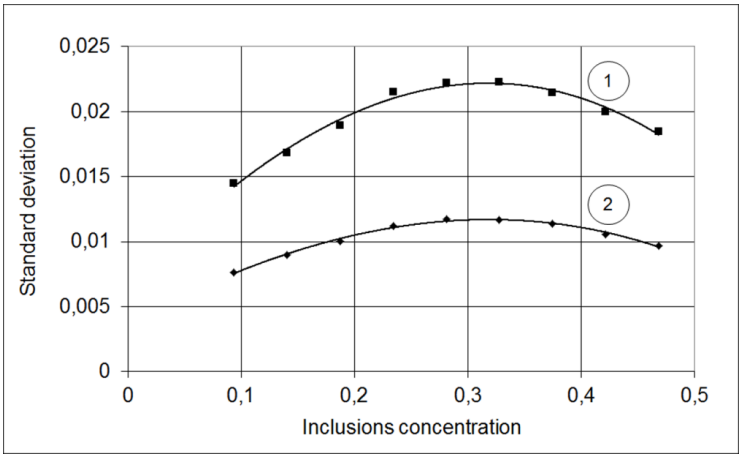

Figure 32. Dependences of the standard deviation on the inclusions concentration for the distribution $\delta\kappa_e$ (curve 1) and the distribution κ_e (curve 2).

We propose to consider the standard deviation s_δ of $\delta\kappa_e$ distribution as a measure of effective anisotropy, since the mathematical expectation of

this value is different from zero. The value of s_δ was found to depend on the inclusions placement parameters of in the computational domain.

The dependence of s_δ on the inclusions concentration with size $b = 16h$ in the template $a = 128h$ is presented in Figure 32. The minimum distance between inclusions equals $d = 3h$. This dependence was obtained from a series of 400 tests. Figure 32 shows, in addition, the standard deviation s_κ of the effective thermal conductivity distribution in the same series of tests. The ratio of values s_δ and s_κ is equal approximately to 1.9. Both standard deviations have maximum in the concentration range $c \approx 0.32$.

The appearance of this maximum is quite understandable. The inclusions concentration growth leads to the fact that the parameters of heat fluxes in different directions are increasingly differs from each other. When the inclusions concentration is high they are located in the matrix evenly and, basically, at the minimum distance. The conditions for the flow of heat fluxes become practically the same in different directions, which leads to a drop in the standard deviation of the distribution $\delta\kappa_e$.

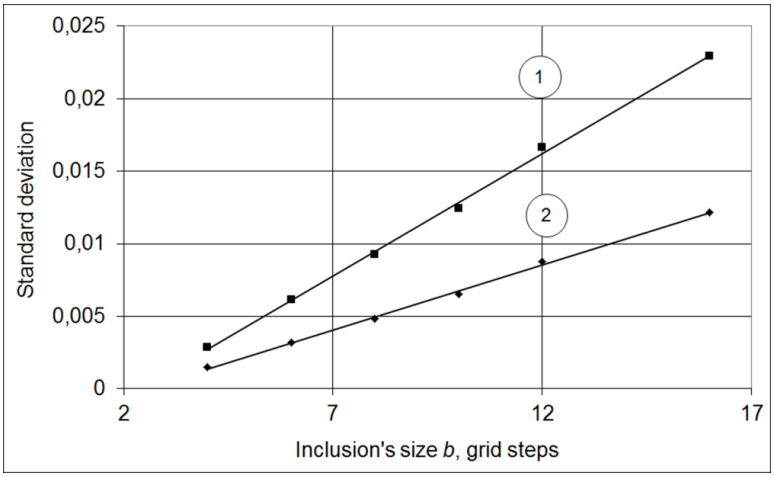

Figure 33. Dependences of the standard deviation on the inclusions size for the distribution $\delta\kappa_e$ (curve 1) and the distribution κ_e (curve 2).

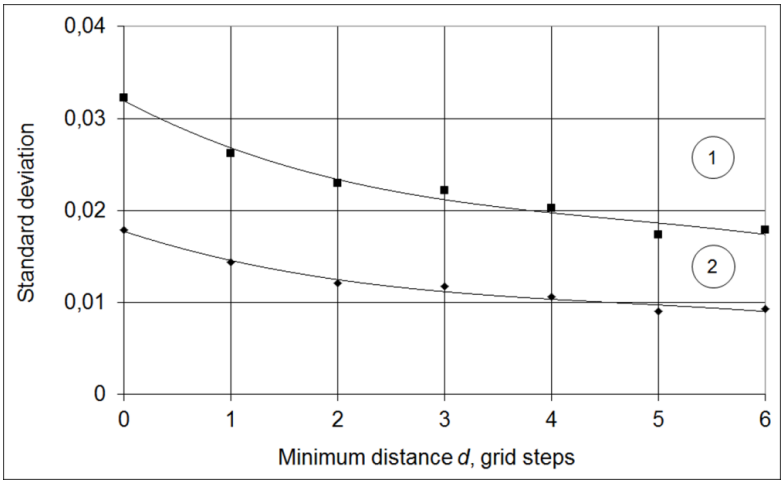

Figure 34. Dependences of the standard deviation on the minimum distance between inclusions for the distribution $\delta\kappa_e$ (curve 1) and the distribution κ_e (curve 2).

Figure 33 presents the dependences of s_δ and s_κ on the size of inclusions in the template $a = 128h$. The inclusions concentration in the matrix is $c \approx 0.29$ and the minimum distance between inclusions is $d = 3h$. Each point of the graph is obtained from a series of 400 tests.

Figure 34 presents the dependences of s_δ and s_κ on the minimum distance between inclusions in the template $a = 128h$ for the inclusions concentration in the matrix $c \approx 0.29$ and the size of the inclusions $b = 16h$. Each point of the graph is obtained from a series of 400 tests. Dependences of s_δ and s_κ for different parameters are similar.

Thus, the value of s_δ is actually determined by the value of s_κ. Hence, the standard deviation s_κ of the distribution κ_e (but not the deviation of the distribution $\delta\kappa_e$) can be considered as a measure of the thermal conductivity effective anisotropy.

5.4. SUMMARY

1) Composite materials with a random inclusions arrangement have statistical scattering of the effective thermal conductivity depending on the specific implementation.
2) The statistical distribution of the effective thermal conductivity can be approximated by the Weibull distribution.
3) A composite material with certain inclusions placement parameters can be characterized by effective thermal conductivity. We have shown that the average value of thermal conductivity in a representative sample of its realizations can be considered as an effective thermal conductivity.
4) The correct value of effective thermal conductivity requires consideration of the mutual influence of inclusions. The effective thermal conductivity of a composite depends on the size of the inclusions and the minimum distance between them.
5) An approximate expression for the dependence of the effective thermal conductivity of the composite on the concentration of inclusions is proposed. This expression includes two coefficients, one of which depends only on the relative size of the inclusions, and the other coefficient depends only on the relatively minimal distance between the filler particles. Such a form of approximation is convenient for further theoretical analysis.
6) The approximate expression for the dependence of the effective thermal conductivity of the composite on the concentration of inclusions is applicable for the entire range of possible inclusions concentrations, in contrast to those offered in GCT family models, which can only be used at low inclusions concentrations.
7) Two-phase composite materials with a random inclusions arrangement have different values of the effective thermal conductivity for different directions of the heat fluxes. This property of the composite material can be called thermal conductivity effective anisotropy. The thermal conductivity effective anisotropy has statistical nature.

8) The constancy of the ratio between the standard deviations of the effective anisotropy of thermal conductivity and the actual effective thermal conductivity in all numerical experiments (approximately 1.9) indicates a high degree of statistical independence of the heat fluxes in the material when a temperature macro-gradient is superimposed in two mutually perpendicular directions.
9) The change in the direction of the temperature macro-gradient must be associated with a change in the inclusions distribution.
10) The standard deviation of distribution of composite material effective thermal conductivity can be considered as measure of its thermal conductivity effective anisotropy.

Chapter 6

STATISTICS OF LOCAL HEAT FLUXES INTENSITY DISTRIBUTION

6.1. SET OF DISTRIBUTION MODES

As we noted above (see sections 4), the presence of filler particles in the composite matrix leads to a violation of the homogeneity of the heat fluxes. Analysis of intensity maps of local fluxes revealed a number of specific areas of the matrix: an unperturbed matrix, a dark matrix, and induced heat conductive channels. These regions differ in the characteristic value of local heat fluxes: the intensity of local fluxes in a dark matrix is lower than the intensity of local fluxes in the unperturbed matrix. The induced heat-conducting channels were characterized by an increased intensity of local fluxes.

It is obvious that the value of the effective thermal conductivity of a composite material is determined by the conditions for the flow of local heat fluxes. The above is the reason for studying the distribution of local heat fluxes in terms of intensity. It is also necessary to clarify the peculiarities of the influence of the placement of inclusions on the distribution of local heat fluxes.

Figures 35 shows sample of composite material with randomly disposed thermal insulating inclusions. Template size is $128h \times 128\ h$, the

inclusions size is $b = 5h$ and minimum distance is $d = h$. Thermal insulating inclusions are represented on the grid by dark gray squares. Inclusions concentration is $c \approx 0.293$ ($N = 192$).

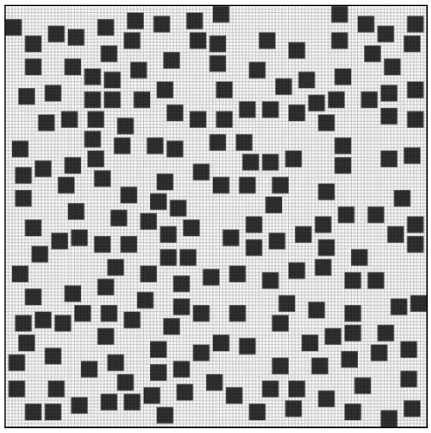

Figure 35. Composite with placement parameters: $a = 128h$, $b = 5h$, and $d = h$ (sample 1).

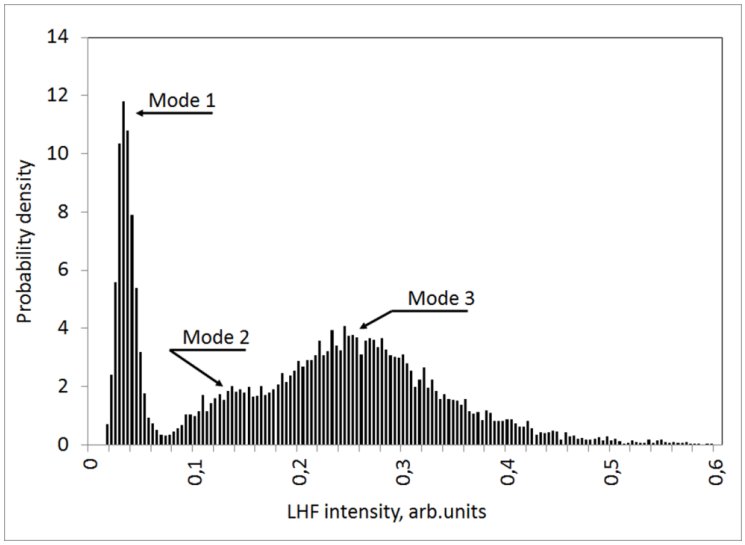

Figure 36. LHF intensity distribution in sample 1.

Figure 36 presents the LHF intensity distribution in this sample. This distribution is characterized by three modes, designated as mode 1, mode 2, and mode 3. Mode 1 is well differentiated from mode 2, and modes 2 and 3 partially overlap.

To identify the template cells through which flow the local fluxes of different modes of this distribution, we used the following visualization. All cells with the intensity of local flows less than 0.07 conventional units were painted black. Local heat fluxes forming mode 1 flow through these cells. Most local fluxes with an intensity of 0.07 to 0.17 conventional units form mode 2. Cells with such fluxes were painted in grey. The cells through which local flows passed with an intensity of more than 0.17 conventional units were painted white. Such local fluxes preferentially form the mode 3. In connection with the partial overlap of modes 2 and 3, such a visualization will show some part of the cells forming mode 2 as the cells forming mode 3 and vice versa. However, the share of such erroneous identification will be low.

The result of the visualization is shown in Figure 37. A preliminary analysis of the obtained map indicates that the mode 1 is formed by local fluxes passing through the inclusions, with the exception of the corner cells. Therefore, we call this mode as the mode of inclusion (I-mode). The cells forming mode 2 turned out to be, in fact, cells of a dark matrix (compare Figures 5, 8, 10, and 11). Subsequently mode 2 will be called a dark matrix mode (D-mode). Dark matrices of inclusions are interacting for the case of a given concentration $c \approx 0.293$.

The remaining white cells may belong to either the unperturbed matrix or the induced heat-conducting channels. Since white cells begin to predominate at a given concentration of inclusions, we will call this mode a mode of channels (C-mode).

Figure 38 shows the distribution of the intensity of local heat fluxes in another sample from the same series of tests. The separation of mode D and mode C is not so obvious on this histogram, as in Figure 36.

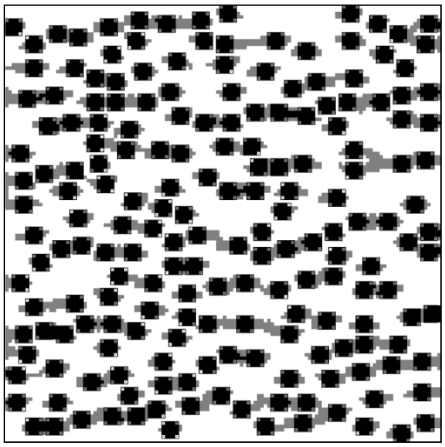

Figure 37. LHF intensity map in sample 1.

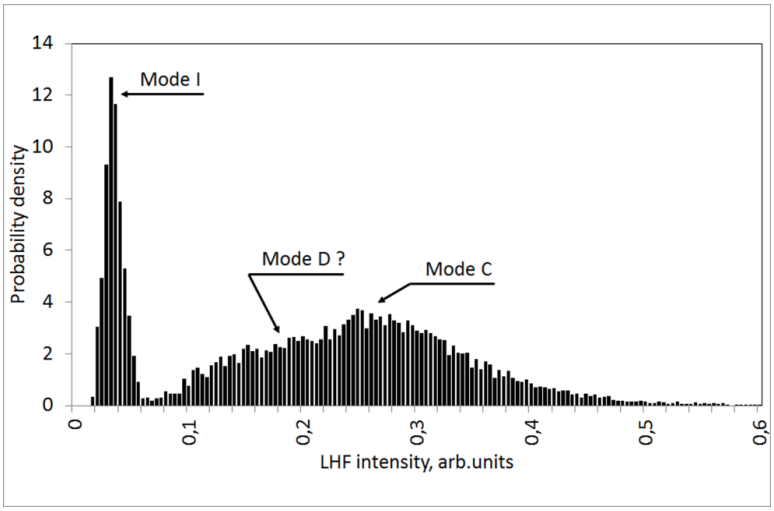

Figure 38. LHF intensity distribution in sample 2.

To analyse the effect of placement parameters on individual distribution modes, we built histograms for large series of tests. Figure 39 shows the LHF intensity distribution in a series of 800 tests (series 1) for placement parameters $a = 128h$, $b = 5h$, $d = h$, $c \approx 0.293$ ($N = 192$, samples 1 and 2 are included in this series). In this case the total number of analyzed LHF is more than 10^7.

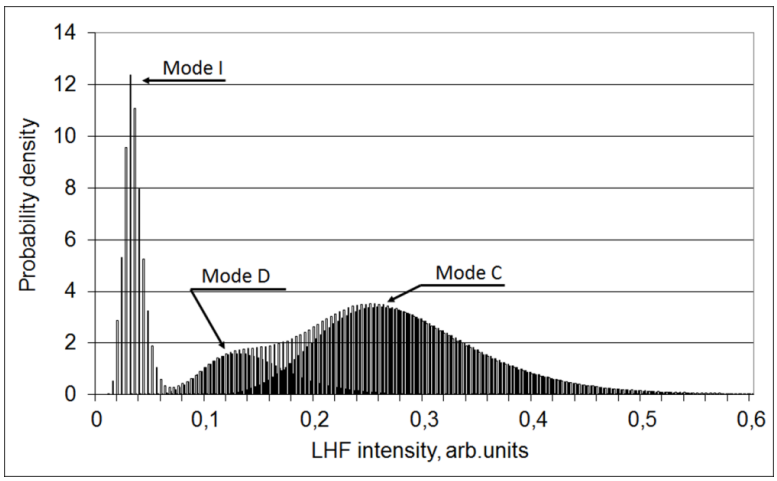

Figure 39. LHF intensity distribution for test series 1: $a = 128h$, $b = 5h$, $d = h$, $c \approx 0.293$ and its decomposition into separate modes D and C.

We assumed that the presented multimodal distribution is the sum of three single-mode distributions. Representative statistics allows determining the parameters of overlapping modes if the types of their distributions are known. First it should be marked that C-mode is asymmetric with an elongated right tail. We can assume that D-mode has a similar asymmetry in spite of it is not so obvious.

As random variation of the LHF value through each next cell in connection with multiplicative influence of randomly distributed inclusions should have an equal probability regardless of the sign, then, the probability of the LHF intensity distribution should be described by a log-normal law if number of steps and inclusions concentration are large:

$$y(x) = \frac{1}{\sqrt{2\pi}\sigma} \cdot \frac{1}{x} \cdot \exp\left[-\frac{1}{2}\left(\frac{\ln x - \ln Me}{\sigma} \right)^2 \right], \qquad (103)$$

where *Me* is a median, σ is the distribution parameter, which is related to the width of the mode. However, the reparametrized form of the lognormal

distribution, which is used, in particular, in [PeakFit™ v4 Users Guide], seems to be more convenient for further analysis.

$$y(x) = A\exp\left[-\frac{1}{2}\left(\frac{\ln x - \ln Mo}{\sigma}\right)^2\right], \tag{104}$$

where *A*, and *Mo* are mode and amplitude of the mode, respectively. Their values are easily determined from the histogram.

The result of decomposition of the discussed multimodal distribution into separate components using the PeakFit® v. 4.12 program is also shown in Figure 39.

I-mode, being well separated from other modes, does not need a special decomposition procedure. In this case, the program was used to determine the parameters of this mode.

A part of LHF which corresponds to a certain mode, we call power of the mode *Pw*. The power can be defined as the area under the intensity distribution curve. For the test series under discussion the power of I-Mode, D-mode and C-mode are $Pw_I \approx 24.7\%$, $Pw_D \approx 15.3\%$, and $Pw_C \approx 59.9\%$, respectively. It is appropriate to note here that the concentration of inclusions in this case is 29.3%. The power of the mode of inclusions turns out to be somewhat smaller because the inclusion angles do not participate in its formation. Indeed, there are 192 inclusions in the template at given placement parameters, therefore, 768 grid nodes are excluded from the formation of the I-mode. The expected power of I-mode should be $Pw_I = (4800 - 768)/16384 \times 100\% \approx 24.6\%$, which agrees with the above results of the analysis of the distribution.

The intensity of the fluxes passing through the angles of inclusions is characteristic for the dark matrix. Therefore, the angular nodes contribute to the determined power Pw_D. Correction of this power by 768 grid nodes shows that the "clean" power of the dark matrix in this case is $Pw_D \approx 10.6\%$.

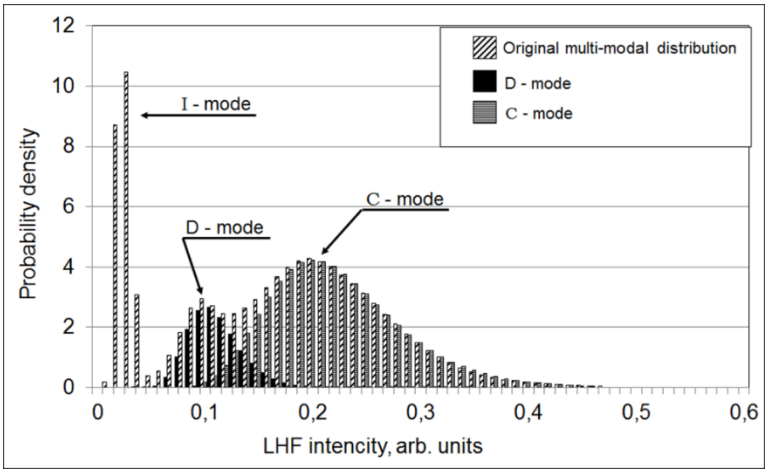

Figure 40. LHF intensity multi-modal distribution for test series 2: a = 160h, b = 4h, d = h, c = 0.30 and its decomposition into separate modes D and C.

The characteristics of the individual modes of distribution and the degree of their overlap are very sensitive to the placement parameters of the inclusions, as shown in the following three figures.

Figure 40 shows LHF intensity distribution in a template with following parameters of randomly arranged inclusions: a = 160h, b = 4h, d = h, c = 0.30 (N = 480). Distribution represents series of 400 tests (series 2). The overlapping modes was separated, and they are also shown in Figure 40. For this test series the power of C-mode and D-mode are $Pw_C \approx 61.2\%$ and $Pw_D \approx 15.8\%$ respectively.

Figure 41 shows a distribution of the LHF intensity values in a template with the following parameters: a = 160h, b = 5h, d = h, c = 0.293 (N = 300) for a series of 400 tests (series 3). It can be seen, the overlapping of modes D and C is stronger than in series 2. The power of the modes also changes: $Pw_C \approx 59.9\%$, and $Pw_D \approx 14.2\%$. The increase in the inclusions size leads to larger overlap of the modes.

It should be noted that series 1 and series 3 differ only in the size of the template a, and therefore in the relative size of the inclusions b/a. Comparing the LHF distributions of these series (Figures 39 and 41), we note the following. C-mode in both cases has the same power, but in series

3, the mode position is shifted to the left with respect to the mode position in series 1. The shift to the left is also observed for the D-mode, although to a lesser extent than for the C-mode.

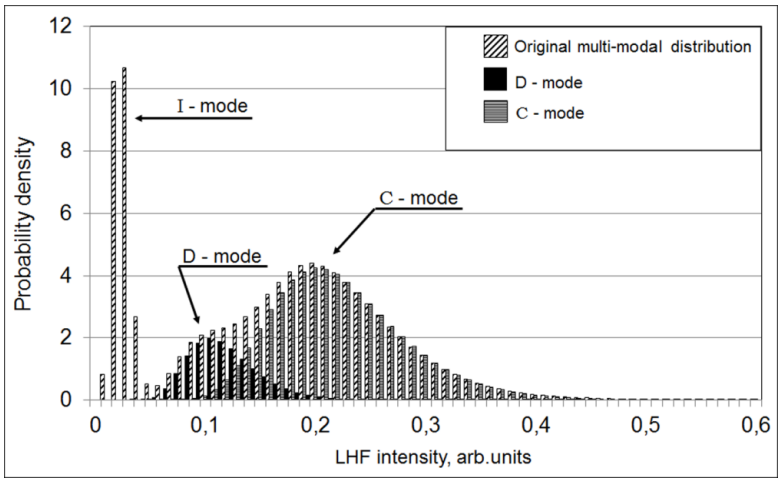

Figure 41. LHF intensity multi-modal distribution for test series 3: a = 160h, b = 5h, d = h, c = 0.293 and its decomposition into separate modes D and C.

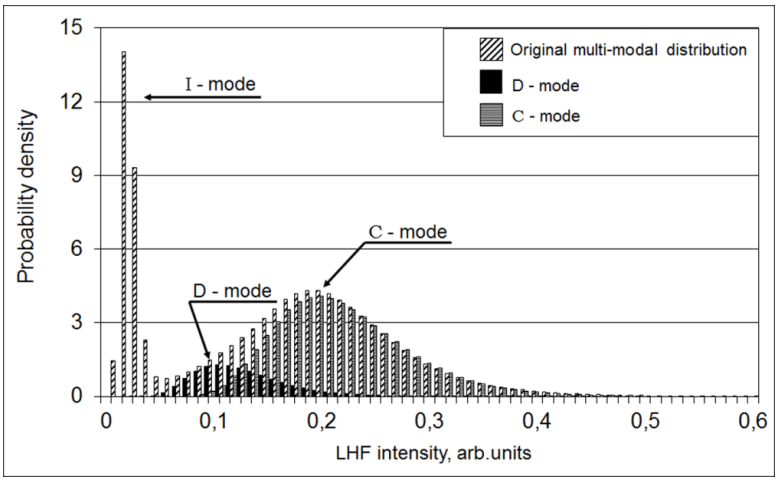

Figure 42. LHF intensity distribution in test series 4: a = 160h, b = 8h, d = h, c = 0.292 and its decomposition into separate modes D and C.

Figure 42 shows the distribution of the LHF intensity values in the template $a = 160h$, $b = 8h$, $d = h$, $c = 0.293$ ($N = 300$) for a series of 400 tests (series 4). In this case, visually, nothing indicates the presence of two overlapping modes in the distribution, and only knowledge of the transformation of the distribution with increasing b allows us to assume the presence of two hidden modes at the observed wide maximum. In this case $Pw_C \approx 59.2\%$, and $Pw_D \approx 12.2\%$.

The presence of numerical data characterizing the overlap of the D- and C-modes makes it possible to clarify the localization of LHF in the samples.

It was found for series 4 that almost all the fluxes falling into intensity range from 0.05 to 0.1 arbitrary units correspond only to the D-mode, and all the fluxes with intensity more than 0.21 arbitrary units belong to the C-mode. On the heat fluxes pattern the inclusions are marked black, the areas with LHF intensity of at least 0.22 arbitrary units (belong to the C-mode) are marked white, and the areas with LHF intensity up to 0.1 arbitrary units (belong to the D-mode) are marked dark gray. The regions which can belong to both D-modes and C-mode because of their overlap are marked light gray. An example of such a pattern is shown in Figure 43.

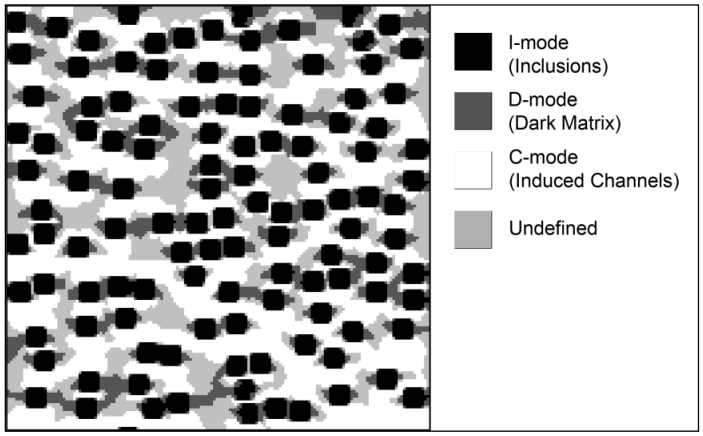

Figure 43. LHF modes intensity map for test series 4.

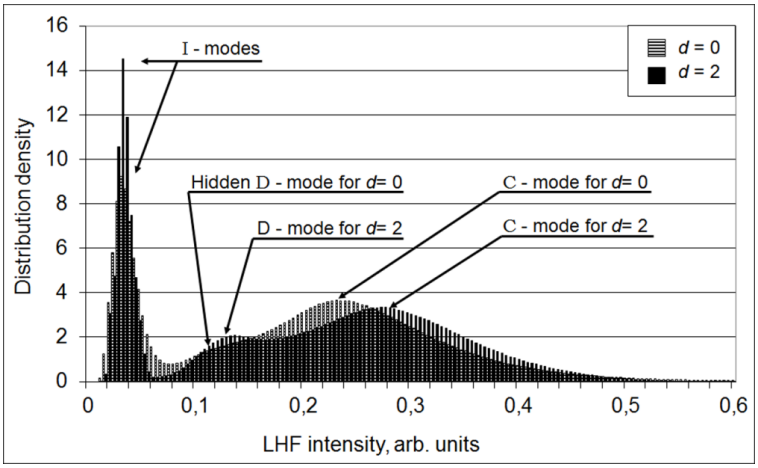

Figure 44. LHF intensity distributions in test series 4 and 5.

The proposed method of visualizing the localization of different LHF modes gives a better idea of the structure of the heat transfer paths (induced heat-conducting channels) inside the sample than the method used by us in constructing the visualization in Figure 33.

The distribution modes are also sensitive to the minimum distance between inclusions. Figure 44 shows the distribution of the LHF intensity values in the template $a = 160h$, $b = 5h$, $c = 0.293$ ($N = 192$) for $d = 0$ and $d = 2h$ (series 5 and 5 respectively). Increasing of minimum distance d from 0 to $2h$ leads to shifting both of C and D modes to the right. Wherein, the power of the C-mode decreases from 62.1% to 54.5%. The decrease in Pw_C is accompanied by an increase in the power of the D-mode from 12.1% to 21.0%.

Returning to Figure 43, we note that inclusions placement shown there does not satisfy the criterion $d/b \geq 1$ for the applicability of GCT. Inclusion placements of this type just lead to the appearance of induced heat-conducting channels.

In the case of low inclusions concentrations and large minimum distances between them, the criterion for the applicability of GCT will be fulfilled. In this case, the nature of LHF flow turns out to be somewhat different. The changing of LHF flow character should lead to a change in

the character of LHF intensity distribution. Really, at low heat-insulating phase concentrations the shape of the LHF distribution varies significantly, although the multimode character of the distribution is preserved. Figures 45 and 46 show the LHF intensity distribution in test series 6 with parameters: $a = 128h$, $b = 5h$, $c = 0.073$ ($N = 48$), $d = h$ and in test series 7 with parameters: $a = 128h$, $b = 16h$, $c = 0{,}094$ ($N = 6$), $d = 6h$, respectively.

Analysis of C-mode shape at low concentration of inclusions shows that in this case its distribution cannot be approximated by a lognormal law. It is natural to assume that with a decrease in inclusions concentration, the number of random changes in LHF while passing the total heat flux through the material becomes not large enough that conditions for the formation of a lognormal distribution arise.

The second feature of LHF intensity distributions at low concentrations and large inclusions is shown in Figure 46. D-mode amplitude is reduced so that it is impossible to discern.

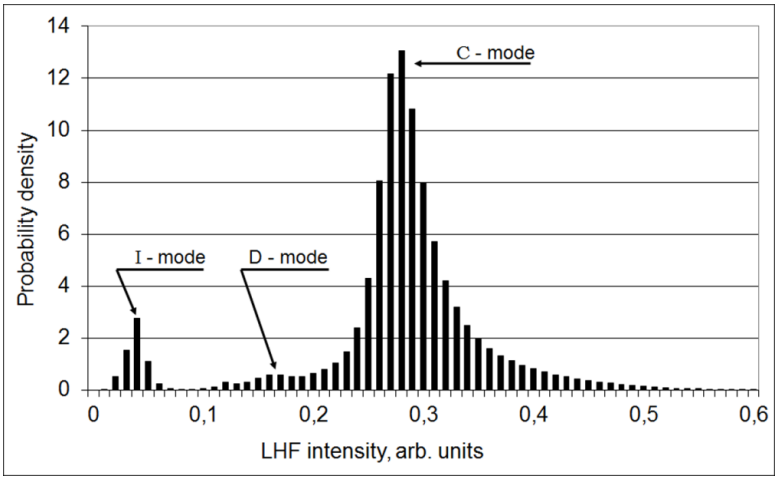

Figure 45. Poly-modal LHF intensity distribution in test series: $a = 128h$, $b = 5h$, $c = 0.073$, and $d = h$.

The third feature of the LHF intensity distributions at small inclusions concentrations is well manifested at relative minimum distances of the order of 0.5. Figure 47 shows the LHF intensity distribution in test series 6

with parameters: $a = 128h$, $b = 6h$, $c = 0.196$ ($N = 89$), $d = 3h$. Two separate modes, indicated in the figure as D1 and D2, arise at the location of the mode D.

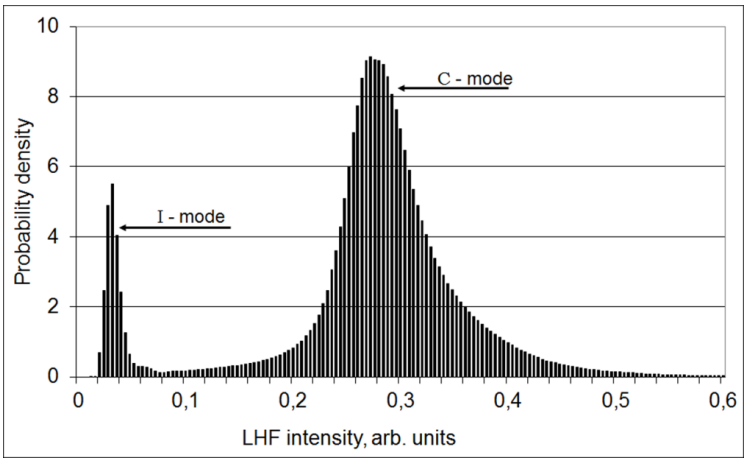

Figure 46. Poly-modal LHF intensity distribution in test series $a = 128h$, $b = 16h$, $c = 0.094$, and $d = 6h$.

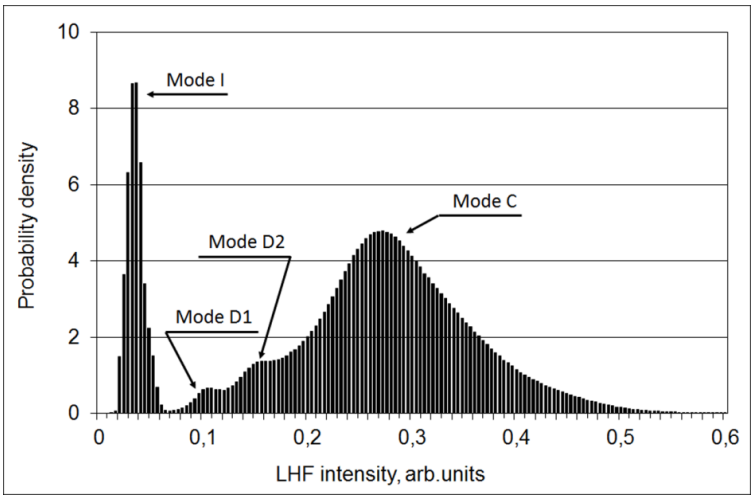

Figure 47. Poly-modal LHF intensity distribution in test series $a = 128h$, $b = 6h$, $c = 0.196$, and $d = 3h$.

To clarify the nature of the D1 and D2 modes, we constructed a series of visualizations of the LHF intensity distribution in specific tests. We applied the same method as in the construction of Figure 33 by selecting the template cells that form the D1 mode with a dark gray colour, and D2 with a light gray colour. Inclusions are traditionally marked in black, and the regions of the unperturbed matrix are white. Induced channels are not formed at a given inclusions concentration, hence, the mode C is correctly interpreted as a weakly perturbed matrix. The result of the visualization is shown in Figure 48. This figure shows the LHF map in the sample fragment (placement parameters: $a = 128h$, $b = 5h$, $c = 0.098$ and $d = 3h$).

Figure 48 shows that both dark gravy areas (mode D1) and light gray (mode D2) are localized in a dark matrix. The mode D1 is that part of the dark matrix that is near the centre of the inclusion face or between closely spaced inclusions.

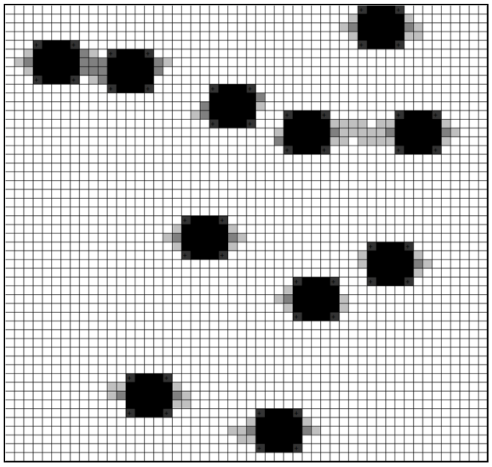

Figure 48. LHF intensity map in the sample fragment.

Thus, the modes D1 and D2 arise as a result of the splitting of the mode D under certain placement parameters.

6.2. EFFECT OF INCLUSIONS PLACEMENT ON HEAT FLUXES DISTRIBUTION MODES

We considered the dependences of the statistical characteristics of the LHF intensity distribution modes on the inclusions placement parameters only for inclusions concentrations of the order of 0.25 or more. Such concentrations correspond to the region where the GCT applicability conditions are violated and where it can be expected that the character of the LHF distribution will affect the value of the effective thermal conductivity of the material.

Figure 49 shows the power dependencies of the C and D modes obtained for the test series with parameters $a = 128h$, $b = 5h$, $d = 0$, and $a = 128h$, $b = 5h$, $d = h$. Each point on the graph is obtained as a result of processing a separate series of 800 tests. The splitting of D-mode was not observed at these placement parameters and in the indicated concentration range. Naturally, the power of the dark matrix mode increases with increasing the concentration of inclusions, and the power of the mode of the induced heat-conducting channels decreases.

It should be noted that for the parameters $d = 0$ and $c > 0.4$, the region that corresponds to the mode of the dark matrix is larger than the region that corresponds to the mode of the induced channels. However, even at $d = h$ and above, the region corresponding to the mode of induced channels is always larger than the region corresponding to the mode of the dark matrix. At non-zero minimum distances between inclusions, it is usually impossible to achieve concentrations above 0.5. Such an opportunity is only for $d = 0$. It turned out that for the concentration $c \sim 0.6$ the $Pw\ (c)$ dependences are saturated and, with a further increase in concentration, change their behaviour: Pw_C begins to increase unexpectedly, and Pw_D begins to decrease. According to our assumption, this is due to the fact that at such concentrations the material should be considered not as a heat-conducting matrix with square body-insulating inclusions, but as a heat-insulating matrix with heat-conducting filamentous inclusions. LHF transport in such material requires a separate study.

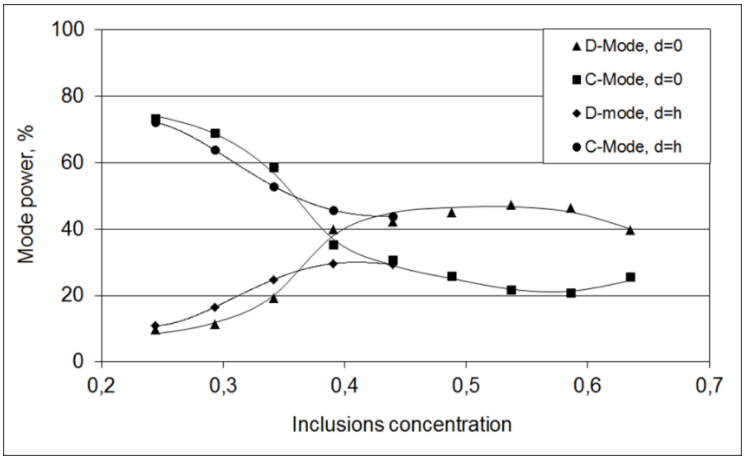

Figure 49. Dependences of Pw_C and Pw_D on the inclusions concentration in tests: $a = 128h$, $b = 5h$, $d = 0$ and $a = 128h$, $b = 5h$, $d = h$.

The position of the C and D modes (the *Mo* parameter from formula (104)) with increasing concentration weakly shifts to the left (i.e., the intensity of LHF decreases), and as the minimum distance increases, they shift to the right (i.e., the LHF intensity increases).The dependences of the *Mo* parameter for modes C and D on the inclusions concentration in the same series of tests are shown in Figure 50.

The increase in the size of the inclusions allows us to investigate the behavior of the position of the mode at a greater number of minimum distances. Figure 51 shows the dependence of Mo_C on the concentration of inclusions for parameters $a = 128h$, $b = 6h$ $d = h$, $2h$, and $3h$. The character of the Mo_C (c) dependence varies with increasing d. In this material, the mode D splits into the modes D1 and D2, which exhibit the same behavior as in Figure 50.

The mode width parameter σ (see formula (104)) for modes C and D has somewhat different behaviour. Figure 52 shows that D-mode width σ_D relatively quickly increases with increasing concentration of inclusions in the case when C-mode width σ_C is weakly dependent on the concentration of inclusions. Since the position of the mode is slightly shifted to the left, the increase in the width of the mode occurs due to the stretching of the

right tail. This means that intense local heat fluxes can pass through the regions of a dark matrix filled with a sufficiently large number of inclusions.

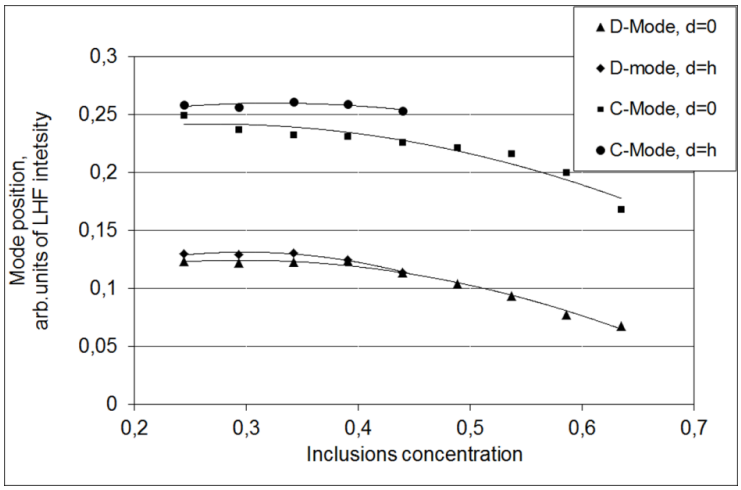

Figure 50. Dependences of Mo_C, and Mo_D on the inclusions concentration in tests: $a = 128h$, $b = 5h$, $d = 0$ and $a = 128h$, $b = 5h$, $d = h$.

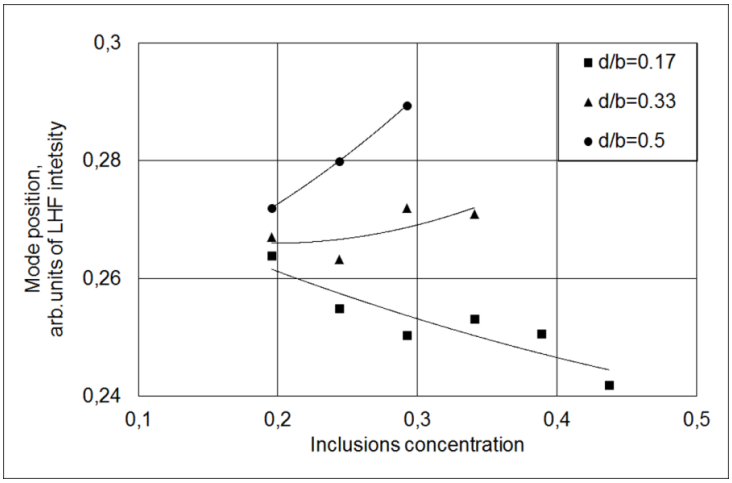

Figure 51. Dependences of Mo_C, and Mo_D on the inclusions concentration in tests: $a = 128h$, $b = 6h$ and various d/b.

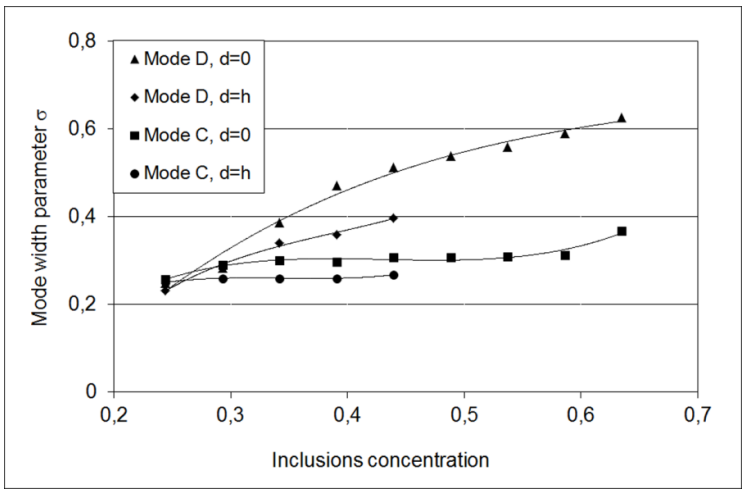

Figure 52. Dependences of σ_C, and σ_D on the inclusions concentration in tests: $a = 128h$, $b = 5h$, $d = 0$ and $a = 128h$, $b = 5h$, $d = h$.

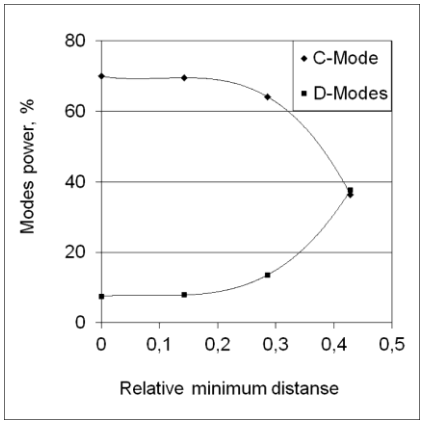

Figure 53 a. Dependences of the power of C-mode and the total power of the modes D1 and D2 on the d/b ratio in tests: $a = 128h$, $b = 7h$, $c = 0.245$, $d = 0, h, 2h, 3h$.

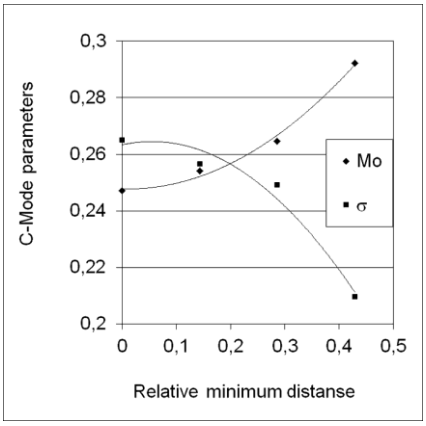

Figure 53b. Dependences of parameters Mo and σ of C-mode on the d/b ratio in tests: $a = 128h$, $b = 7h$, $c = 0.245$, $d = 0, h, 2h, 3h$.

As we showed above (see sections 5), the effective thermal conductivity of a composite material is affected by the ratio d/b. The most probable cause of this effect is the change in the conditions for the flow of

local heat fluxes. Therefore, the dependences of the mode characteristics of the LHF distribution on the ratio d/b are of interest.

Figure 53 shows the dependence of the mode power of the induced channels and the total power of the dark matrix modes D1 and D2 on the relative minimum distance for the test series $a = 128h$, $b = 7h$, $c = 0.245$, $d = 0, h, 2h, 3h$.

Analysis of the graph shows that when the minimum distance increases, the regions between the inclusions are occupied mainly by a dark matrix. Visualization of solutions shows that this occurs mainly in the direction of the x axis, i.e., in the direction of the common heat flux. The thermal conductive channels become narrower, but the intensity of the fluxes in them increases. This is confirmed by Figure 54, which shows the dependence of the position of the mode of the channels and the mode width on the relative minimum distance between the inclusions. Reducing the power of the channel mode and shifting its position toward a higher intensity have competing effects on the effective thermal conductivity of the material. As shown in sections 5 (see Figure 23), as a result, we still have an increase in the effective thermal conductivity with an increase in the ratio d/b.

6.3. Effect of LHF Flow Angles on Thermal Conductivity

In material with irregularly arranged inclusions, LHF do not flow strictly along the applied temperature macro-gradient. Figure 54 shows a fragment of heat fluxes map in material with inclusions placement parameters: $a = 128h$, $b = 10h$, $c = 0.537$ and $d = h$ ($N = 88$). The temperature macro-gradient between the material boundaries is applied from right to left.

The map demonstrates that a significant part of LHF flows at nonzero angles to the direction of the temperature macro-gradient between the material boundaries. There are even such areas where LHF flow almost

perpendicularly to the direction of temperature macro-gradient. Thus, the heat flux passing through the sample overcomes a distance slightly greater than the distance between the left and right boundaries of the sample. Therefore, the total heat transfer resistance of the sample should increase, and the effective thermal conductivity should decrease. The heat fluxes path elongation can be described by a characteristic deviation angle of the averaged direction of heat fluxes from the direction of temperature macro-gradient between the boundaries of the sample.

Before choosing the procedure for calculating this characteristic angle, we analyzed the distribution of the angles of the deviation of LHF from the temperature macro-gradient direction. Figure 55 shows such distribution for the pattern, a fragment of which is shown in Figure 54.

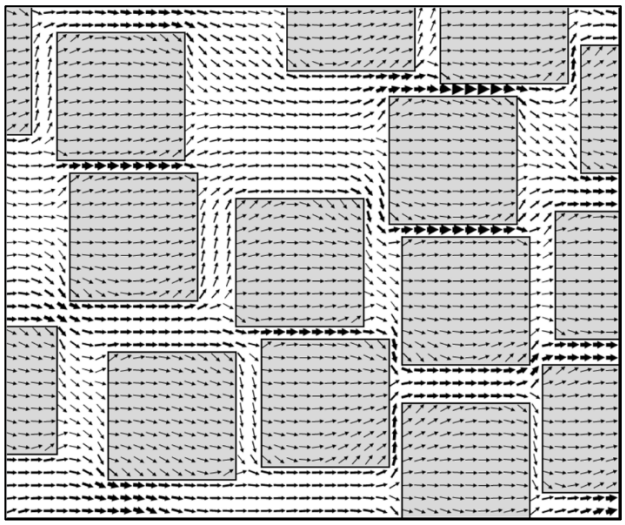

Figure 54. Fragment of heat fluxes map with sizes 48*h* × 40*h*. LHF directions were calculated according to (5) and indicated by arrows. LHF intensity is proportional to the thickness of the arrows. Heat-insulating inclusions are gray.

Figures 56 – 58 show that the character of the angular distribution of LHF is the same in large series of tests. The inclusions placement parameters influence the distribution characteristics.

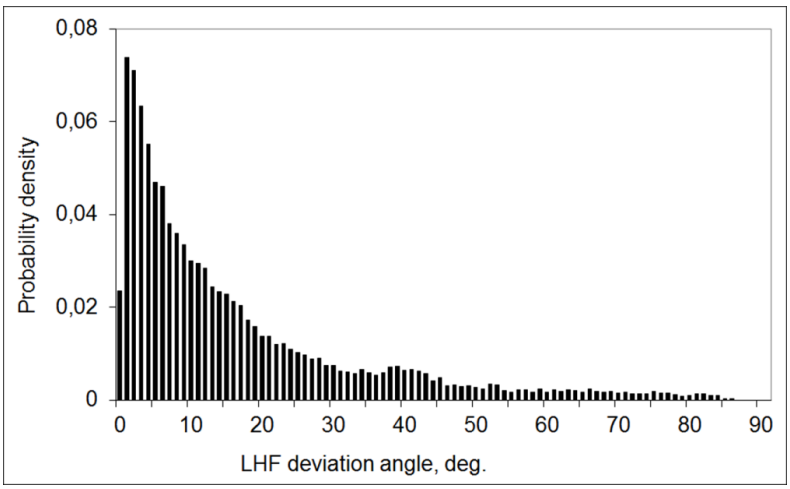

Figure 55. Angular distribution of LHF deviation from temperature macro-gradient direction in test which shown in Figure 54.

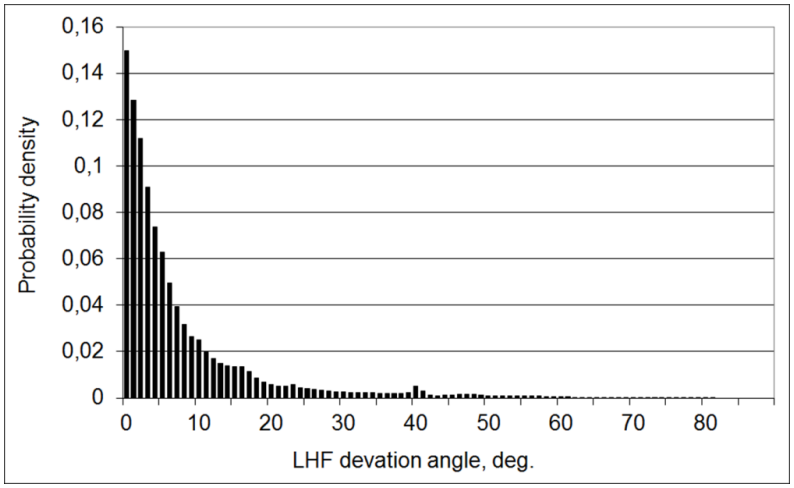

Figure 56. Angular distribution of LHF deviation from temperature macro-gradient direction in series of 800 tests: $a = 128h$, $b = 7h$, $d = 2h$, and $c = 0.1$.

It should be noted that separate modes are seen on the right tails of these distributions. Analyzing LHF patterns we defined the reasons of existence of the mode, corresponding to an angle of about 40 degrees. Figure 54 shows that LHF flow through the inclusions corners at an angles

of about 40 – 45 degrees. The decrease in the inclusions size at their constant concentration corresponds to an increase in the inclusions number and, correspondingly, the number of angular regions through which LHF flow at above mentioned angles.

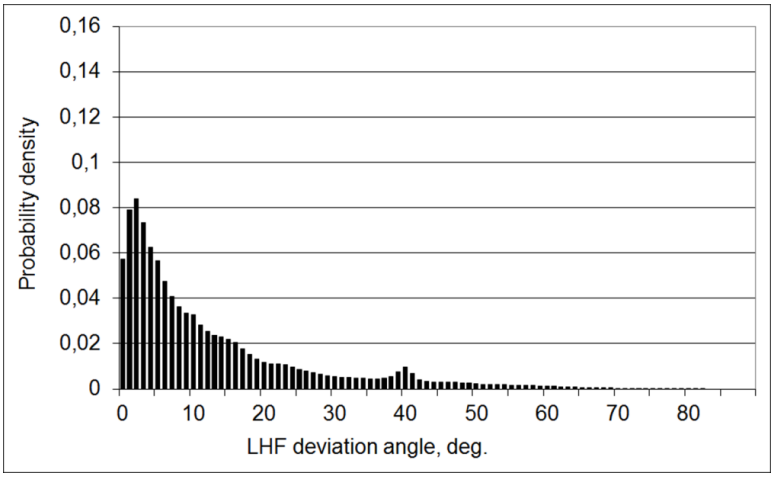

Figure 57. Angular distribution of LHF deviation from temperature macro-gradient direction in series of 800 tests: $a = 128h$, $b = 7h$, $d = 2h$, and $c = 0.245$.

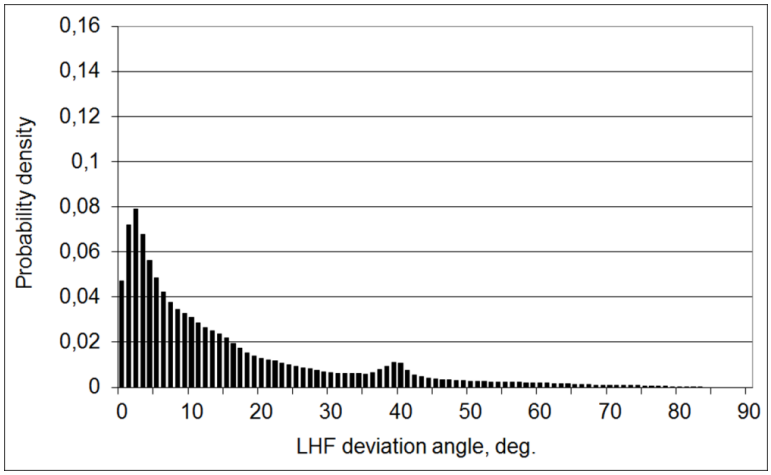

Figure 58. Angular distribution of LHF deviation from temperature macro-gradient direction in series of 800 tests: $a = 128h$, $b = 7h$, $d = 2h$, and $c = 0.39$.

Thus, the appearance of the mode on the LHF angular distribution is only due to the rectangular shape of the inclusions and demonstrates the LHF passage through their corners.

The mode value of the most similar distributions corresponds to the range of 4 – 8 degrees and depends slightly on the inclusions placement parameters. Therefore, we did not consider the angular distribution mode as the characteristic angle. As a characteristic angle, we considered the following two variants: the average value of angle $<\varphi>$ (the first initial moment of the distribution, which is determined in the standard way) and the angle of $<\varphi_W>$, while the statistical weighting is performed from the magnitude of the module vector of LHF density:

$$<\varphi_W>=\frac{\sum_{i,j}\varphi_{i,j}\left|j_{i,j}\right|}{\sum_{i,j}\left|j_{i,j}\right|}, \tag{105}$$

where $|j_{i,j}|$ is the module vector of LHF density, determined according to (91) at the counting grid node with numbers i, j; and $\varphi_{i,j}$ is the angle between the temperature macro-gradient and the direction of the LHF vector at the same node, determined according to (92).

Figures 59 and 60 show the correlation scattering fields of the LHF average deviation angle $<\varphi>$ with the relative effective thermal conductivity κ_e of the material with the placement parameters: $a = 128h$, $b = 10h$, $c = 0.34$, $d = h$ and the LHF average deflection angle $<\varphi_W>$ with κ_e of the same material, respectively. The inclination angle value of scattering ellipses shows that anti-correlation exists between the selected angles ($<\varphi>$, $<\varphi_W>$) and κ_e. The anti-correlation is stronger in the case of $<\varphi_W>$.

Figures 61 and 62 show dependence of the correlation coefficients between κ_e and $<\varphi>$, and also between κ_e and $<\varphi_W>$ for the parameters $a = 128h$, $b = 10h$, $d = h$ and $a = 128h$, $b = 10h$, $d = 4h$, respectively on inclusions concentration.

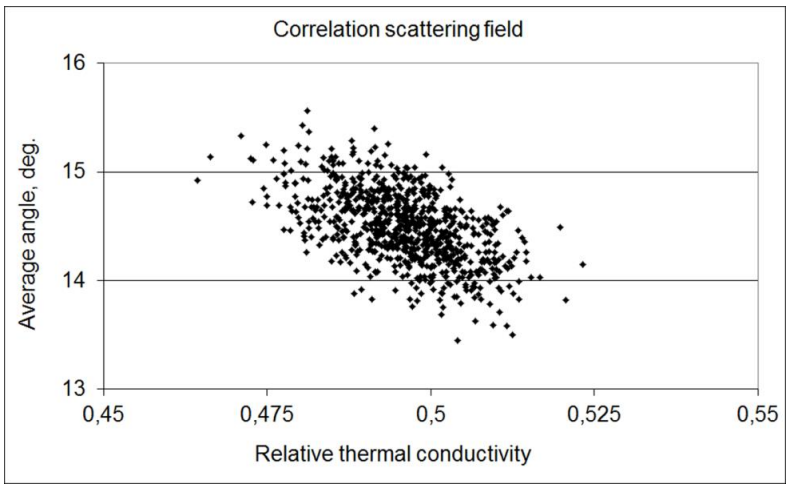

Figure 59. Correlation scattering field of the average angle of LHF deviation from temperature macro-gradient direction and relative effective thermal conductivity in series of 800 tests: $a = 128h$, $b = 10h$ $c = 0.34$, and $d = h$.

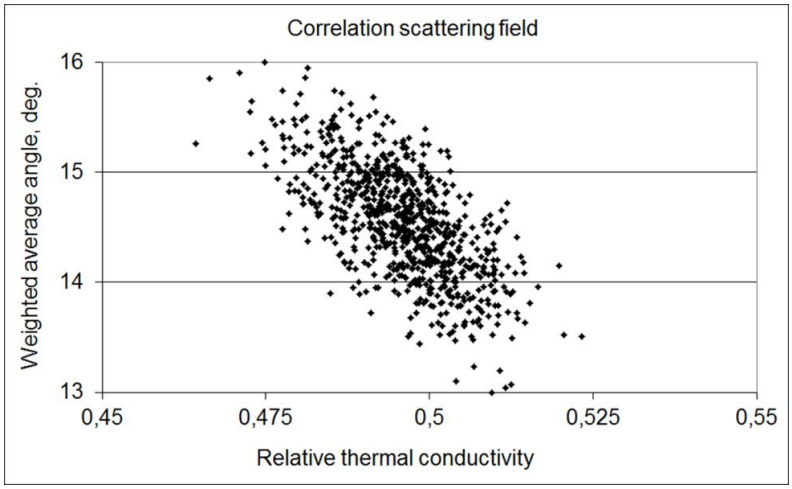

Figure 60. Correlation scattering field of the $<\varphi_W>$ from temperature macro-gradient direction and relative effective thermal conductivity in a series of 800 tests: $a = 128h$, $b = 10h$ $c = 0.34$, and $d = h$.

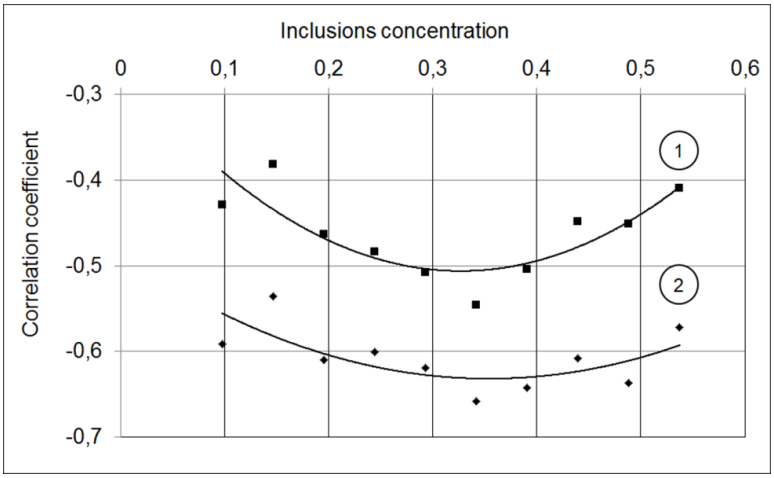

Figure 61. Dependences of the correlation coefficient between κ_e and $<\varphi>$ (curve 1), and the correlation coefficient between κ_e and $<\varphi_W>$ (curve 2) on inclusions concentration: $a = 128h$, $b = 10h$, and $d = h$.

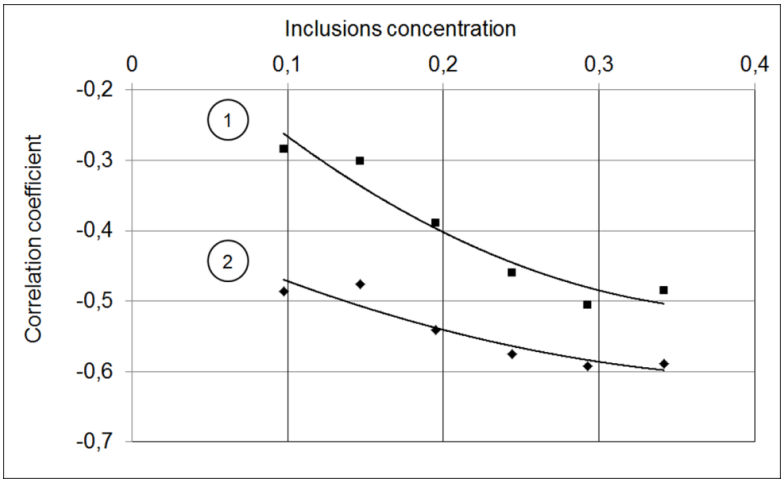

Figure 62. Dependences of the correlation coefficient between κ_e and $<\varphi>$ (curve 1), and the correlation coefficient between κ_e and $<\varphi_W>$ (curve 2) on inclusions concentration: $a = 128h$, $b = 10h$, and $d = 4h$.

It is obvious that the correlation of the weighted average angle $<\varphi_W>$ with κ_e is stronger, therefore, as a characteristic angle, it is reasonable to consider the weighted average angle of LHF deviation from the temperature macro-gradient direction.

Figure 63 shows typical dependences of the weighted average angle of LHF deviation on the inclusions concentration. These dependences demonstrate a tendency of saturation or approach to the local maximum as the inclusions concentration increases. Moreover, it shows that the weighted average angle also depends on minimum distance between inclusions and this dependence becomes stronger at concentrations of 0.3 and higher.

Figures 64 and 65 show the weighted average angle of LHF as a function of the relative minimum distance d/b at different concentrations and different particle sizes of the filler. These dependences are stronger at high concentrations.

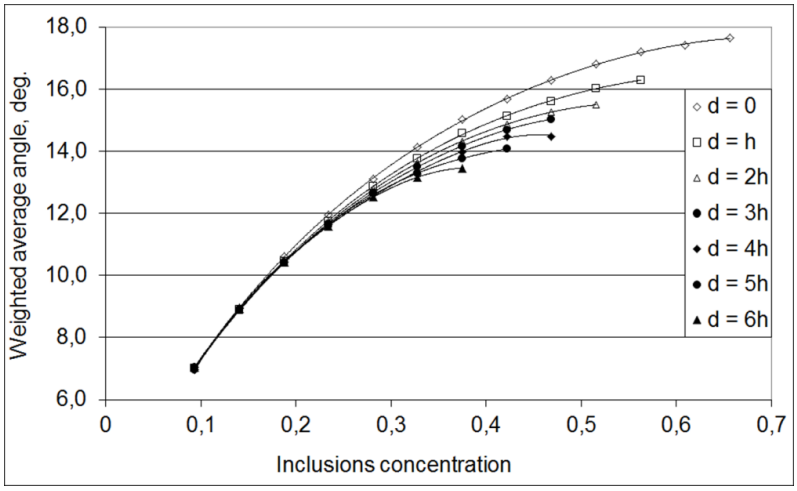

Figure 63. Dependences of weighted average angle of LHF deviation from temperature macro-gradient direction on the inclusions concentration for $a = 128h$, $b = 16h$, and different minimum distances d.

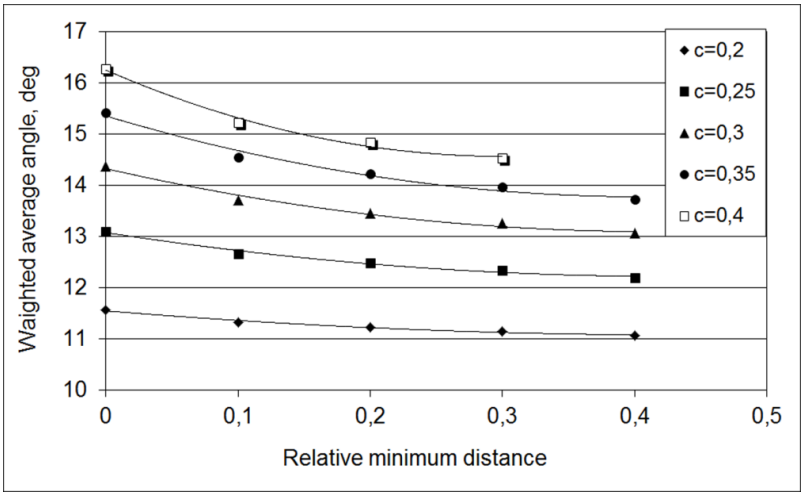

Figure 64. Dependences of weighted average angle of LHF deviation from temperature macro-gradient direction on the d/b ratio for $a = 128h$, $b = 10h$, and and various c.

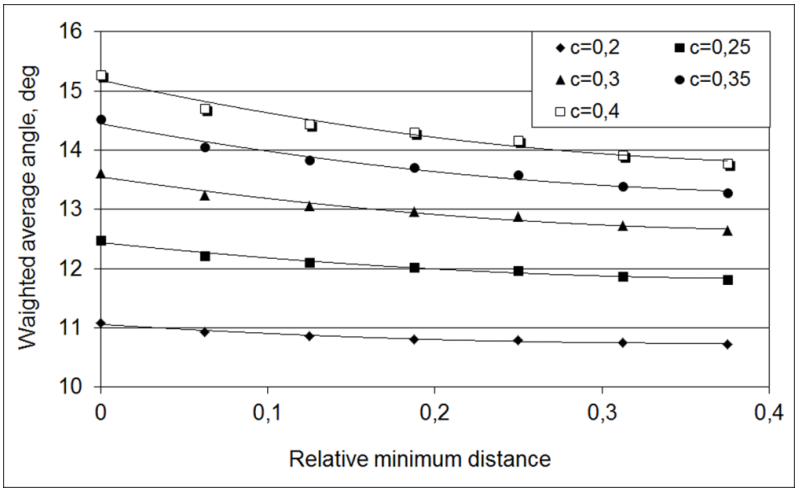

Figure 65. Dependences of weighted average angle of LHF deviation from temperature macro-gradient direction on the d/b ratio for $a = 128h$, $b = 16h$, and various c.

Figures 64 and 65 also show that the dependences $<\varphi_W>$ (d/b) are weakened as the ratio d/b is increased, i.e. with a decrease in the mutual influence of inclusions.

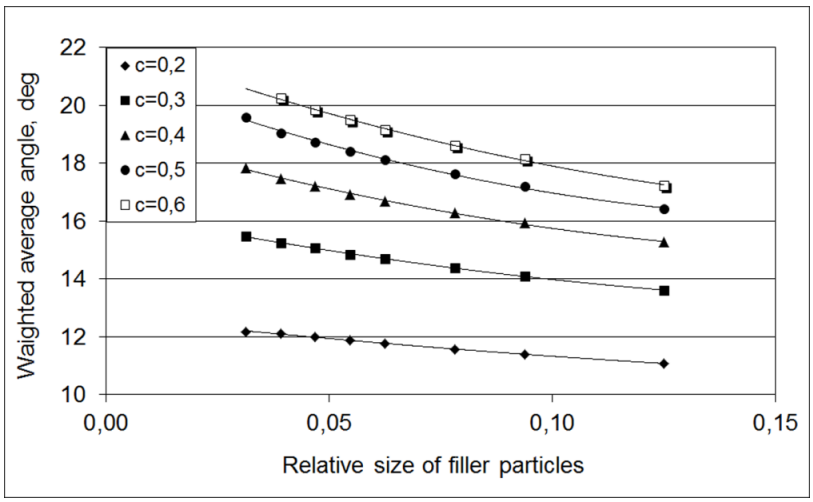

Figure 66. Dependences of weighted average angle of LHF deviation from temperature macro-gradient direction on the b/a ratio for $a = 128h$, $d = 0$ and various c.

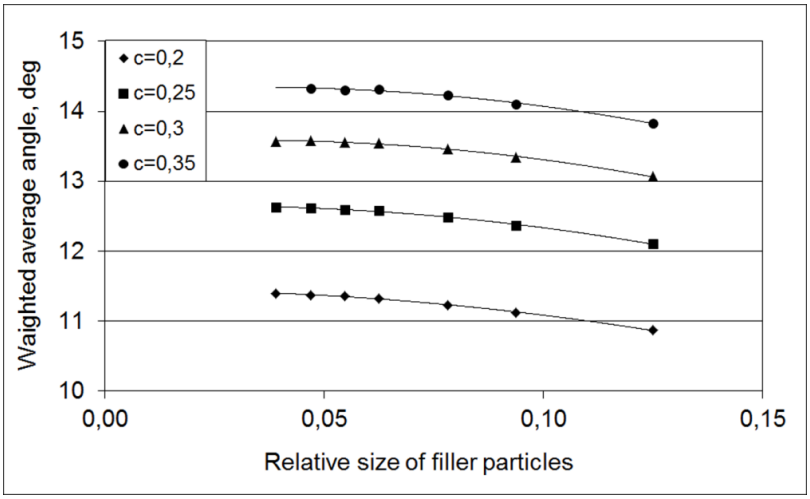

Figure 67. Dependences of weighted average angle of LHF deviation from temperature macro-gradient direction on the b/a ratio for $a = 128h$, $d = 2h$, and various c.

Figures 66 and 67 show the weighted average angle of LHF as a function of the relative particle size (b/a) of filler at different concentrations and different minimum distances between the filler

particles. In these figures, a decrease in $<\varphi_W>$ is observed with an increase in the ratio b/a. As a reason for this dependence, it can be pointed out that an increase in the ratio b/a at a constant inclusions concentration means a decrease in the number of filler particles and, consequently, the number of those regions of the matrix in which the LHF deviate from the direction of the temperature drop. In this case, for smaller values of d, when the interaction between the filler particles is more probable, the $<\varphi_W>$ (d/b) dependences are stronger.

Concentration dependences $<\varphi_W>$ are described fairly well by the approximation

$$\langle \varphi_W \rangle(c) = \alpha_\varphi \arctan\left(\sqrt[4]{(\beta_\varphi c)^3} \right), \tag{106}$$

where α_φ, and β_φ are the fitting coefficients.

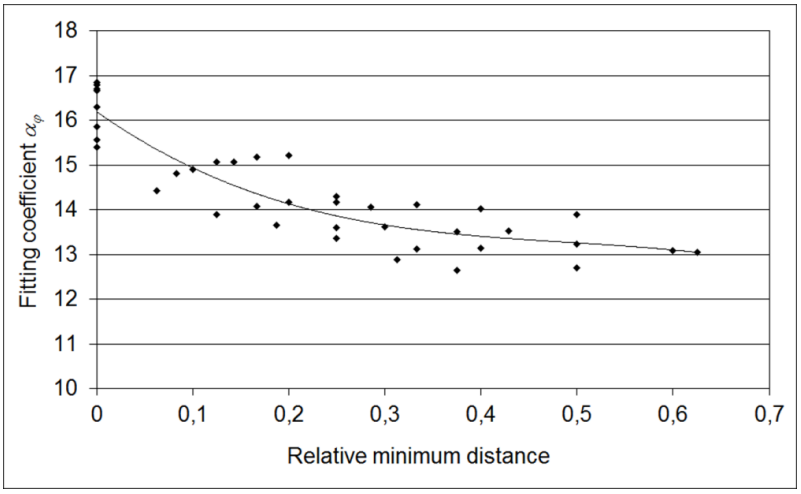

Figure 68. Dependence of the fitting coefficient α_φ on the d/b for all b/a.

Figures 68 – 69 show the dependencies of the fitting coefficients on the relative minimum distance d/b between inclusions. These graphs contain points with different values of the relative size of the inclusions

b/a. The indicated values differ 4 times. In this case, the spread of the values of the fitting factors does not exceed 12%. In the first approximation, we can assume that there is no dependence of the magnitude of the fitting coefficients on the relative size of the inclusions.

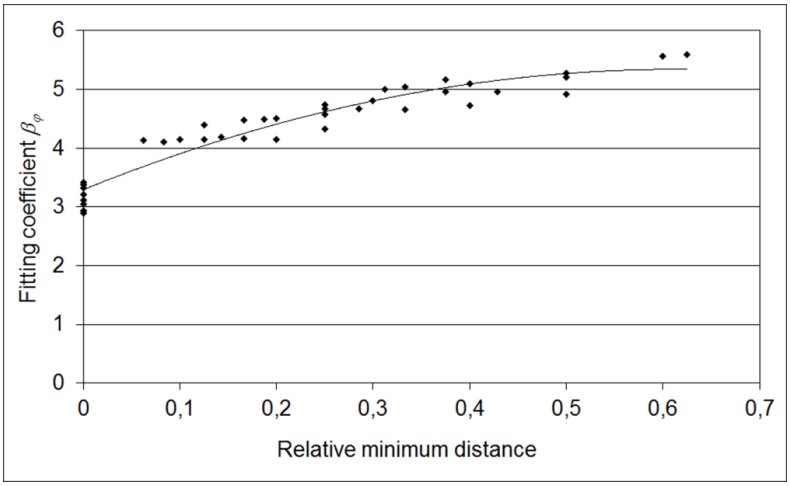

Figure 69. Dependence of the fitting coefficient β_φ on the d/b for all b/a.

As expected, the values of both fitting coefficients tend to some constant values with increasing d/b ratio and approaching it to 1.

6.4. SUMMARY

1) It was found that the statistical distribution of the modulus of the density vector of local heat fluxes is multimodal. It is shown that this distribution consists of the distributions of local fluxes that flow inside the inclusions, as well as in the region of the dark matrix and in the region of induced heat-conducting channels.
2) At high inclusions concentrations (c > 0.25), beyond the applicability limits of the GCT, individual modes of the LHF

distribution can be completely satisfactorily approximated by the log-normal distribution.

3) For the case of low concentrations, the mode of distribution of local heat fluxes, passing through the regions of the dark matrix can split into two modes. A mode with lower values of the modulus of the density vector of local heat fluxes is formed in the region of a dark matrix immediately adjacent to the boundaries of inclusions or located between closely located inclusions. The mode with higher LHF values corresponds to the rest of the dark matrix, whose dimensions are comparable to the size of the inclusion.
4) Changes in the placement parameters of inclusions in conditions when there is a mutual influence of inclusions lead to changes in the characteristics of the multimode heat flux intensity distribution. These changes, in turn, manifest themselves in the form of changes in the effective thermal conductivity of the material.
5) Local heat fluxes in composite materials with heat-insulating inclusions deviate from the direction of the temperature macro-gradient.
6) We propose to consider the weighted average angle, determined according to formula (47), as a measure of the average deviation specified in paragraph 1.
7) It is shown that the value of the weighted average angle of local heat fluxes deviation from the direction of the temperature macro-gradient is significantly correlated with the effective thermal conductivity of the sample. The effective thermal conductivity decreases with an increase in the weighted average deviation angle. This means that deviations of the local heat fluxes from the direction of the temperature macro-gradient lead to an increase in the effective path of heat fluxes in the matrix of the composite material.
8) An approximate expression for the dependence of the weighted average angle of LHF deviation from the temperature macro-gradient on inclusions concentration was proposed. This expression includes two coefficients that depend on relative

minimal distance between the filler particles. Such a form of approximation is convenient for further theoretical analysis.

AFTERWORD

Two years ago, starting work on the article [315], we simulated the impact of various factors on the integral thermal conductivity of the two-component composites. In doing so, we experimented with ordered structures of inclusions in the matrix, which were modelled separately for each series of tests. We observed that the thermal conductivity of the composite depended on the specific location of the inclusions. These facts did not fit into the framework of the dominant Maxwell-Rayleigh theory. The theory assumes the dependence of thermal conductivity on concentration, size and shape of inclusions. Nevertheless, the results of our numerical experiments have shown that changing the placement of inclusions leads to a change in the integral thermal conductivity by 10-12%. This led us to the decision to use statistical methods of investigation to study the influence of the arrangement of inclusions on the effective thermal conductivity.

As a result, we started placing the inclusions with the help of a random number generator. Concentration and size of inclusions were used as traditional model parameters for describing the thermal conductivity of composites. We considered the minimum distance between inclusions as the third parameter. The effect of this parameter on the thermal conductivity was established by us at the stage of experiments with ordered

structures. This effect was confirmed for the distances $d < b$ of inclusions at their random placement within the matrix of the composite.

In order to explain this fact, we decided to calculate the local heat fluxes in the material. The primary study of the fluxes was carried out by means of visualization of a numerical solution. The study of the visualized flow maps allowed us to identify the characteristic areas of the material that received the names of the dark matrix and induced channels. It turned out that the minimum distance between inclusions affects the fluxes maps when the inclusions are close. In addition, the paths of local flows were not straight, but tortuous. The number and curvature of the turns of their paths also depended on the placement parameters of the inclusions.

The next step was to study the statistical distribution of fluxes in terms of intensity and direction. It was found that these distributions turned out to be multi-modal. The results of numerical experiments have made it possible to correlate the modes of the heat fluxes intensity distribution with the characteristic regions of the composite matrix, namely, the dark matrix and the induced channels. We have introduced the parameter "weighted average angle of deviation from the macro-gradient of temperature" to characterize the tortuosity of the paths of local heat fluxes. We have shown that this parameter is significantly correlated with the effective thermal conductivity of the composite. Its influence on the thermal conductivity is explained by the increase in the path length of the local heat fluxes in the composite matrix. The foregoing indicates that the placement of inclusions and the intensity of heat fluxes should be taken into account in the study of thermal conductivity. Accounting for this influence is possible within the framework of the statistical approach.

The angular distribution of the local heat fluxes turned out to be quite complex and consisting of several modes. A detailed investigation of the angular distribution of heat fluxes is the following obvious problem. Correlation between the weighted average angle and effective thermal conductivity is not exhaustive. We hope to find a correlation between the parameters of the modes of distribution of the local heat fluxes intensity and the effective thermal conductivity. The search for this correlation is also the matter of the near future. In addition, the mono-disperse model

does not correspond to the observed structure of most composite materials. Therefore, the study of the statistical characteristics of local heat fluxes in poly-disperse structures is also an actual problem.

Thus, this study is difficult to complete, it can only be suspended, which the authors did for a while to write this book.

REFERENCES

[1] Al-Homoud, M. S. 2005. “Performance characteristics and practical applications of common building thermal insulation materials.” *Build. Environ*. 40: 353–366.

[2] Patnaik, A., Mvubu, M., Muniyasamy, S., Botha, A., and Anandjiwala, R. D. 2015. “Thermal and Sound Insulation Materials from Waste Wool and Recycled Polyester Fibers and their Biodegradation Studies.” *Energy Build.* 92 (I): 161–169.

[3] Asdrubali, F., D’Alessandro, F., and Schiavoni, S. 2015. “A Review of Unconventional Sustainable Building Insulation Materials.” *Sustainable Mater. Technol.* 4: 1–17.

[4] Peavy, B. A. 1996. “A heat transfer note on temperature dependent thermal conductivity.” *J. Therm. Insul. Build. Envelopes* 20: 76–90.

[5] Budaiwi, I. M., Abdou, A. A., and Al-Homoud, M. S. 2002. “Variations of thermal conductivity of insulation materials under different operating temperatures: impact on envelope induced cooling load.” *J. Archit. Eng.* 8(4): 125–32.

[6] Peruzzi, L., Salata, F., Vollaro, A. D. L., and Vollaro, R. D. L. 2014. “The reliability of technological systems with high energy efficiency in residential buildings.” *Energy Build*. 68: 19–24.

[7] Manohar, K. 2012. “Experimental investigation of building thermal insulation from agricultural by-products.” *Br. J. Appl. Sci. Technol*. 2 (3): 227–239.

[8] Milutien, E., Staniškis, J. K., Kručius, A., Augulien, V., and Ardickas, D. 2012. "Increase in buildings sustainability by using renewable materials and energy." *Clean Techn. Environ. Policy* 14: 1075–1084.

[9] Tanaka, T., Kozako, M., and Okamoto, K. 2012. "Toward High Thermal Conductivity Nano Micro Epoxy Composites with Sufficient Endurance Voltage." *J. Int. Counc. Electr. Eng*. 2 (1): 90-98.

[10] Yung, K. C., and Liem, H. 2007. "Enhanced Thermal Conductivity of Boron Nitride Epoxy-Matrix Composite through Multi-Modal Particle Size mixing." *J. Appl. Polym. Sci*. 106: 3587–3591.

[11] Xu, Y., and Chung, D. D. L. 2000. "Increasing the Thermal Conductivity of Boron Nitride and Aluminium Nitride Particle Epoxy-Matrix Composites by Particle Surface Treatments." *Compos. Interfaces* 7 (4): 243–256.

[12] Sato, K., Horibe, H., Shirai, T., Hotta, Y., Nakano, H., Nagai, H., Mitsuishi, K., and Warari, K. 2010. "Thermally Conductive Composite Films of Hexagonal Boron Nitride and Polyimide with Affinity-enhanced Interfaces." *J. Mater. Chem*. 20: 2749–2752.

[13] Zhi, C. Y., Bando, Y., Terano, T., Tang, C. C., Kuwahara, H., and Golbery, D. 2009. "Towards Thermoconductive, Electrically Insulating Polymeric Composites with Boron Nitride Nanotubes as Fillers." *Adv. Funct. Mater*. 19: 1857–1862.

[14] Andritsch, T., Kochetov, R., Gebrekiros, Y. T., Morshuis, P. H. F., and Smit, J. J. 2010. "Short-term DC Breakdown Strength in Epoxy-based BN Nano- and Micro composites." *Proc. IEEE ICSD*, B2 (3): 179–182.

[15] Terano, T., Bando, Y., Mitome, M., Zhi, C., Tang, C., and Golberg, D. 2009. "Thermal Conductivity Improvement of Polymer Films by Catechin-Modified Boron Nitride Nanotubes." *J. Phys. Chem*. C 113: 13605–13609.

[16] Konzelmann S., Hoffmann C., Merte R., and Peier D. 2008. "Thermal and Electrical Properties of Aluminium Nitride Filled Epoxy-resin Compound." *IEEE Trans. Dielectr. Electr. Insul*. 15 (2): 327–333.

[17] Schulte-Fischedick, J., Dreißigacker, V., and Tamme, R. 2007. "An innovative ceramic high temperature plate-fin heat exchanger for EFCC processes." *Appl. Therm. Eng*. 27: 1285–1294.

[18] Harris, C., Kelly, K., Wang, T., McCandless, A., and Motakef, S. 2002. "Fabrication, modelling, and testing of micro-cross-flow heat exchangers." *J. Microelectromech. Systems* 11(6): 726–735.

[19] Baud, S., Thevenot, F., and Chatillon, C. 2003. "High temperature sintering of SiC with oxide additives: IV. Powder beds and the influence of vaporization on the behaviour of SiC compacts." *J. Eur. Ceram. Soc*. 23: 29–36.

[20] Kumar, S., Bablu, M., Ranjan, A., Manocha, L. M., and Prasad, N. E. 2017. "Fabrication of 2D C/C-SiC composites using PIP based hybrid process and investigation of mechanical properties degradation under cyclic heating." *Ceram. Int*. 43: 3414–3423.

[21] Patel, M., Saurabh, K., Prasad, V., and Subrahmanyam, J. 2012. "High temperature C/C–SiC composite by liquid silicon infiltration: a literature review." *Bull. Mater. Sci*. 35: 63–73.

[22] Folke, C., and Romey, I. 1999. "Efficiencies of integrated gasification combined cycle power stations with chemical quench." Proceedings of the Fifth International Conference on Technologies and Combustion for a Clean Environment, Lisboa, 1999, 779–784.

[23] Maier, H. R., and Himmelstein, K. (2000). "Design and testing of a prototype SiSiC heat exchanger for coal combustion power stations." Proceedings of the Seventh International Symposium on Ceramic Materials and Components for Engines. *Applications in Energy, Transportation and Environment Systems,* Goslar, 2000, 255–260.

[24] Joshi, H. M., and Webb, R. L. 1987. "Heat transfer and friction in the offset strip fin heat exchanger." *Int. J. Heat Mass Transfer* 30 (1): 69–84.

[25] Meschke, F., Riebler, G., Hessel, V., Schürer, J., Baier T. 2005. "Hermetic gastight ceramic micro reactors." *Chem. Eng. Tech*. 28 (4): 465–473.

[26] Stampfl, J., Wob, A., Fratzl, P., and Seidler, S. 2002. "Rapid prototyping of ceramic and polymeric cellular materials." *IFMBE Proc*. 172–173.

[27] Munro, R. G. 1997. "Material properties of a sintered-SiC." *J. Phys. Chem. Ref. Data* 26(5): 1195–1203.

[28] Liu, D. M., and Lin, B. W. 1996. "Thermal conductivity in hot-pressed silicon carbide." *Ceram. Int*. 22: 407–414.

[29] Christin, F. 2002. "Design, fabrication, and application of thermos-structural composites (TSC) like C/C, C/SiC, and SiC/SiC composites." *Adv. Eng. Mater*. 4: 903–912.

[30] Tang, S. F., Deng, J. Y., Wang, S. J., and Liu, W. C. 2007. "Fabrication and characterization of C/SiC composites with large thickness, high density and near-stoichiometric matrix by heater less chemical vapour infiltration." *Mater. Sci. Eng*., A 465: 290–294.

[31] Liu, H. C., Tsuru, H., Cooper, A. G., and Prinz, F. B. 2005. "Rapid prototyping methods of silicon carbide micro heat exchangers." *Proc. Inst. Mech. Eng., B*: J. Eng. Manuf. 219: 525–538.

[32] Krenkel, W., and Berndt, F. 2005. "C/C-SiC Composites for Space Applications and Advanced Fraction Systems." *Mater. Sci. and Eng., A* 412 (1-2): 177–181.

[33] Hui, P. M., Zhang, X., Markworth, A. J., and Stroud, D. 1999. "Thermal Conductivity of Graded Composites: Numerical simulations and an Effective Medium Approximation." *J. Mat. Sci*. 34: 5497–5503.

[34] Becker, R., and Richmond, O. 1994. "Incorporation of microstructural geometry in material modelling." *Modelling Simul. Mater. Sci. Eng*. 2: 439–454.

[35] Fan, Z., Tsakiropoulos, P., and Miodownik, A. P. 1994. "A generalized law of mixres." *J. Mater. Sci*. 29: 141–150.

[36] Argyris, J., Doltsinis, I. S., Eggers, M., and Handel, R. 1994. "Studies on ceramic coatings. Deduction of mechanical and thermal properties from the microstructure of the material." *Comput. Meth. App. Mech. Eng*. 111(3–4): 203–234.

[37] Miller, D. P., Lannutti, J. J., and Noebe, R. D. 1993. "Fabrication and Properties of Functionally Graded Ni/Al/Al2O3 Composites." *J. Mater. Res*. 8 (8): 2004–2013.

[38] Bergman, D. J., and Stroud, D. 1992. "Physical Properties of Macroscopically Inhomogeneous Media." *Solid-State Phys*. 46: 147–269.

[39] Maxwell, J. C. 1904. "A treatise on electricity and magnetism." Oxford University Press, vol. I, 3rd Ed., 435.

[40] Strutt, J. W. (Lord Rayleigh). 1982. "On the influence of obstacles arranged in rectangular order upon the properties of a medium." *Philos. Mag*. 34: 481–502.

[41] Hamilton, R. L., and Crosser, O. K. 1962. "Thermal Conductivity of Heterogeneous Two Component System." *Ind. Eng. Chem. Fundam*. 1 (3): 187–191.

[42] Hatta, H., and Taya, M. 1986. "Thermal Conductivity of Coated Filler-Composites." *J. Appl. Phys*. 59: 1851–1860.

[43] Powell, B. R., Jr., Youngblood, G. E., Hasselman, D. P. H., and Bentsen, L. D. 1980. "Effect of Thermal Expansion Mismatch on the Thermal Diffusivity of Glass-Ni Composites." *J. Am. Ceram. Soc*. 63: 581–586.

[44] Willis, J. R. 1977. "Bounds and Self-Consistent Estimates for the Overall Properties of Anisotropic Composites." *J. Mech. Phys. Solids* 25: 185–202.

[45] Hasselman, D. P. H. 1978. "Effect of Cracks on Thermal Conductivity." *J. Comp. Mat*. 12 (4): 403–405.

[46] Yu, A., Ramesh, P., Sun, X., Bekyarova, E., Itkis M. E., and Haddon R. C. 2008. "Enhanced Thermal Conductivity in a Hybrid Graphite Nano platelet – Carbon Nanotube Filler for Epoxy Composites." *Adv. Mater*. 20: 4740–4744.

[47] Shenogin, S., Xue, L., Ozisik, R., Keblinski, P., and Cahill, D. G. 2004. "Role of thermal boundary resistance on the heat flow in carbon-nanotube composites." *J. App. Phys*. 95 (12), 8136–8144.

[48] Zhou, W., Wang, C, Ai, T., Wu, K., Zhao, F., and Gu, H. 2009. "A novel fibre-reinforced polyethylene composite with added silicon nitride particles for enhanced thermal conductivity." *Composites: Part A* 40: 830–836.

[49] Ruch, P. W., Beffort, O., Kleiner, S., and Weber L., Uggowitzer, P. J. 2006. "Selective interfacial bonding in Al (Si)–diamond composites and its effect on thermal conductivity." *Compos. Sci. Technol*. 66:2677–2685.

[50] Cao X. Q., Vassenb, R., and Stoever, D. 2004. "Ceramic materials for thermal barrier coatings." *J. Eur. Ceram. Soc*. 24: 1–10.

[51] Hasselman, D. P. H., and Johnson, L.F. 1987. "Effective thermal conductivity of composites with interfacial thermal barrier resistance." *J. Compos. Mater*. 21 (6): 508-515.

[52] Tavangar, R., Molina, J., and Weber, L. 2007. "Assessing Predictive Schemes for Thermal Conductivity Against Diamond-Reinforced

Silver Matrix Composites at Intermediate Phase Contrast." *Scripta Mater*. 56 (5): 357-360.

[53] Hale, D. K. 1976. "Review: The physical properties of composite materials." *J. Mater. Sci*. 11: 2105–2141.

[54] Hashin, Z. 1983. "Analysis of Composite Materials-A Survey." *J. App. Mech*. 50: 481–505.

[55] Torquado, S. 1991. "Random heterogeneous media: microstructure and improved bounds on effective properties." *Appl. Mech. Rev*. 44 (2), 37–76.

[56] Weber, L., Dorn, J., and Mortensen, A. 2003. "On the electrical conductivity of metal matrix composites containing high volume fractions of non-conducting inclusions." *Acta Mater*. 51 (11): 3199–3211.

[57] Bruggeman, D. A. G. 1935. "Berechnung verschiedener physikalischer kkonstanten von heterogenen ssubstanzen. Annalen der Physik." 416(7): 636–664. ["Calculation of different physical constants of heterogeneous substances." *Ann. Phys*. 416(7): 636–664.

[58] Landauer, R. 1952. "The electrical resistance of binary metallic mixtures." *J. Appl. Phys*. 23 (7): 779–784.

[59] Every, A. G., Tzou, Y., Hasselman, D. P. H., and Raj, R. 1992. "The effect of particle size on the thermal conductivity of ZnS/diamond composites." *Acta Metall. Mater*. 40 (1): 123-129.

[60] Pietrak, K., and Wiśniewski, T. S. 2015. "A review of models for effective thermal conductivity of composite materials." *J. Power Technol*. 95 (1): 14–24.

[61] Nielsen, L. E. 1974. "The Thermal and Electrical Conductivity of Two-Phase Systems." *Ind. Eng. Chem. Fund*. 3 (1): 17–20.

[62] Donea, J. 1972. "Thermal Conductivities Based on Variation Principles." *J. Compos. Mater*. 6 (2): 262–266.

[63] Benveniste, Y. 1987. "Effective Thermal Conductivity of Composites with a Thermal Contact Resistance Between the Constituents: Nondilute Case." *J. Appl. Phys*. 61: 2840–2843.

[64] Nan, C.-W., Birringer, R., Clarke, D. R., and Gleiter, H. 1997. "Effective Thermal Conductivity of Particulate Composites with Interfacial Thermal Resistance." *J. Appl. Phys*. 81: 6692–6699.

[65] Bai, G., Jiang, W., and Chen, L. 2006. “Effect of Interfacial Thermal Resistance on Effective Thermal Conductivity of MoSi2/SiC Composites.” *Mater. Trans*. 47 (4): 1247–1249.

[66] Rocha, R. P. A., and Cruz, M. A. E. 2001. “Computational of the Effective Conductivity of Unidirectional Fibrous Composites with an Interfacial Thermal Resistance.” *Numer*. *Heat Transfer, Part A* 39(2): 179–203.

[67] Xu, Y., Wang, H., Tanaka, Y., Shimono, M., and Yamazaki, M. 2007. “Measurement of Interfacial Thermal Resistance by Periodic Heating and a Thermo-Reflectance Technique.” *Mater. Trans*. 48 (2): 148–150.

[68] Mori, T., and Tanaka, K. 1973. “Average stress in matrix and average elastic energy of materials with misfitting inclusions.” *Acta Metall*. 21: 571–574.

[69] Graham, S., and McDowell, D. 2003. “Numerical analysis of the transverse thermal conductivity of composites with imperfect interfaces.” *J. Heat Transfer* 125: 389–393.

[70] Kanit, T., Forest, S., Galliet, I., Mounoury, V., and Jeulin, D. 2003. “Determination of the size of the representative volume element for random composites: statistical and numerical approach.” *Int. J. Solids Struct*. 40: 3647-3679.

[71] Kamiński, M. 2003. “Homogenization of Transient Heat Transfer Problems for Some Composite Materials.” *Int. J. Eng. Sci*. 41: 1-29.

[72] Furmansky, P. 1997. “Heat conduction in composites: homogenization and macroscopic behaviour.” *App. Mech. Rev*. 50 (6): 327–355.

[73] Hien, T. D., and Kleiber, M. 1977. “Stochastic finite element modelling in linear transient heat transfer.” *Comput. Meth. Appl. Mech. Eng*. 144: 111–124.

[74] Auriault, J. L., and Ene, H. I. 1994. “Macroscopic modelling of heat transfer in composites with interfacial thermal barrier.” *J. Heat Mass Transfer* 37(18): 2885–2892.

[75] Delouei, A. A., Kayhani, M. H., and Norouzi, M. 2012. “Exact analytical solution of unsteady axi-symmetric conductive heat transfer in cylindrical orthotropic composite laminates.” *Int. J. Heat Mass Transfer* 55: 4427–4436.

[76] Sadowski, T., Ataya, S., and Nakonieczny, K. 2009. "Thermal analysis of layered FGM cylindrical plates subjected to sudden cooling process at one side - Comparison of two applied methods for problem solution." *Comput. Mater*. Sci. 45: 624–632.

[77] Kim, J. S., and Muliana, A. H. 2010. "A two-scale homogenization framework for nonlinear effective thermal conductivity of laminated composites." *Acta Mech.* 212: 319–34.

[78] Cho, Y. B., and Averill, R. C. 2000. "First order zig-zag sub laminate plate theory and finite element model for laminated composite and sandwich panels." *Compos. Struct*. 50(1): 1–15.

[79] Averill, R. C., and Yip, Y. C. 1996. "Development of simple, robust, finite elements based on refined theories for thick laminated beam." *Comput. Struct*. 59(3), 529–546.

[80] Chung, P. W., Tamma, K. K., and Namburu, R. R. 2001. "Homogenization of temperature-dependent thermal conductivity in composite materials." *J. Thermophys. Heat Transf*. 15: 10–17.

[81] Haj-Ali, R. M., and Muliana, A. H. 2004. "A multi-scale constitutive framework for the nonlinear analysis of laminated composite materials and structures." *Int. J. Solids Struct*. 41(13): 3461–3490.

[82] Jiang, M., Jasiuk, I., and Ostoja-Starzewski, M. O. 2002. "Apparent elastic and elastoplastic behaviour of periodic composites." *Int. J. Solids Struct*. 39: 199–212.

[83] Khan, K. A., and Muliana, A. H. 2010. "Effective thermal properties of viscoelastic composites with field dependent constituent properties." *Acta Mech.* 209: 153–178.

[84] Kolodziej, J. A., and Konczak, Z. 1994. "Determination of effective thermal conductivity for a laminated composite slab in a nonlinear case." *Int. Commun. Heat Mass Transf*. 21: 403–410.

[85] Kulkarni, M. R., and Brady, R. P. 1997. "A model of global thermal conductivity in laminated carbon/carbon composites." *Compos. Sci. Tech*. 57: 277–285.

[86] Drugan, W. J., and Willis, J. R. 1996. "A Micromechanics-Based Nonlocal Constitutive Equation and Estimates of Representative Volume Element Size for Elastic Composites." *J. Mech. Phys. Solids* 44 (4): 497-524.

[87] Xia Z., Zhou, C., Yong Q., and Wang, X. 2006. "On selection of repeated unit cell model and application of unified periodic boundary

conditions in micro-mechanical analysis of composites." *Int. J. Solids. Struc*. 43: 266–278.

[88] Tyrus, J. M., Gosz, M., and DeSantiago, E. 2007. "A local finite element implementation for imposing periodic boundary conditions on composite micromechanical models." *Int. J. Solids Struc*. 44: 2972–2989.

[89] Bianchi, S., Corigliano, A., Frassine, R., and Rink, M. 2006. "Modelling of interlaminar fracture processes in composites using interface elements." *Compos. Sci. Technol*. 66, 255–263.

[90] Llorca, J. and Segurado, J. 2004. "Three-dimensional multi-particle cell simulations of deformation and damage in sphere-reinforced composites." *Mater. Sci. Eng. A* 365: 267–274.

[91] Thoutireddy, P., Molinari, J., Repetto, E., and Ortiz, M. 2002. "Tetrahedral composite finite elements." *Int. J. Num. Meth. Eng*. 53: 1337–1351.

[92] Kari, S., Berger, H., Rodriguez-Ramos, R., and Gabbert, U. 2007. "Computational evaluation of effective material properties of composites reinforced by randomly distributed spherical particles." *Compos. Struct*. 77: 223–231.

[93] Christensen, R. M., and Lo, K. H. 1997. "Solutions for effective shear properties of three phase sphere and cylinder models." *J. Mech. Phys. Solids* 27: 315–30.

[94] Hine, P. J, Lusti, H. R., and Gusev, A. A. 2002. "Numerical simulation of the effects of volume fraction, aspect ratio and fibre length distribution on the elastic and thermo-elastic properties of short fibre composites." *Compos. Sci*. Tech. 62: 1445–53.

[95] Milton, G. W. 1982. "Bounds on the elastic and transport properties of two-component composites." *J. Mech. Phys. Solids* 30: 177–91.

[96] Kaczmarczyk Ł., Pearce C. J., and Bićanić N. 2008. "Scale transition and enforcement of RVE boundary conditions in second-order computational homogenization." *Int. J. Numer. Meth. Eng*. 74: 506–522.

[97] Trias, D., Costa, J., Turon, A., and Hurtado, J. E. 2006. "Determination of the Critical Size of a Statistical Representative Volume Element (SRVE) for Carbon Reinforced Polymers." *Acta Mater*. 54 (13): 3471–3484.

[98] Shan, Z., and Gokhale, A. 2002. “Representative Volume Element for Non-Uniform Microstructure.” *Comput. Mater. Sci*. 24: 361–379.

[99] Romero, A., and Masad, E. 2004. “Relationship Between the Representative Volume Element and Mechanical Properties of Asphalt Concrete.” *J. Mater. Civ. Eng*. 193: 3221-3238.

[100] Graham, S., and Yang, N. 2003. “Representative Volumes of Materials Based on Microstructural Statistics.” *Scripta Mater*. 48: 269-274.

[101] Jacob, G. C., Starbuck, J. M., Fellers, J. F., Simunovic, S., and Beoman, R. G. 2006. “Crashworthiness of various rancom chopped carbon fibre reinforced epoxy composite materials and their strain rate dependence.” *J. Appl. Polym. Sci*. 101: 1477–86.

[102] Corum, J. M., Battiste, R. L., Ruggles, M. B., and Ren, W. 2001. “Durability-based design criteria for a chopped-glass-fibre automotive structural composite.” *Compos. Sci. Technol*. 61: 1083–1095.

[103] Quek, S. C., Waas, A., Shahwan, K. W., and Agaram, V. 2004. “Compressive response and failure of braided textile composite: part 2-computations.” *Int. J. Non–Linear Mech*. 39: 649–663.

[104] Heinrich C., Aldridge M., Wineman A. S., Kieffer J., Waas A. M., and Shahwan K. 2012. “The influence of the representative volume element (RVE) size on the homogenized response of cured fiber composites.” *Modelling Simul. Mater. Sci. Eng*. 20: 075007.

[105] Grufman, C., and Ellyin, F. 2007. “Determining a representative volume element capturing the morphology of fibre reinforced polymer composites.” *Compos. Sci. Technol*. 67: 766–775.

[106] Lissenden, C. J., Arnold, S. M., and Iyer, S. K. 2000. “Flow/damage surfaces for fiber-reinforced metals having different periodic microstructures.” *Int. J. Plast*. 16: 1049–1074.

[107] Segurado, J., and Llorca, J. A 2002. “Numerical Approximation to the Elastic Properties of Sphere-Reinforced composites.” *J. Mech. Phys. Solids* 50: 2107–2121.

[108] Forest, S., Barbe, F., and Cailletaud, G. 2000. “Cosserat Modelling of Size Effects in the Mechanical Behaviour of Polycrystals and Multi-Phase Materials.” *Int. J. Solids Struct*. 37: 7105–7126.

[109] Michel, J., Moulinec, H., and Suquet, P. 1999. “Effectives Properties of Composite Materials with Periodic Microstructure: a

Computational Approach." *Comput. Methods Appl. Mech. Eng*. 172: 109–143.

[110] Pan, Y., Iorga L., and Pelegri A. A. 2008. "Numerical generation of a random chopped fiber composite RVE and its elastic properties." *Compos. Sci*. *Technol*. 68: 2792–2798.

[111] Böhm, H. J, Eckschlager, A., and Han, W. 2002. "Multi-inclusion unit cell models for metal matrix composites with randomly oriented discontinuous reinforcements." *Comput. Mat. Sci*. 25: 42–53.

[112] Faessel, M., Delisée, C., Bos, F., and Castéra, P. 2005. "3D modelling of random cellulosic fibrous networks based on X-ray tomography and image analysis." *Compos. Sci. Technol*. 65: 1931–1940.

[113] Duschlbauer, D., Böhm, H. J, and Pettermann, H. E. 2006. "Computational simulation of composites reinforced by planar random fibers: homogenization and localization by unit cell and mean field approaches." *J. Compos. Mater*. 40: 2217–2234.

[114] Tu S. T., Cai W. Z., Yin Y., and Ling X. 2005. "Numerical simulation of saturation behaviour of physical properties in composites with randomly distributed second-phase." *J. Compos. Mater*. 39 (7): 617–631.

[115] Kanit, T., N'Guyen, F., Forest, S., Jeulin, D., Reed, M., and Singleton S. 2006. "Apparent and effective physical properties of heterogeneous materials: representativity of samples of two materials from food industry." *Comput. Methods Appl. Mech. Eng*. 195: 3960–3982.

[116] Swaminathan, S., Ghosh, S., and Pagano, N. J. 2006. "Statistically equivalent representative volume elements for unidirectional composite microstructures: I. Without damage." *J. Compos. Mater*. 4: 583–604.

[117] Pellisou, C., Baccou, J., Monerie, Y., and Perales, F. 2009. "Determination of the Size of the Representative Volume Element for Random Quasi-Britte Composites." *Int. J. Solid Struct*. 46: 2842–2855.

[118] Sab, K., and Nedjar, B. 2005. "Periodization of random media and representative volume element size for linear composites." *C. R. Mécanique* 333: 187–195.

[119] Gitman, I., Askes, H., and Sluys, L. 2007. "Representative volume: existence and size determination." *Eng. Fract. Mech*. 74: 2518–2534.

[120] Zeman, J., and Senjora, M. 2001. "Numerical evaluation of effective elastic properties of graphite fiber tow impregnated by polymer matrix." *J. Mech. Phys. Solids*, 49: 69-90.

[121] Marcos-Gómez, D., Ching-Lloid, J., Elizalde, M. R., Clegg, W. J., and Molina-Aldareguia, J. M. 2010. "Predicting the Thermal Conductivity of Composite Materials with Imperfect Interfaces." *Compos. Sci. Technol*. 70: 2276-2283.

[122] Li, H., Li, Sh., and Wang, Y. 2011. "Prediction of Effective Thermal Conductivities of Voven Fabric Composites Using Unit Cells at Multiple Length Scales." *J. Mater. Res*. 26: 384-394.

[123] Bensoussan, A., Lions, J. L., and Papanicolaou, G. 2011. *Asymptotic Analysis for Periodic Structures*. Providence, Rhode Island.

[124] Hassani, B., and Hinton, E. 1998. "A review of homogenization and topology optimization I–homogenization theory for media with periodic structure." *Comput. Struct*. 69: 707–717.

[125] Guedes, J. M, and Kikuchi, N. 1990. "Pre and post processing for materials based on the homogenization method with adaptive finite element methods." *Comput. Meth. Appl. Mech. Eng*. 83: 143–198.

[126] Bendsoe M. P., and Kikuchi N. 1988. "Generating optimal topologies in structural design using homogenization method." *Comput. Meth. Appl. Mech. Eng*. 71: 197–224.

[127] Suzuki, K., and Kikuchi, N. 1991. "A homogenization method for shape and topology optimization." *Comput. Meth. Appl. Mech. Eng*. 93: 291–318.

[128] Pindera, M., Khatam, H., Drago, S., and Bansal, Y. 2009. "Micromechanics of Spatially Uniform Heterogeneous Media: A Critical Review and Emerging Approaches." *Composites, Part B* 40: 349–378.

[129] Allaire, G. 1992. "Homogenization and Two-Scale Convergence." *SIAM J. Math. Anal*. 23: 1482–1518.

[130] Aboudi, J., Pindera, M., and Arnold, S. 1999. "Higher-Order Theory for Functionally Graded Materials." *Composites, Part B* 30: 777–832.

[131] Michel, J., and Suquet, P. 2004. "Computational Analysis of Nonlinear Composites Structures Using the Nonuniform

Transformation Field Analysis. Comput." *Methods Appl. Mech. Eng*. 193: 5477–5502.

[132] Guinovart-Díaz, R., Rodriguez-Ramos, R., Bravo-Castillero, J., and Maugin, G. 2005. "A Recursive Asymptotic Homogenization Scheme for Multi-Phase Fiber-Reinforced Composites." *Mech. Mater*. 37: 1119–1131.

[133] Cavalcante, M., Marques, S., and Pindera, M. 2008. "Computational Aspects of the Parametric Finite-Volume Theory for Functionally Graded Materials." *Comput. Mater. Sci*. 44: 422–438.

[134] Chatzigeorgiou, G., Charalambakis, N., and Murat, F. 2008. "Homogenization Problems of a Hollow Cylinder Made of Elastic Materials With Discontinuous Properties." *Int. J. Solids Struct*. 45: 5165–5180.

[135] Visintin, A. 2008. "Homogenization of Nonlinear Visco-Elastic Composites." *J. Math. Pures Appl*. 89: 477–504.

[136] Francfort, G., and Murat, F. 2009. "The Proofs of the Optimal Bounds for Mixtures of Two Anisotropic Conducting Materials in Two Dimensions. Mech. Mater." 41: 448–455.

[137] Tsinopoulos, S., Verbis, J., and Polyzos, D. 2000. "An Iterative Effective Medium Approximation for Wave Dispersion and Attenuation Predictions in Pariculate Composites." *Adv. Compos. Lett*. 9: 193–200.

[138] Pasternak, E., and Muhlhaus, H. B. 2005. "Generalised Homogenization Procedures for Granular Materials." *J. Eng. Math*. 52 (1): 199–229.

[139] Chen, Y. M., and Ting, J. M. 2002. "Ultra-high thermal conductivity polymer composites." *Carbon*. 40: 359-362.

[140] Kim, G. H., Lee, D., Shanker, A., Shao, L., Kwon, M. S., et al. 2015. "High thermal conductivity in amorphous polymer blends by engineered interchain interactions." *Nat Mater*. 14(3): 295–300.

[141] Singh, V. et al. 2014. "High thermal conductivity of chain-oriented amorphous polythiophene." *Nat. Nanotechnol*. 9(5): 384–390.

[142] Wong, C. P., and Bollampally, R. S. 1999. "Thermal conductivity, elastic modulus, and coefficient of thermal expansion of polymer composites filled with ceramic particles for electronic packaging." *J. Appl. Polym. Sci*. 74(14): 3396–3403.

[143] Hill, R. F., and Supancic P. H. 2002. "Thermal conductivity of platelet-filled polymer composites." *J. Am. Ceram. Soc*. 85(4): 851–857.

[144] Kurabayashi, K. 2001. "Anisotropic thermal properties of solid polymers." *Int. J. Thermophys*. 22(1): 277–288.

[145] Ohmura, T., Tsuboi, M., and Tomimura, T. 2002. "Estimation of the mean thermal conductivity of anisotropic materials." *Int. J*. 23(3): 843–853.

[146] Nagasaka, Y., and Nagashima, A. 1981. "Absolute measurement of the thermal conductivity of electrically conducting liquids by the transient hot-wire method." *J. Phys. Educ*. 14(12): 1435–1440.

[147] Mishra, V., Hardin, C. L., Garay, J. E., and Dames, C. 2015. "A 3 omega method to measure an arbitrary anisotropic thermal conductivity tensor." *Rev. Sci. Instrum*. 86(5): 054902.

[148] Bartlett, M. D., Kazem, N., Powell-Palm M. J., Huang, X., Sun, W., Malen, J. A., and Majidi, C. 2017. "High thermal conductivity in soft elastomers with elongated liquid metal inclusions." *Proc. National. Acad. Sci. USA* 114 (9): 2143–2148.

[149] Chen, H., Ginzburg, V. V., Yang, J., Yang, Y., Liu, W., Huang, Y., Du, L., and Chen B. 2016. "Thermal conductivity of polymer-based composites: Fundamentals and applications." *Prog. Polym. Sci*. 59: 41–85.

[150] Huang, H., and Ramesh Talreja, R. 2005. "Effects of void geometry on elastic properties of unidirectional fiber reinforced composites." *Compos. Sci. Technol*. 65: 1964–1981.

[151] Bulsara, V. N., Talreja, R., and Qu, J. 1999. "Damage initiation under transverse loading of unidirectional composites with arbitrarily distributed fibers." *Compos. Sci. Technol*. 59: 673–82.

[152] Campbell, F. C., Mallow, A. R., and Browning, C. E. 1995. "Porosity in carbon fiber composites: an overview of cause." *J. Adv. Mater*. 18–33.

[153] Mura, T., Shodja, H. M., and Hirose, Y. 1996. "Inclusion problems." *Appl. Mech. Rev*. 49 (10): 118–27.

[154] Kumlutas, D., and Tavman, I. H. 2006. "A Numerical and Experimental Study on Thermal Conductivity of Particle Filled Polymer Composites." *J. Thermoplast. Compos. Mater*. 19: 441–455.

[155] Danes, F., Garnier, B., and Dupuis, T. 2003. "Predicting, Measuring, and Tailoring the Transverse Thermal Conductivity of Composites from Polymer Matrix and Metal Filler." *Int. J. of Thermophys*. 24 (3): 771–784.

[156] Choi, S., and Kim, J. 2013. "Thermal conductivity of epoxy composites with a binary-particle system of aluminum oxide and aluminum nitride fillers." *Composites: Part B* 51: 140–147.

[157] Sim, L. C., Ramanan, S. R., Ismail, H., Seetharamu, K. N., and Goh, T. J. 2005. "Thermal characterization of Al2O3 and ZnO reinforced silicone rubber as thermal pads for heat dissipation purposes." *Thermochim. Acta* 430(1-2): 155–165.

[158] Sohn, H. Y., and Moreland, C. 1968. "The effect of particle size distribution on packing density." *J. Chem. Eng*. 46 (3): 162–167.

[159] Wakeman, R. J. 1975. "Packing densities of particles with lognormal size distributions." *Powder Technol*. 11: 297–299.

[160] Lee, G. W., Park, M., Kim, J., Lee, J. I., and Yoon H. G. 2006. "Enhanced thermal conductivity of polymer composites filled with hybrid filler." *Composites Part A* 37 (5): 727–734.

[161] Yang, Y. C., Chu, S. S., Chang, W. J., and Wu T. S. 2010. "Estimation of Heat Flux and Temperature Distribution in a Composite Strip and Homogeneous Foundation." *Int.* Commun. *Heat Mass Transfer* 37: 495-500.

[162] Yang, Y. C., Wu, T. S., and Wei, E. J. 2007. "Modelling of simultaneous estimating the laser heat flux and melted depth during laser processing by inverse methodology." *Int. Commun. Heat Mass Transfer* 34: 440–447.

[163] Chen, W. L., Yang, Y. C., and Chu, S. S. 2009. "Estimation of heat generation at the interface of cylindrical bars during friction process." *Appl. Thermal Eng*. 29: 351–357.

[164] Wang, S. K., Lee, H. L., and Yang, Y. C. 2009. "Inverse problem of estimating time-dependent heat generation in a frictional heated strip and foundation." *Int. Commun. Heat Mass Transfer*. 36: 925–930.

[165] Chen, W. L., and Yang, Y. C. 2008. "On the inverse heat convection problem of the flow over a cascade of rectangular blades." *Int. J. Heat Mass Transfer* 51: 4184–4194.

[166] Yang, Y. C., and Chen, W. L. 2009. "An iterative regularization method in simultaneously estimating the inlet temperature and heat-

transfer rate in a forced-convection pipe." *Int. J. Heat Mass Transfer* 52: 1928–1937.

[167] Gori, F., and Corasaniti, S. 2014. "Effective thermal conductivity of composites." *Int. J. Heat Mass Transfer* 77: 653-661.

[168] Smith, G. 1985. *Numerical Solution of Partial Differential Equations: Finite Difference Methods*. Oxford: Clarendon Press.

[169] Meerschaert, M. M., and Tadjeran, C. 2006. "Finite difference approximations for two-sided space-fractional partial differential equations." *Appl. Numer. Math.* 56: 80–90.

[170] Berger, M. J. 1984. "Adaptive Mesh Refinement for Hyperbolic Partial Differential Equations." *J. Comput. Phys*. 53: 484–512.

[171] Lynch, V. E., Carreras, B. A., del-Castillo-Negrete, D., Ferriera-Mejias, K. M., and Hicks, H. R. 2003. "Numerical methods for the solution of partial differential equations of fractional order." *J. Comput. Phys*. 192: 406–421.

[172] Yuste, S. B., and Acedo, L. 2005. "An explicit finite difference method and a new von Neumann-type stability analysis for fractional diffusion equations." *Siam J. Numer. Anal*. 42 (5): 1862–1874.

[173] Ford, N. J., and Simpson, C. 2001. "The numerical solution of fractional differential equations: Speed versus accuracy." *Numer. Algorithms* 26: 333–346.

[174] Zhang, Y. 2009. "A finite difference method for fractional partial differential equation." *Appl. Math. Comput*. 215: 524–529.

[175] Duan, J. S. 2005. "Time- and space-fractional partial differential equations." *J. Math. Phys*. 46: 1063–1071.

[176] Liszka, T., and Orkisz, J. 1980. "The finite difference method at arbitrary irregular grids and its application in applied mechanics." *Comput. & Struct.* 11: 83–95.

[177] Spalding, D. B. 1972. "A novel finite difference formulation for differential expressions involving both first and second derivatives." *Int. J. Numer. Methods Eng.* 4: 551–559.

[178] Yang, Q., Liu, F., and Turner, I. 2010. "Numerical methods for fractional partial differential equations with Riesz space fractional derivatives." *Appl. Math. Model*. 34: 200–218.

[179] Yoo, H. 2000. "Semi-discretization of stochastic partial differential equations on R1 by a finite-difference method." *Math. Comp*. 69: 653-666.

[180] Cui, M. 2009. "Compact finite difference method for the fractional diffusion equation." *J. Comput. Phys*. 228: 7792–7804.

[181] Lin, Y. M., and Xu, C. J. 2007. "Finite difference/spectral approximations for the time-fractional diffusion equation." *J. Comput. Phys*. 225: 1533–1552.

[182] Szabo, B., and Babuhska, I. 1991. *Finite Element Analysis*. New York: A Wiley-Interscience Publication.

[183] Nayroles, B., Touzot, G., and Villon, P. 1992. "Generalizing the finite element method: Diffuse approximation and diffuse elements." *Comput. Mech*. 10: 307–318.

[184] Babuska, I., Tempone, R., and Zouraris, G. E. 2004. "Galerkin finite element approximations of stochastic elliptic partial differential equations." *SIAM J. Numer. Anal*. 42 (2): 800–825.

[185] Becker, R., Kapp, H., and Rannacher, R. 2000. "Adaptive finite element methods for optimal control of partial differential equations: basic concept." *SIAM J. Control Optim*. 39 (1): 113–132.

[186] Houston, P., and Süli, E. 2005. "A note on the design of hp-adaptive finite element methods for elliptic partial differential equations." *Comput. Methods Appl. Mech. Eng*. 194: 229–243.

[187] Ainsworth, M., and Senior, B. 1998. "An adaptive refinement strategy for hp-finite element computations." *Appl. Numer. Math*. 26: 165– 178.

[188] Harriman, K., Houston, P., Senior, B., and Süli, E. 2005. "hp-Version discontinuous Galerkin methods with interior penalty for partial differential equations with nonnegative characteristic form." Paper presented at the International Conference on the Occasion of Stanley Osher's 60th Birthday. Hong Kong University, Hong Kong, December 12–15.

[189] Heuveline, V., and Rannacher, R. 2003. "Duality-based adaptivity in the hp-finite element method." *J. Numer. Math*. 1 (2): 95–113.

[190] Moore, P. K. 2003. "Applications of Lobatto polynomials to an adaptive finite element method: a posteriori error estimates for hp-adaptivity and grid-to-grid interpolation." *Numer. Math*. 94: 367–401.

[191] Rachowicz, W., Demkowicz, L., and Oden, J. T. 1989. "Toward a universal h–p adaptive finite element strategy, Part 3. Design of h–p meshes." *Comput. Methods. Appl. Mech. Eng*. 77: 181–212.

[192] Schwab, Ch., and Suri, M. 1996. “The p and h–p version of the finite element method for problems with boundary layers.” *Math. Comp*. 65: 1403–1429.

[193] Ford, N. J., Xiao, J., and Yan, Y. 2011. “A finite element method for time fractional partial differential equations.” *Fract. Calc. Appl. Anal*. 14 (3): 454–474.

[194] Jiang, Y., and Ma, J. 2011. “High-order finite element methods for timefractional partial differential equations.” *J. Comput. Appl. Math*. 235: 3285–3290.

[195] Langlands, T. A. M., and Henry, B. I. 2005. “The accuracy and stability of an implicit solution method for the fractional diffusion equation.” *J. Comput. Phys*. 205: 719–736.

[196] Li, J., Cheng, A. H. D., and Chen, C.-S. 2003. “A comparison of efficiency and error convergence of multiquadric collocation method and finite element method.” *Eng. Anal. Bound. Elem*. 27: 251–257.

[197] Cook, R., Malkus, D., and Plesha, M. 2001. *Concepts and Applications of Finite Element Analysis*. New York: John Wiley & Sons.

[198] Cheney, W., and Kincaid, D. 2008. *Numerical Mathematics and Computing*. Cengage Learning.

[199] Brunch, J. C., and Zyvolovsky, G. 1974. “Transient two-dimensional heat conduction problems solved by the finite element method.” *Int. J. Numer. Meth. Eng*. 8: 481–494.

[200] Pham, Q. T. 1985. “A fast, unconditionally stable finite-difference scheme for heat conduction with phase change.” *Int. J. Heat Mass Transfer* 28 (11): 2079–2084.

[201] Isgor, O. B., and Razaqpur, A. G. 2004. “Finite element modelling of coupled heat transfer, moisture transport and carbonation processes in concrete structures.” *Cement & Concrete Compos*. 26: 57–73.

[202] Liu, X. L., Crouch, I. G., and Lam, Y. C. 2000. “Simulation of heat transfer and cure in pultrusion with a general-purpose finite element package.” *Compos. Sci. Tech*. 60: 857–864.

[203] Hackett, R. M., and Zhu, S. Z. 1992. “Two-dimensional finite element model of the pultrusion process.” *J. Reinf. Plast. Compos*. 11: 1322–1351.

[204] Ruan, Y., and Liu, J. 1994. "A steady-state heat transfer model for fiber-reinforced thermoplastic pultrusion processes using the finite element method." *J. Mater. Process. Manuf. Sci*. 3: 91–113.

[205] Lam, Y. C, Joshi, S. C., and Liu, X. L. 1998. "Application of a general-purpose finite element package for numerical modelling of resin flow through fibrous media." *Proceedings of the International Conference on Advances in Materials and Processing Technologies (AMPT-4)*, Kuala Lumpur, Malaysia.

[206] Chen, C. M., and Kovacevic, R. 2003. "Finite element modelling of friction stir welding–thermal and thermomechanical analysis." *Int. J. Mach. Tools Manuf*. 43: 1319–1326.

[207] Monde, M. 2000. "Analytical method in inverse heat transfer problem using Laplace transform technique." *Int. J. Heat Mass. Transfer* 43: 3965-3975.

[208] Chu, H. P., and Chen, C. L. 2008. "Hybrid differential transform and finite difference method to solve the nonlinear heat conduction problem." *Commun. Nonlinear Sci. Numer. Simul*. 13: 1605–1614.

[209] Ishak, A., Nazar, R., and Pop, I. 2008. "Heat transfer over a stretching surface with variable heat flux in micropolar fluids." *Phys. Lett. A* 372 (2008) 559–561.

[210] Mittal, R., and Moin, P. 1997. "Suitability of Upwind-Biased Finite Difference Schemes for Large-Eddy Simulation of Turbulent Flows." *AIAA J.* 35 (8): 1415–1417.

[211] Murthy, J. Y., and Mathur, S. R. 1998. "Finite Volume Method for Radiative Heat Transfer Using Unstructured Meshes." *J. Thermophys. Heat Transfer*. 12 (3): 313–321.

[212] Reddy, J. N., and Gartling, D. K. 2010. *The Finite Element Method in Heat Transfer and Fluid Dynamics*. Boca Raton: CRC Press.

[213] James, W. B, Wostenholm, G. H., Keen, G. S., and McIvor, S. D. 1987. "Prediction and measurement of the thermal conductivity of composite materials." *J. Phys. D: Appl. Phys*. 20: 261 – 268.

[214] Bai, Y., Vallée, T., and Keller, T. 2008. "Modelling of thermal responses for FRP composites under elevated and high temperatures." *Compos. Sci. Tech*. 68: 47–56.

[215] Griffis, C. A., Masumra, R. A., and Chang, C. I. 1981. "Thermal response of graphite epoxy composite subjected to rapid heating." *J. Compos. Mater*. 15: 427–42.

[216] Chang, C. I. 1986. "Thermal effects on polymer composite structures." *Theor. Appl. Fract. Mech*. 6(2): 113–20.

[217] Henderson, J. B., and Wiecek, T. E. 1987. "A mathematical model to predict the thermal response of decomposing, expanding polymer composites." *J. Compos. Mater*. 21(4): 373–93.

[218] McManus L. N., and Springer G. S. 1992. "High temperature thermo-mechanical behavior of carbon-phenolic and carbon–carbon composites." *I. Analysis. J. Compos. Mater*. 26 (2): 206–229.

[219] Wang, M., Kang, Q., and Pan, N. 2009. "Thermal conductivity enhancement of carbon fiber composites." *Appl. Therm. Eng*. 29: 418–421.

[220] Choi, S. U. S., Zhang, Z. G., Yu, W., Lockwood, F. E., and Grulke E. A. 2001. "Anomalous thermal conductivity enhancement in nanotube suspensions." *Appl. Phys. Lett*. 79 (14): 2252–2254.

[221] Gao, X. Q., Guo, Q. G., Shi, J. L., Li, G. S., Song, J. R., and Liu, L. 2005. "The fabrication of chopped carbon fiber-carbon composites and their thermal/electrical conductivity and microstructure." *New Carbon Mater*. 20 (1): 18–22.

[222] Nan, C. W., Shi, Z., and Lin, Y. 2003. "A simple model for thermal conductivity of carbon nanotube-based composites." *Chem. Phys. Lett*. 375 (5–6): 666–669.

[223] Fu, S. Y., and Mai, Y. W. 2003. "Thermal conductivity of misaligned short-fiber-reinforced polymer composites." *J. Appl. Polym. Sci*. 88 (6): 1497–1505.

[224] Springer, G. S., and Tsai, S. W. 1967. "Thermal conductivities of unidirectional materials." *J. Compos. Mater*. 1: 166–173.

[225] Han, L. S., and Cosner, A. A. 1981. "Effective thermal conductivities of fibrous composites." *J. Heat Transfer* 103: 387–392.

[226] Gupta, N., Gorthi, R. C., and Mishra, S. C. 2006. "Lattice Boltzmann Method Applied to Variable Thermal Conductivity Conduction and Radiation Problems." *J. Thermophys. Heat Transfer* 20 (4): 895–902.

[227] Das, R., Mishra, S. C., and Uppaluri, R. 2009. "Retrieval of thermal properties in a transient conduction–radiation problem with variable thermal conductivity." *Int. J. Heat Mass Transfer* 52: 2749–2758.

[228] Chiang, J. Y., and Chen, C. K. 2008. "Application of grey prediction to inverse nonlinear heat conduction problem." *Int. J. Heat Mass Transfer* 51: 576–585.

[229] Elbarbary, E. M. E., and Elgazery, N. S. 2004. "Chebyshev Finite Difference Method for the Effects of Variable Viscosity and Variable Thermal Conductivity on Heat Transfer from Moving Surfaces with Radiation." *Int. J. Therm. Sci*. 43: 889-899.

[230] Dehghan, M., and Saadatmandi, A. 2008. "Chebyshev finite difference method for Fredholm integro-differential equation." *Int. J. Comput. Mech*. 85 (1): 123–130.

[231] Rashed, M. T. 2003. "Numerical solution of a special type of integro-differential equations." *Appl. Math. Comput*. 143: 73–88.

[232] Ghaly, A. Y., and Seddeek, M. A. 2004. "Chebyshev finite difference method for the effects of chemical reaction, heat and mass transfer on laminar flow along a semi-infinite horizontal plate with temperature dependent viscosity." *Chaos, Solitons Fractals* 19: 61–70.

[233] Saadatmandi, A., and Dehghan, M. 2008. "The numerical solution of problems in calculus of variation using Chebyshev finite difference method." *Phys. Lett. A* 372: 4037–4040.

[234] Khater, A. H., Temsah, R. S., and Hassan, M. M. 2008. "A Chebyshev spectral collocation method for solving Burgers'-type equations." *J. Comput. Appl. Math*. 222: 333–350.

[235] Tsai, R., Huang, K. H., and Huang, J. S. 2008. "Flow and heat transfer over an unsteady stretching surface with non-uniform heat source." *Int. Commun. Heat Mass Transfer* 35: 1340–1343.

[236] Ramezani, M., Dehghan, M., and Razzaghi, M. 2008. "Combined Finite Difference and Spectral Methods for the Numerical Solution of Hyperbolic Equation with an Integral Condition." *Numer. Meth. Partial Diff. Eq*. 24 (1), 1–8.

[237] Horng, I. R., and Chou, J. H. 1985. "Shifted Chebyshev direct method for solving variational problems." *Int. J. Syst. Sc*i. 16: 855–861.

[238] Chiang, P.-J., Wu, C.-L., Teng, C.-H., Yang, C.-S., and Chang, H.-C. 2008. "Full-Vectorial Optical Waveguide Mode Solvers Using Multidomain Pseudospectral Frequency-Domain (PSFD) Formulations." *IEEE J. Quant. Electr*. 44 (1): 56–66.

[239] Fahroo, F., and Ross, I. M. 2002. "Direct Trajectory Optimization by a Chebyshev Pseudospectral Method." *J. Guidance Control Dynamics* 25 (1): 160–166.

[240] Soubaras, R., and Zhang, Yu. 2008. “Two-step explicit marching method for reverse time migration.” *SEG Technical Program Expanded Abstracts* 2272–2276.

[241] Elgazery, N. S. 2008. “An implicit-Chebyshev pseudospectral method for the effect of radiation on power-law fluid past a vertical plate immersed in a porous medium.” *Comm. Nonlinear Sci. Numer. Simulat*. 13: 728–744.

[242] Khader, M. M., and Megahed, A. M. 2013. “Numerical studies for flow and heat transfer of the Powell-Eyring fluid thin film over an unsteady stretching sheet with internal heat generation using the Chebyshev finite difference method.” *J. Appl. Mech. Tech. Phys*. 54: 440–450.

[243] Peng, H. S., and Chen, Ch. L. 2011. “Hybrid differential transformation and finite difference method to annular fin with temperature-dependent thermal conductivity.” *Int. J. Heat Mass Transfer* 54: 2427–2433.

[244] Bruschke, M. V., and Advani, S. G. 1990. “A Finite Element/Control Volume Approach to Mold Filling in Anisotropic Porous Media.” *Polym. Compos*. 11 (6): 398–405.

[245] Hamila, N., and Boisse, P. 2008. “Simulations of textile composite reinforcement draping using a new semi-discrete three node finite element.” *Compos*. Part B 39: 999–1010.

[246] Dong, L., Lekakou, C., and Bader, M. G. 2001. “Processing of composites: simulations of the draping of fabrics with updated material behaviour law.” *J. Compos. Mater*. 35(2): 138–63.

[247] Wang, W., Sadeghipour, K., and Baran, G. 2008. “Finite element analysis of the effect of an interphase on toughening of a particle-reinforced polymer composite.” *Compos. Part A* 39: 956–964.

[248] Sun, C. J., Wu, W., Mahanti, S., Sadeghipour, K., Baran, G. R., and Debnath, S. 2006. “Finite element analysis of toughening for a particle reinforced composite.” *Polym. Compos*. 27 (4): 360–367.

[249] Guild, F. J., and Kinloch, A. J. 1995. “Modelling the properties of rubber-modified epoxy polymers.” *J. Mater. Sci*. 30 (7): 1689–1697.

[250] Ayyar, A., and Chawla, N. 2006. “Microstructure-based modelling of crack growth in particle reinforced composites.” *Compos. Sci. Technol*. 66 (13): 1980–1994.

[251] Kassam, Z. H. A., Zhang, R. J., and Wang, Z. 1995. "Finite element simulation to investigate interaction between crack and particulate reinforcements in metal-matrix composites." *Mater. Sci. Eng. A* 203 (1–2): 286–299.

[252] Reid, A. C. E., Langer, S. A., Lua, R. C., Coffman, V. R., Haan, S. I., and García, R. E. 2008. "Image-based finite element mesh construction for material microstructures." *Comput. Mater. Sci*. 43: 989–999.

[253] Pan, Y., Iorga, L., and Pelegri, A. A. 2008. "Analysis of 3D random chopped fiber reinforced composites using FEM and random sequential adsorption." *Comput. Mater. Sci*. 43: 450–461.

[254] Dede, E. M. 2010. "Simulation and optimization of heat flow via anisotropic material thermal conductivity." *Comput. Mater. Sci*. 50: 510–515.

[255] Binci, M., Fullwood, D., and Kallidindi, S. R. 2008. "A new spectral framework for establishing localization relationships for elastic behavior of composites and their calibration to finite-element models." *Acta Mater*. 56: 2272–2282.

[256] Tarleton, T., Charalambides, M. N., and Leppard, C. 2012. "Image-based modelling of binary composites." *Comput. Mater. Sci*. 64: 183–186.

[257] Islam, Md. R., and Promila, A. 1999. "Thermal Conductivity of Fiber Reinforced Composites by the FEM." *J. Compos. Mater*. 33 (18): 1699–1715.

[258] Song, Y. S., and Youn, J. R. 2006. "Evaluation of effective thermal conductivity for carbon nanotube/polymer composites using control volume finite element method." *Carbon* 44: 710–717.

[259] Najafi, M., Roghani-Mamaqani, H., Salami-Kalajahi, M., and Haddadi-Asl, V. 2010. "A comprehensive Monte Carlo simulation of styrene atom transfer radical polymerization." *Chinese J. Polym. Sci*. 28 (4): 483−497.

[260] Liu, L. C., and Huang, M. J. 2010. "Thermal conductivity modelling of micro- and nanoporous silicon." *Int. J. Therm. Sci*. 49: 1547–1554.

[261] Sakata, D., Ashida, F., and Kojima, T. 2010. "Stochastic homogenization analysis for thermal expansion coefficients of fiber reinforced composites using the equivalent inclusion method with perturbation-based approach." *Comput. Struct*. 88: 458–466.

[262] Peraud, J. P. M., and Hadjiconstantinou, N. G. 2011. "Efficient simulation of multidimensional phonon transport using energy-based variance-reduced Monte Carlo formulations." *Phys. Rev. B* 84: 205331.

[263] Boming, Z., Zhong, Y., Yufeng, W., and Hongwei, S. 2010. "Hierarchical multi-scale modelling of failure in unidirectional fiber-reinforced plastic matrix composite." *Mater. Design* 31: 2312–2318.

[264] Naveira-Cotta, C. P., Orlande, H. R. B., and Cotta, R. M. 2010. "Integral transforms and bayesian inference in the identification of variable thermal conductivity in two-phase dispersed systems." *Numer. Heat Transfer, Part B* 57: 173–202.

[265] Ersoy, N., Garstka, T., Potter, K., Wisnom, M. R., Porter, D., Clegg, M., and Stringer, G. 2010. "Development of the properties of a carbon fibre reinforced thermosetting composite through cure." *Composites*: *Part A* 41: 401–409.

[266] Wang, F., Shuai, Y., Tan, H., and Yu, C. 2013. "Thermal performance analysis of porous media receiver with concentrated solar irradiation." *Int. J. Heat Mass Transfer* 62: 247–254.

[267] Liu, B., and Shen, S. 2013. "Broadband near-field radiative thermal emitter/absorber based on hyperbolic metamaterials: Direct numerical simulation by the Wiener chaos expansion method." *Phys. Rev. B* 87: 115403.

[268] Xu, P., Zheng, J., Chen, H., and Liu, P. 2010. "Optimal design of high pressure hydrogen storage vessel using an adaptive genetic algorithm." *Int. J. Hydrogen Energy* 35: 2840–2846.

[269] Gong, F., Bui, K., Papavassiliou, D. V., and Duong, H. M. 2014. "Thermal transport phenomena and limitations in heterogeneous polymer composites containing carbon nanotubes and inorganic nanoparticles." *Carbon* 78: 305 – 316.

[270] Duong, H. M., Yamamoto, N., Bui, K., Papavassiliou, D. V., Maruyama, S., and Wardle, B. L. "Morphology Effects on Nonisotropic Thermal Conduction of Aligned Single-Walled and Multi-Walled Carbon Nanotubes in Polymer Nanocomposites." *J. Phys. Chem. C* 114: 8851–8860.

[271] Su, R. J., and Hwang, J. J. 1998. "Analysis of Transient Heat Transfer in a Cylindrical Pin Fin." *J. Thermophys. Heat Transfer* 12 (2): 281–283.

[272] Hammersley, J. M., and Handscomb, D. C. 1964. *Monte Carlo methods*. New York – London – Methuen: Jonh Wiley & Sons.

[273] Kalos, M. H., and Whitlock, P. A. 1986. *Monte Carlo methods*. New York: John Wiley & Sons.

[274] Fishman, G. S. 1996. *Monte Carlo Concept. Algorithms and applications*. New York: Springer.

[275] Liu, J. S. 2003. *Monte Carlo strategies in scientific computing*. New York: Springer.

[276] Haji-Sheikh, A., and Sparrow, E. M. 1966. "The floating random walk and its application to Monte Carlo solutions of heat equations." *J. SIAM Appl. Math*. 14 (2): 370–389.

[277] Haji-Sheikh, A., and Sparrow, E. M. 1967. "The Solution of Heat Conduction Problems by Probability Methods." *J. Heat Transfer* 89 (2): 121–130.

[278] Zinsmeister, G. E., and Pan, S. S. 1976. "A modification of the Monte Carlo method for steady heat conduction problems." *Int. J. Numer. Method. Eng*. 10: 1057–1064.

[279] Cruz, M. E., and Patera, A. T. 1995. "A parallel Monte-Carlo finite-element procedure for the analysis of multicomponent random media." *Int. J. Numer. Method. Eng.* 38: 1087-1121.

[280] Kowsary, F., and Arabi, M. 1999. "Monte Carlo solution of anisotropic heat conduction." *Int. Comm. Heat Mass Transfer* 26 (8): 1163-1173.

[281] Belova, I. V., and Murch, G. E. 2004. "Monte Carlo simulation of the effective thermal conductivity in two-phase material." *J. Mater. Process. Tech*. 153,154: 741-745.

[282] Fiedler, T., Öchsner, A., Muthubandara, N., Belova, I. V., and Murch, G. E. 2007. "Calculation of the Effective Thermal Conductivity in Composites Using Finite Element and Monte Carlo Methods." *Mater. Sci. Forum* 553: 51–56.

[283] Fiedler, T., Belova, I. V., Öchsner, A., and Murch, G. E. 2010. "Lattice Monte Carlo Analysis of Thermal Diffusion in Multi-Phase Materials." In *Heat Transfer in Multi-Phase Materials*, edited by A. Öchsner, and G. E. Murch, 275–300, Berlin Heidelberg: Springer-Verlag.

[284] Bahadori, R., Gutierrez, H., Manikonda S., and Meinke, R. 2017. "Two-dimensional transient heat conduction in multi-layered

composite media with temperature dependent thermal diffusivity using floating random walk Monte-Carlo method." *Int. J. Heat Mass Transfer* 115: 570–580.

[285] Bahadori, R., Gutierrez, H., Manikonda S., and Meinke, R. 2018. "A mesh-free Monte-Carlo method for simulation of three-dimensional transient heat conduction in a composite layered material with temperature dependent thermal properties." *Int. J. Heat Mass Transfer* 119: 533–541.

[286] Grove, S. M. 1990. "A Model of Transverse Thermal Conductivity in Unidirectional Fibre-Reinforced Composites." *Compos. Sci. and Technol*. 38: 199-209.

[287] Guo, Z., and Zhao, T. S. 2005. "A lattice Boltzmann model for convection heat transfer in porous media." *Numer. Heat Transfer, Part B* 47: 157–177.

[288] Freed, D. M. 1998. "Lattice-Boltzmann method for macroscopic porous media modelling." *Int. J. Mod. Phys. C* 9: 1491–1503.

[289] Kang, Q., Zhang, D., and Chen, S. 2001. "Unified lattice Boltzmann method for flow in multiscale porous media." *Phys. Rev. E* 66: 056307.

[290] Vafai, K., and Tien, C. L. 1981. "Boundary and inertia effects on flow and heat transfer in porous media." *Int. J. Heat Mass Transfer* 24:195–203.

[291] Alexander, F. J., Chen, S., and Sterling, J. D. 1993. "Lattice Boltzmann thermohydrodynamics." *Phys. Rev. E* 47: R2249–R2252.

[292] Fang, W.-Z., Chen, L., Gou, J.-J., and Tao, W.-Q. 2016. "Predictions of effective thermal conductivities for three-dimensional four-directional braided composites using the lattice Boltzmann method." *Int. J. Heat Mass Transfer* 92: 120–130.

[293] Javaran, E. J., Nassab, S. A. G., and Jafari, S. 2010. "Thermal analysis of a 2-D heat recovery system using porous media including lattice Boltzmann simulation of fluid flow." *Int. J. Thermal Sci*. 49: 1031–1041.

[294] Xiao, X., Zhang, P., and Li, M. 2013. "Preparation and thermal characterization of paraffin/metal foam composite phase change material." *Appl. Energy* 112: 1357–1366.

[295] Karani, H., and Huber, C. 2015. “Lattice Boltzmann formulation for conjugate heat transfer in heterogeneous media.” *Phys. Rev. E*, 91 023304.

[296] Tao, Y. B., You, Y., and He, Y. L. 2016. “Lattice Boltzmann simulation on phase change heat transfer in metal foams/paraffin composite phase change material.” *Appl. Thermal Eng*. 93: 476–485.

[297] Wang, M., Wang, X., Wang, J., and Pan, N. 2013. “Grain size effects on effective thermal conductivity of porous materials with internal thermal contact resistance.” *J. Porous Media* 16 (11): 1043–1048.

[298] Veyret, D., and Tsotridis, G. 2010. “Numerical determination of the effective thermal conductivity of fibrous materials. Application to proton exchange membrane fuel cell gas diffusion layers.” *J. Power Sources* 195: 1302–1307.

[299] Demuth, C., Mendes, M. A. A., Ray, S., and Trimis, D. 2014. “Performance of thermal lattice Boltzmann and finite volume methods for the solution of heat conduction equation in 2D and 3D composite media with inclined and curved interfaces.” *Int. J. Heat Mass Transfer* 77: 979–994.

[300] Wang, M., He, J., Yu, J., and Pan, N. 2007. “Lattice Boltzmann modelling of the effective thermal conductivity for fibrous materials.” *Int. J. Therm. Sci*. 46 (9): 848–855.

[301] Xie, C., Wang, J., Wang, D., Pan, N., and Wang, M. 2015. “Lattice Boltzmann Modelling of Thermal Conduction in Composites with Thermal Contact Resistance.” *Commun. Comput. Phys*. 15 (4): 1037-1055.

[302] Thomas, M., Boyard, N., Perez, L., Jarny, Y., and Delaunay, D. 2008. “Representative Volume Element of Anisotropic Unidirectional Carbon-Epoxy Composite with High-Fibre Volume Fraction.” *Compos. Sci. Tech*. 68: 3184–3192.

[303] Muliana, A. H., and Kim, J. S. 2010. “A two-scale homogenization framework for nonlinear effective thermal conductivity of laminated composites.” *Acta Mech*. 212: 319–347.

[304] Fish, J., and Shek, K. 2000. “Multi-scale analysis of composite materials and structures.” *Compos. Sci. Technol*. 60: 2547–2556.

[305] Goyheneche, J. M., and Cosculluela, A. 2005. “A multiscale model for the effective thermal conductivity tensor of a stratified composite material.” *Int. J. Thermophys*. 26: 191–202.

[306] Yu, Q., and Fish, J. 2002. "Multi-scale asymptotic homogenization for multiphysics problems with multiple spatial and temporal scales: a coupled thermo-viscoealstic example problem." *Int. J. Solids Struct*. 39: 6429–6452.

[307] Xing, Y. F., Yang, Y, and Wang, X. M. 2010. "A multi-scale eigenelement method and its application to periodical composite structures." *Compos. Struct*. 92 (2010) 2265–2275.

[308] Srinivasan, M., Maettig, P., Glitza, K.W., Sanny, B., and Schumacher, A. 2014 "Multi-scale Calculation for Increasing the Thermal Conductivity of Carbon Fiber Composite with Diamond Powder." *Proceeding of the XLII International Summer School Conference-Advanced Problems Mech., St.-Petersburg, Institute for Problems in Mechanical Engineering RAS* 481–490.

[309] Pike, M. G., and Oskay, C. 2015. "Modelling Random Short Nanofiber- and Microfiber-Reinforced Composites Using the Extended Finite-Element Method." *J. Nanomech. Micromech*. 5 (1): A4014005.

[310] Kim, H. J., and Swan, C. C. 2003. "Algorithms for automated meshing and unit cell analysis of periodic composites with hierarchical tri-quadratic tetrahedral elements." *Int. J. Numer. Meth. Eng*. 58: 1683–1711.

[311] Hou, T. Y., and Wu, X. H. 1997. "A Multi-scale Finite Element Method for Elliptic Problems in Composite Materials and Porous Media." *J. Comput. Phys*. 134 (1): 169-189.

[312] Ghosh, S., and Mukhopadhyay, S. N. 1993. "A material based finite element analysis of heterogeneous media involving Dirichlet tessellations." *Comput. Methods Appl. Mech. Eng*. 104: 211-247.

[313] Matt, C. F., and Cruz, M. E. 2008. "Effective Thermal Conductivity of Composite Materials with 3-D Microstructures and Interfacial Thermal Resistance." *Numer. Heat Transfer, Part A* 53: 577–604.

[314] Glasserman, P. 2003. *Monte Carlo Methods in Financial Engineering*. New York: Springer.

[315] Zaginaylo, I., Maksimeniuk, Ya., and Pysarenko, A. 2017. "Two-Dimensional Numerical Simulation Study of the Effective Thermal Conductivity Statistics for Binary Composite Materials." *Int. J. Heat Technol*. 35 (2): 364–370.

INDEX